Air Jets for Lift Control in Low Reynolds Number Flow

by

Erik Skensved

A thesis
presented to the University of Waterloo
in fulfilment of the
thesis requirement for the degree of
Master of Applied Science
in
Mechanical Engineering

Waterloo, Ontario, Canada, 2010

I hereby declare that I am the sole author of this thesis. This is a true copy of the thesis, including any required final revisions, as accepted by my examiners.

I understand that my thesis may be made electronically available to the public.

Abstract

The environmental and monetary cost of energy has renewed interest in horizontal-axis wind turbines (HAWT). One problem with HAWT design is turbulent winds, which cause cyclic loading and reduced life. Controlling short-term aerodynamic fluctuations with blade pitching or mechanical flaps is limited by the speed of actuation. The objective was to investigate using jet-flap-like fluidic actuators on the 'suction surface' of an aerofoil for rapid aerodynamic control. A NACA 0025 aerofoil was constructed for wind-tunnel experiments. The low Reynolds number (Re) flow was measured non-intrusively with particle image velocimetry (PIV). The jet showed limited effect compared to published work. The sharp trailing edge and distance to the jet were determined to be critical factors. At Re $\approx$ 100000 the 'suction surface' jet sheet is less useful for control than the conventional 'pressure surface' sheet. The experiment suggests usage near the blade root on truncated aerofoils.

Acknowledgements

I would like to thank Dr. David Johnson for supervision and guidance of this research, as well as his assistance with the preparation of this document. I would also like to thank Stephen Orlando for assistance with the Laser Doppler Anemometer, and also for taking the photographs which appear in this report. Thanks also to Brian Gaunt and Michel McWilliam for advice on the Particle Image Velocimetry method.

Dedication

This thesis is dedicated to my parents.
Without them none of this would be possible.

Contents

List of Tables

List of Figures

Nomenclature

Roman Symbols

Δt Time interval between PIV frames [s]

ΔX Particle shift between PIV frames [m]

$\dot{m}$ Mass flow rate per unit span [kg s^{-1} m^{-1}]

A_j Area of the fluid jet [m^2]

c Blade or aerofoil chord [m]

C_μ Jet momentum coefficient

C_l Lift coefficient

$C_{lC_{\mu=0}}$ Lift coefficient with jet off

$C_{lC_{\mu\neq0}}$ Lift coefficient with jet on

$C_{l,measured}$ Measured lift coefficient

d Diameter of jet holes [m]

d_s Beam separation distance [m]

f Focal length [m]

h Wind tunnel height [m]

l Distance along laser beam from waist [m]

p_f Flow pressure [Pa]

r Span location [m]

R_{air} Specific gas constant for air [J kg^{-1} K^{-1}]

s Jet-flapped span [m]

$Std(N)$ Standard deviation of the normal force on blade [N]

t	Overall aerofoil half-thickness as a fraction of c
T_f	Flow temperature [K]
U_∞	Free-stream velocity [m s^{-1}]
V_j	Speed of the fluid jet [m s^{-1}]
$V_{x,y,n}$	Time averaged local jet velocity [m s^{-1}]
w	Beam half width [m]
x, y, z	Local tunnel coordinates [m]
y_t	Local aerofoil half-thickness as a fraction of c
$\overline{V}_{x,y}$	Average local jet velocity over all jets [m s^{-1}]
C	Jet supply loss coefficient
Re	Reynolds number
X,Y,Z	Global tunnel coordinates [m]

Greek Symbols

α	Angle of attack [rad]
λ	Wavelength of light [m]
ω	Angular velocity [rad s^{-1}]
ϕ	LDA beam intersection angle [rad]
ρ_∞	Free stream density [kg m^{-3}]
ρ_j	Density of the fluid jet [kg m^{-3}]
$\sigma_{x,y}$	Local standard deviation of velocity [m s^{-1}]
θ	Jet deflection angle $\equiv$ angle between zero-lift line and the jet direction at the trailing edge [rad]
ξ	Dummy coordinate for chord-wise position ($0 < \xi < 1$)

Subscripts

0	Beam waist
des	Indicates design conditions
f	Focal distance from waist

Chapter 1

Introduction

In the modern world, one of the key resources is energy; this fact is self evident. With concerns over the price of fossil fuels, and their environmental impact, interest in wind as a source of energy has been renewed [1]. Historically wind was captured in order to deliver mechanical power for a particular task. The current use of horizontal-axis wind turbines (HAWT) to generate electricity is the focus of this document.

Briefly, horizontal-axis wind turbines, described more thoroughly by Burton et al. [1], consist of one or more aerofoil-shaped blades attached to a horizontally mounted shaft. The action of the wind on the blades creates the shaft torque necessary to turn an electrical generator either directly or through a gearbox. The blade-shaft-generator system is mounted on a vertical-axis yaw assembly and either pivots freely, or is actively oriented, into the wind. The designer of such a wind turbine is concerned with its ability to generate power safely over its design lifetime. A contributing factor to both the safety and lifespan of a turbine is the ability to control its operation within prescribed limits.

One of the key problems with wind turbine design is that, in operation, turbines are subject to unpredictable wind conditions. Design of turbines using the blade element method (BEM) assuming uniform constant wind is relatively well known. Unfortunately such conditions do not exist in nature. Variations in wind can be categorized as long-term or short-term and as periodic or random.

Control of turbines experiencing long-term uniform fluctuations has been achieved with variable-slip generators, variable-pitch blades, and by coupling the generator to the grid through special power electronics [1]. Control of short-term variations with these traditional methods is limited due to practical pitching rates and rotor inertia.

Periodic short-term fluctuations are those that occur 'N-times per revolution'. For example vertical wind shear or error in the turbine orientation (yaw error) causes a periodic change in both the angle and magnitude of the flow over the blade as it rotates. This of course leads to a periodic load being applied to the blades

and accordingly the whole turbine. Though it has been proposed that turbine blades could be cyclically pitched [1] [2] the practicality is questionable due to required pitching rates. It has been suggested that the decrease in rotor speed with increasing diameter could lead to cyclic pitch being more practical, however increasing the blade size may also reduce achievable pitching rates.

Random velocity fluctuations result from natural turbulence in the wind. Theoretically, independent blade pitching could be implemented, but different radial locations would require different magnitudes of pitch change. Thus even this solution would require a compromise over the blade span.

The final consideration of short-term variations is that dynamic effects cannot be neglected. In particular the variation of aerofoil lift that is associated with dynamic stall cannot be neglected. This change in lift from expected levels affects the mechanical forces on the turbine components and is a strong incentive to attempt control of short-term variation.

The main objective of this research is to investigate the potential of using high-velocity air jets to control the response of aerofoils in low to moderate Reynolds number (Re) flow. Specifically the objective is to use a jet flap on the 'suction surface' of an orthodox aerofoil to reduce the lift and drag forces similar to an aileron.

Chapter 2 below is devoted to a brief review of: literature on the dynamic stall phenomena, prior work on jet flaps, and other related work on aerodynamic control. In Chapter 3 the construction of the aerofoil model that was used in the wind-tunnel experiments is described along with its air supply system. Chapters 4 and 5 detail the setup and analysis of the laser Doppler anemometer (LDA) measurements used to validate the control jet. In Chapters 6, 7, 8, and 9 the main wind-tunnel experiment is detailed. The basic particle image velocimetry (PIV) setup used for data collection is reviewed in Chapter 6. The calculations performed to extract results from the raw data is described in Chapters 7 and 8. Chapter 9 presents the lift control results from the PIV experiment along with comparison data from previous work. Finally in Chapter 10 the conclusions and recommendations of the research are summarized.

Chapter 2

Literature Review

The purpose of this chapter is to provide a general overview of relevant literature on the topic of aerodynamic flow control as it relates to wind turbines. More specifically the goal is to highlight what research has been done and what has yet to be done. Finally the reviewed literature provides a basis that is built upon in the current work.

2.1 Dynamic Stall

Static stall of an aerofoil can be considered a steady process. The unsteady counterpart to static stall is dynamic stall. Dynamic stall occurs when the timescale of the stall process is of equal or smaller order to the fluid-mechanic timescale [3].

An experiment was conducted by Schreck and Robinson [4] to investigate the dynamic stall response of HAWT blades. This dynamic stall condition leads to amplified fluctuating loads, which shorten machine life and may cause variations in the voltage or phase of the generated power. According to the authors the inability to mitigate dynamic stall phenomena in turbine designs results from an inability to produce a detailed aerodynamic model. This itself is a result of ignorance of the fundamental three-dimensional flow fields about dynamically-stalling turbine blades. Another contributing factor, not mentioned by the authors, is the inability to provide an adequate control response to dynamic stall.

In previous two-dimensional wind-tunnel experiments [3] it was found that when an aerofoil is rapidly pitched beyond the static stall angle a small, energetic vortex is formed near the leading edge. This vortex grows and convects downstream over the aerofoil suction surface causing a temporary low surface pressure and accordingly high lift. Once the vortex convects off the surface the aerofoil is statically stalled. Even in this simplified case there exist complex vortex kinematics. To extend understanding to the flow kinematics of operating HAWTs, the full rotating case must be investigated.

The rotational case was studied using the Unsteady Aerodynamics Experiment (UAE) upwind turbine in the NASA Ames wind tunnel [5]. One of the two blades was outfitted with surface pressure taps. Local flow angle (LFA) was measured with five-hole probes on $0.8c$ long stalks attached to the leading edge of the blade. These stalks were offset from the surface pressure taps, but one might question whether they could disturb the flow, particularly if it were already unstable. Ideally a noninvasive measurement method should be used.

The UAE turbine was set at yaw angles from 10° to 60° during the experiments. A nonzero yaw angle causes the HAWT blades to experience pseudo-sinusoidal variations in angle of attack (α) and LFA with azimuthal angle. Under this condition the blade α can rise above the static stall limit during its rotation. The LFA results from the vector addition of the tunnel free-stream velocity (U_∞) and the local azimuthal velocity ($r \cdot \omega$). The authors note that the LFA was used directly and not converted to α due to uncertainty over how the flow angle changes between the position of the five-hole probe and the leading edge of the aerofoil.

The dynamic stall vortex was detected by the passage of a local minima in surface pressure by the rows of pressure taps. Since there was good repeatability between the 36 blade-rotation cycles, the data from the cycles were ensemble averaged into a single pressure profile for each condition.

In previous two-dimensional work [3] it was found that, if the LFA crosses the static stall LFA during the pitching cycle, dynamic stall results. If the LFA remains always above or always below the static stall LFA, dynamic stall was found not to occur. Refer to Figure 2.1 for schematic representation of this stall process.

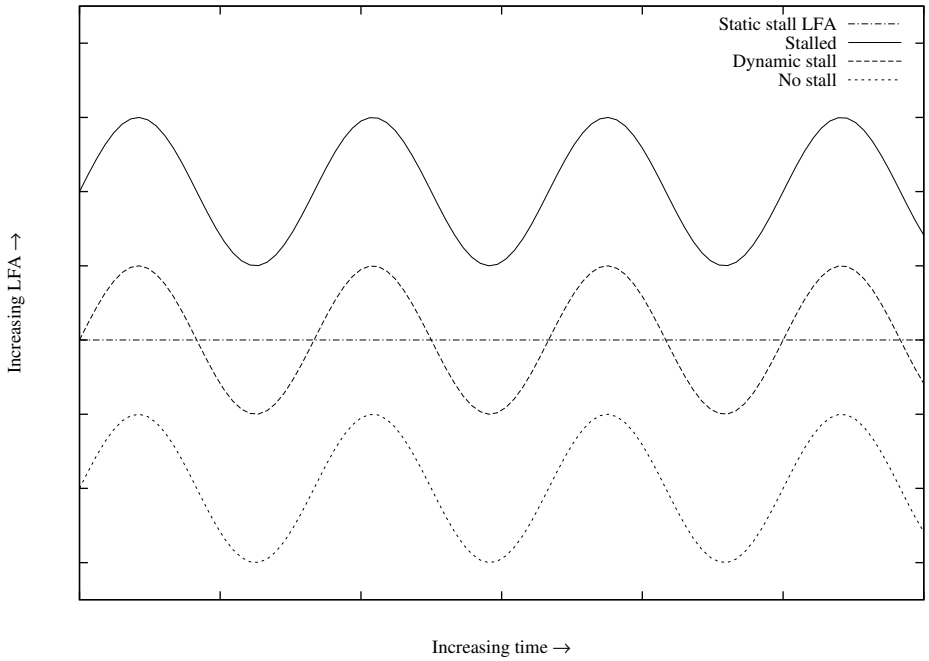

Figure 2.1: Schematic of stall response with sinusoidal LFA.

In this three-dimensional study it was found that, though dynamic stall will not occur if the static stall limit is not crossed, dynamic stall may not occur even if the limit is crossed. Similarly if the LFA always exceeds the stall limit, then one would expect that the aerofoil would remain statically stalled. This is also not necessarily the case in three-dimensional flow. This limit crossing rule gives a general guideline as to when three-dimensional flow will dynamically stall, however it must be realized that it is not an accurate predictor.

It was found that, the LFA at which dynamic stall initiated, was dependent on the radial location on the blade. The inboard position initiated at the lowest angle followed closely by the outboard section. Interestingly, the midsection of the blade was most resistant to dynamic stall initiation. Though the midsection was the last region to initiate stall, the vortex convection rate was higher than that of the root or tip. The authors suggest that the stall vortex was pinned, which is to say convection was impeded, at the root and tip of the blade, hence its overall convection rate was slowed and it was not released off the blade.

As either U_∞ or the yaw angle were increased the dynamic stall vortex extended from the root towards the tip. No evidence of the vortex reaching the blade tip was found. This leads to the conclusion that attempts to mitigate the dynamic stall event should be focused on the region from the mid-span to near, but not directly at, the blade root.

2.2 The Jet Flap

The purpose of this section is to provide some background into the jet flap and prior analytical and experimental work done by other researchers. The first work is a general overview of the pioneering work, both analytical and experimental, on the jet flap. The second paper details a single set of early work done by Dimmock [6].

2.2.1 Introduction to the Jet Flap

A survey of the important experimental and theoretical work on the jet flap up until about 1960 was done by Korbacher and Sridhar [7]. The purpose was to aggregate what was known and highlight what was not known.

The 'jet flap' is an aerodynamic flow control device that is analogous to the traditional mechanical flap. As implied by the name, this device uses a jet of air to control air flowing over an aerofoil. This flow control affects both the air of the boundary layer, near the aerofoil surface, and the circulation of the air far from the surface.

The distinction between boundary layer control (BLC) and circulation control (CC) is not well defined. Generally BLC refers to either: blowing air to increase the momentum of the air flow near the surface of the aerofoil, or suction to remove

this low-momentum air. The purpose of controlling the boundary layer is typically to prevent the flow from separating from the aerofoil surface. There are also other techniques that have been investigated to energize the flow, however they are not described herein. Circulation control picks up where BLC leaves off. The goal is typically to increase the circulation above the 'natural' level of an aerofoil with fully attached flow.

The use of the term 'jet flap' is broad and encompasses both the 'blown flap' and its variations, as well as the 'pure jet flap' that does not involve a physical surface. The blown flap, in the context of CC, involves the use of a small flap or shrouded flap to redirect a high speed jet of fluid, via the Coanda effect [8], at an angle θ to the chord of the aerofoil. The high-momentum fluid increases the *effective* size of the small movable flap. In contrast the pure jet flap consists of a high-momentum jet of fluid exhausted directly from a nozzle, movable or not, without the physical flap surface, so that the jet of fluid itself acts as the flap.

For low momentum jets theoretical work has shown that the blown flap is more effective than the pure variety. The experiments presented in Chapters 4 and 6 are concerned with a configuration more similar to the pure flap for practical considerations. For this reason research related to the pure flap is the focus of this chapter.

Two key hypotheses were proposed; the lift hypothesis and the thrust hypothesis. These hypotheses rely on three assumptions: no mixing between the jet and the surrounding fluid, no profile drag, and two-dimensional flow with no induced drag. Under these conditions the jet, beginning at an angle θ to the free stream, must curve and asymptotically approach the direction of the free stream. If the jet—a streamline—does not eventually reach the free stream direction it would impart an infinite momentum in the vertical direction to the flow field.

Thrust hypothesis: *The jet thrust experienced by the aerofoil in the counter stream wise direction is equal to the magnitude of the jet thrust at the outlet regardless of the initial angle (θ) of the jet* [7].

Lift hypothesis: *The total lift of the jet flapped aerofoil is equal to the pressure lift exerted on the aerofoil and its imaginary solid curved flap plus the reaction component of the jet in the lifting direction* [7].

There are several different rigorous arguments, not described here, for both of these hypothesis. Of course real air flow is not two-dimensional nor ideal, hence these predictions are somewhat optimistic. Nevertheless the indicated potential for lift and thrust enhancement are still enticing.

The jet momentum coefficient (Equation 2.1) is the non-dimensional parameter most frequently used to characterize the jet in BLC and CC research. In essence it is a ratio of the jet momentum flux (jet thrust) over pressure force (dynamic pressure multiplied by area). The coefficient used throughout this document utilizes the

per-unit-span momentum flux and is therefore a two-dimensional coefficient. Thus $\dot{m}$ is the jet mass flow per-unit-span, while the scale is a length (c) rather than an area. Note in many older publications C_μ is written as C_J.

$$C_\mu \equiv \frac{\dot{m}V_j}{\frac{1}{2}\rho_\infty U_\infty^2 c} \tag{2.1}$$

There are eight theoretical treatments for the lift of a jet flapped aerofoil given in this review. The most intuitive analogy is the curved mechanical flap. The lift is determined from the composite camber line once the shape of the curved flap has been determined. The most useful expression is due to an approximation and extension by Strand [9] of Spence's [10] work. Spence considered the balance of centripetal acceleration to the pressure difference across the jet. Consequently the jet could be 'replaced' with a line of representative point vortexes, similar to what is done in thin aerofoil theory. If the resulting integro-differential equations are solved, as in thin aerofoil theory, an expression for the total lift is determined:

$$C_l = 2\pi\alpha + 4\pi(A_0\theta + B_0\alpha) \tag{2.2}$$

where A_0 and B_0 are Fourier coefficients that are a function of C_μ. The approximate expression for the total lift given by Strand is:

$$C_l = 2\pi\alpha + \left(\pi\sqrt{C_\mu} + C_\mu\right)(\theta + \alpha) \tag{2.3}$$

though this expression utilizes the small angle approximation. A modified expression, also given, for angles up to 90° is:

$$C_l = 2\pi\alpha\eta + \left(3.9\sqrt{C_\mu} + C_\mu\right) sin(\theta + \alpha) \tag{2.4}$$

where η is a constant determined from a test with $C_\mu = 0$.

Equation 2.4 reflects the physical phenomena involved in generating lift. In general the lift can be separated into three lifting forces: natural lift, reaction lift, and pressure lift. The natural lift of the aerofoil is $2\pi\alpha\eta$. The reaction lift is the component of the jet thrust in the lift direction ($C_\mu sin(\theta+\alpha)$). Lastly the pressure lift component is $3.9\sqrt{C_\mu}sin(\theta + \alpha)$.

The component of interest to this investigation is of course the pressure lift. The pressure lift is a result of the lowered static pressure region extending from the trailing edge toward the leading edge of the suction surface and the same pattern of increased pressure on the opposite surface. The low pressure region is created by the action of the jet drawing air down from over the aerofoil to fill the region behind the jet (Figure 2.2). This both provides a favourable pressure gradient (BLC) for the naturally occurring flow over the suction surface and also further increases the lifting force (CC).

The pressure profile over the upper surface of the aerofoil is in the form of suction peaks over the leading and trailing edges (Figure 2.2). The leading edge

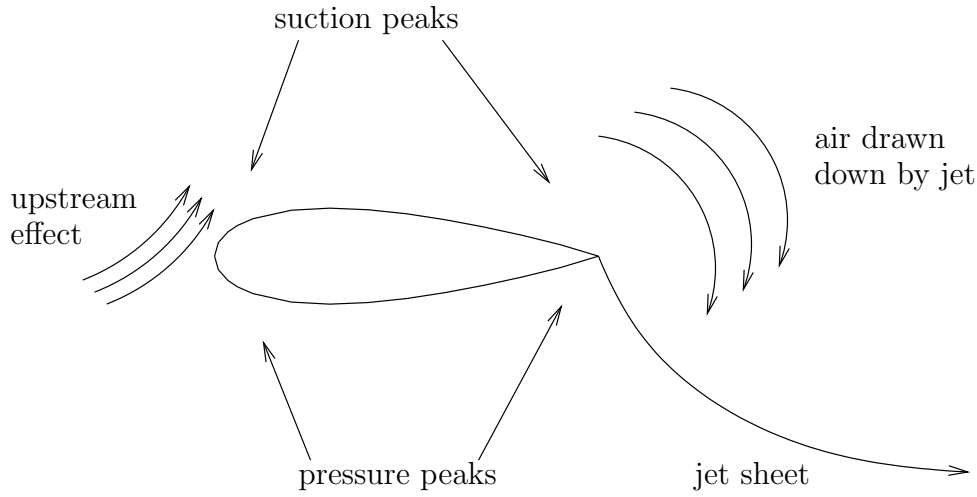

Figure 2.2: Basic mechanism of the jet flap.

suction peak is responsible for the net thrust being independent of θ, as stated in the thrust hypothesis. In non-ideal flow the leading edge suction peak is diminished with respect to the trailing edge peak. This is particularly true if leading edge separation occurs and can lead to negative net thrust being generated (net drag). Larger leading edge radii tend to create pressure gradients more favourable for attached flow in this region.

As the angle of attack of the aerofoil increases a separation bubble forms near the leading edge. The action of the jet causes the leading edge separated flow to reattach. The jet behaves somewhat like an ejector pump strongly drawing the upstream flow over the aerofoil. The size of the separation bubble can increase by extending until it reaches the trailing edge.

Stall of a jet flapped aerofoil occurs when the separation bubble bursts open and forms a wake. This is caused by either an increase in α or θ such that the influence of the jet can no longer maintain flow attachment. Thus the stall α decreases with increased θ. It is therefore important to be cautious with setting θ to avoid flow separation.

Not surprisingly the other parameter that plays a role in flow separation and stall, in addition to α and θ, is the Reynolds number. The Reynolds number of the jet flapped aerofoil is based on the chord of the aerofoil, the free stream velocity and the kinematic viscosity of the air ($\mathrm{Re} = \frac{U_\infty c}{\nu}$). The Reynolds number has been found to have a large effect on the lift and drag of the jet flapped aerofoil. Korbacher and Sridhar [7] state that while a Re of 4×10^6 may approximate cruise conditions in aircraft (20×10^6), an approximation of slow flight $\mathrm{Re} = 5 \times 10^6$ by a Reynolds number of 1×10^6 could be problematic due to laminar separation. Korbacher and Sridhar refer to the work of Dimmock [6] on the effects of Reynolds number. This research is described in Section 2.2.2 below.

Experimental evidence [11] shows that the measured thrust is less than the thrust predicted by the thrust hypothesis, which is equal to the total jet momentum flux. This being said the thrust at large θ is greater than the pure reaction component of the jet, lending support to the hypothesis. Part of this deficit can be attributed to the non-ideal mixing that is contrary to the basic assumptions. It has been found that the entrainment angle of the flow into the jet can be over 90°. In idealized flow the jet is a streamline and the external flow is parallel. Even in idealized jet mixing the flow is also parallel not perpendicular, so in the real case there will be some 'secondary losses' [11] beyond the primary mixing loss. Another issue in jet mixing is entrainment of the slow moving boundary layer. Since entrainment rate is proportional to the difference in velocity between the streams [12] the jet spreading rate is increased by the boundary layer and the entrainment occurs at a larger angle incurring higher losses. In addition to loss of thrust in the entrainment process the reduced pressure in the trailing edge region contributes to overall drag on the aerofoil.

The relation of Korbacher and Sridhar's jet flap review to the current work should be clear. Knowledge of the general working principle of the flap is key to its use. The lift and thrust hypotheses suggest it is possible to use a jet flap to control the lift force on the blade while at the same time recovering power through the shaft torque created by the jet thrust. Non-ideal effects were revealed through Korbacher and Sridhar's experimentation. These effects are responsible for diminishing the effect of the jet and so care is required to create an effective system.

2.2.2 Additional Information About the Jet Flap

The following work done by Dimmock [6] was done with a view at using full-span propulsive jets in aeronautical applications namely aircraft wings. This basic research allowed the testing of the theoretical predictions of aerodynamic forces and moments, particularly the lift and thrust hypotheses.

The aerofoil chosen was an elliptical section 12.5% thick with a 0.203 m chord and a 0.305 m span. This very low aspect ratio leads to doubt about the two-dimensionality of the flow. An ellipse was chosen for ease of comparison between experiments and analytic predictions that require coordinate transformations. It was thought that an elliptical section might be as appropriate as any other aerofoil section for a jet flapped wing. This section does not have the sharp trailing edge common to most low speed aerofoils, hence its performance with the jet turned off is not the same as conventional sections. Three jet deflection angles (θ) of 0°, 31.4°, 90° were tested by fabricating the aerofoil with a replaceable brass trailing edge. The latter two angles allowed the effect of θ to be studied, while the 0° angle was used to isolate the drag due to jet entrainment. The model was suspended at both ends of the span by the parallel arms of a thrust balance. Lift was determined from 26 static pressure taps situated around the aerofoil section. The model was supplied with compressed air for the jet.

Reynolds Number Effects

The Reynolds number used in Dimmock's experiment was the chordal value as defined in Section 2.2.1. Due to the limited tunnel size the aerofoil chord could not be made large enough to test at full scale Reynolds number. In the 90° model tests the Re ranged from 0.425×10^6 to 0.459×10^6 for $0.000 \leq C_\mu \leq 0.467$. In the 31.4° model tests the Re was 0.425×10^6 for $C_\mu \leq 0.50$ and from 0.147×10^6 to 0.425×10^6 for $0.50 < C_\mu \leq 4.17$.

As a result of the generally low and variable Reynolds number in the experiments some care must be taken in interpreting the results. Three factors lead Dimmock to conclude that flow transition was occurring: an abrupt change in slope of the lift versus momentum flux curve (Figure 2.3), the appearance of a trailing edge suction peak at roughly the same C_μ (Figure 2.4), and also a discontinuity in the surface-pressure curve near the trailing edge (Figure 2.5). Consequently experiments were done with trip wires in various locations on the chord to determine the effect of transition and separation. Experiments were done with trip wires installed at both leading and trailing edges of the suction and pressure surfaces. The final position of the trip wires on both surfaces was at 82% of chord near the trailing edge.

Further experimentation was done with smoke and wool tufts. This demonstrated that momentum deficiency in the boundary layer, which normally forms a wake, absorbed jet momentum. Decreased *available* jet momentum results in decreased lift augmentation and decreased net thrust. The presence of the trip wires caused the boundary layer to be tripped and re-energized, thereby preventing flow separation and net momentum loss. Dimmock suggested that the loss of momentum due to laminar separation near the trailing edge is greater than that of a turbulent boundary layer. In other words a thick boundary layer causes loss, however a separated boundary layer causes more loss.

If the jet momentum, and therefore the lift coefficient, is increased beyond a limit the flow transitions from laminar to turbulent near the leading edge. After this point the trailing edge trip wire has no effect. The slope of the lift versus momentum curve lowers slightly at this point revealing the loss in effective jet strength.

At higher jet momentum flux, and higher lift, the flow separates near the leading edge. Despite the separation, the lift continued to increase smoothly and the trailing edge suction peak continued to increase.

It was noted that there was separation evident at the trailing edge with the 90° jet always. It seems reasonable that, independent of the Reynolds number, the trailing edge configuration may affect the separation behaviour of the aerofoil.

Entrainment Effects

In addition to the aforementioned loss in effective jet strength when thick or separated boundary layers are entrained into the jet there is also the manner of the

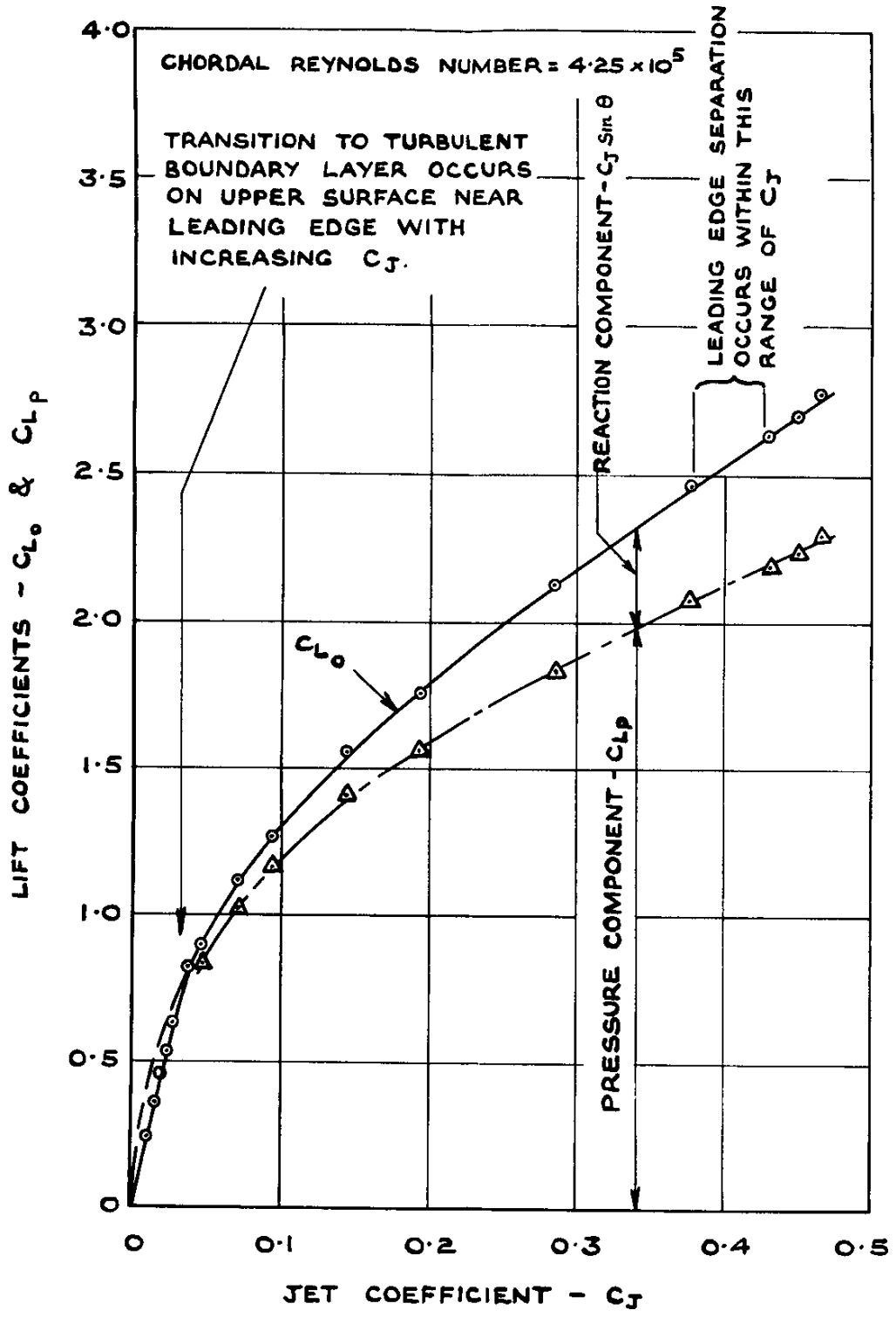

Figure 2.3: Lift versus momentum flux curve from Dimmock [6]. Test conditions: $\alpha = 0°$ and $\theta = 90°$. Note change in slope at approximately $C_\mu = 0.04$ indicating transition. Note also that $C_J \equiv C_\mu$.

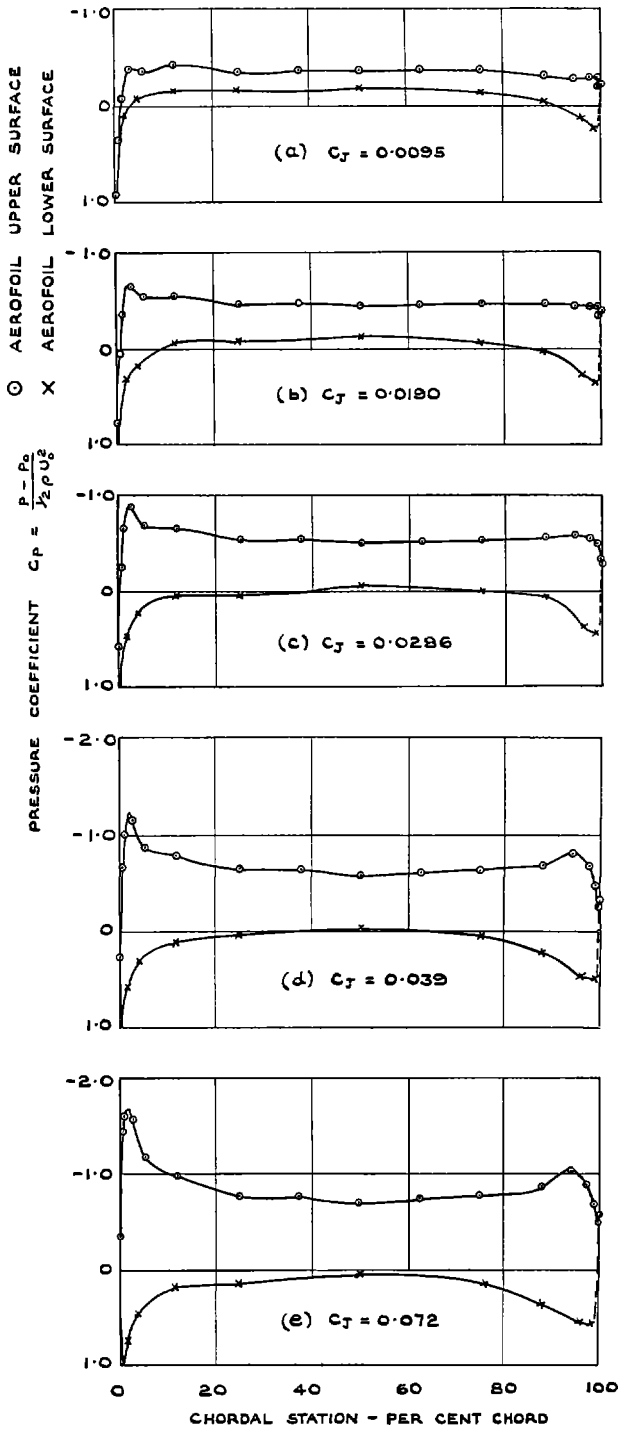

Figure 2.4: Surface pressure profiles from Dimmock [6]. Note existence of trailing-edge suction peak in (d) and (e), but not in (a), (b), or (c). Note also that $C_J \equiv C_\mu$.

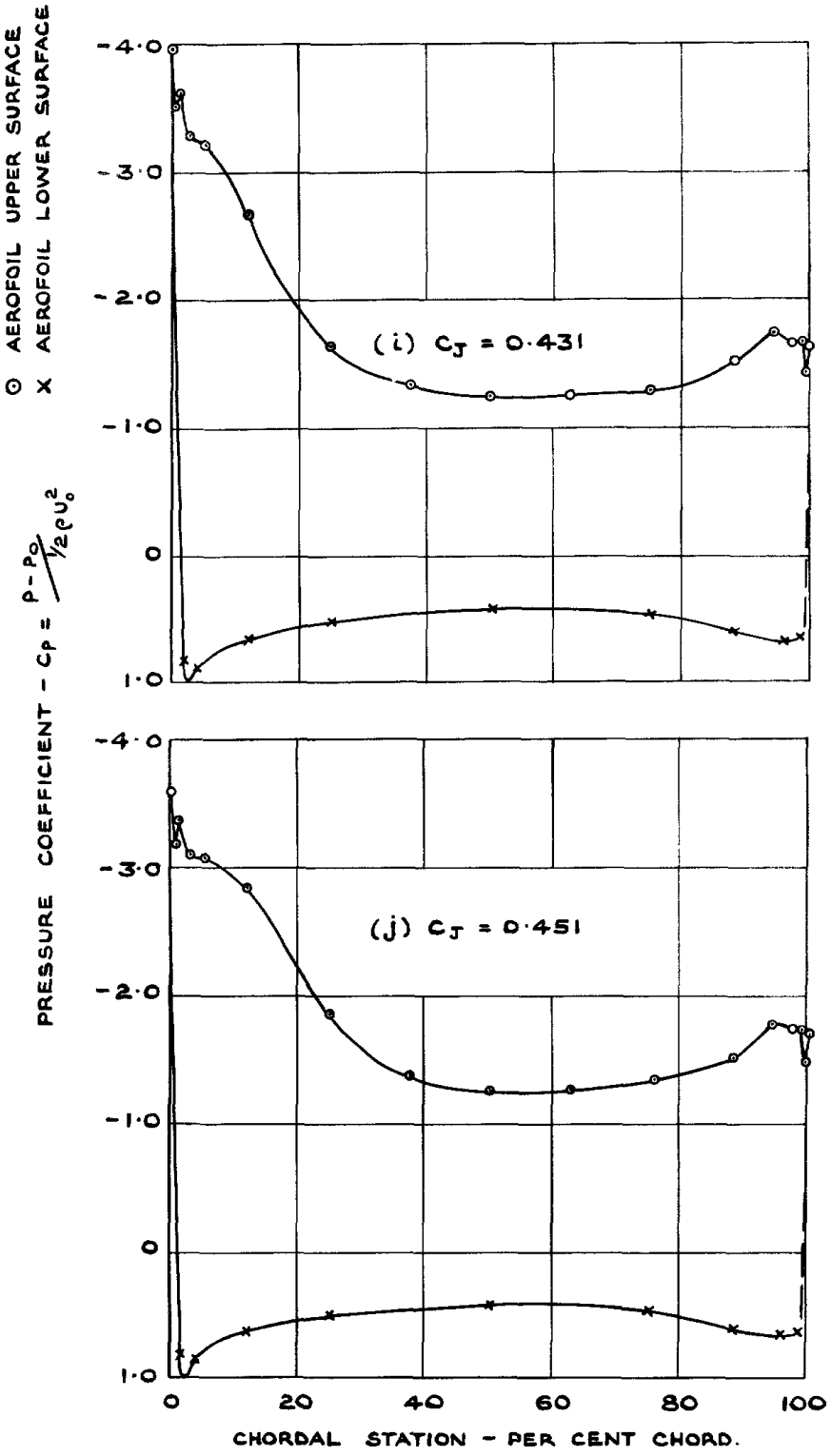

Figure 2.5: Surface pressure profile from Dimmock [6]. Note the discontinuity in the pressure trace near 100% of chord. Note also that $C_J \equiv C_\mu$.

entrainment. Again experimentation with wool tufts and smoke revealed that the flow was turned perpendicular to the jet before being entrained. In the ideal case no mixing occurs. Ideal jet mixing involves parallel streams. The basic assumptions are not consistent with parallel mixing and so there is a loss.

Using the 90° model the thrust was measured first with the pressure distribution, then later with the thrust balance. Though the maximum measured thrust was only 37% of the raw jet momentum flux, this still provides support for the thrust hypothesis, since the direct component of thrust is zero. When C_μ exceeded 0.4 the flow separated at the leading edge and there was a reduction in measured thrust.

The entrained flow around the aerofoil can influence the pressure distribution. If the pressure in the vicinity of the jet is lowered there will be an increase in the drag force; this is termed 'jet drag'. Experimentation with a 0° trailing edge jet allowed this drag component to be measured (Figure 2.6). It was found that, in this implementation, the jet drag was approximately $0.06C_\mu$ for $C_\mu < 0.10$ and $0.017C_\mu$ at higher values of C_μ ($\mathrm{Re} = 0.425 \times 10^6$). At $\mathrm{Re} = 0.212 \times 10^6$ the slope continues at 0.06 until $C_\mu = 0.25$ then changes to 0.0104. It may be that these values vary depending on implementation, however this does give an order of magnitude of the jet drag loss.

2.3 Related Work

The purpose of this section is to review the prior research into the use of trailing-edge devices for active lift control on wind turbine blades. This was done with a view of using control jets to influence the net circulation around the blade section. Emphasis has been given to the Gurney flap as it is somewhat analogous to the low-momentum jet flap. Though not directly applicable, such related studies can lend valuable ideas to the current body of research.

2.3.1 Numerical Study Comparing a Circulation Control Rotor to a Gurney Flap Equipped Rotor

A numerical study of the flow around the National Renewable Energy Laboratory (NREL) Phase VI rotor was completed by Tongchitpakdee et al. [13]. The study compared the use of a fixed Gurney flap and a trailing-edge Coanda jet at low and high wind speeds. The NREL Phase VI rotor uses stall-controlled S809 blades. Since stall-controlled machines can only operate in a very limited range of wind speeds, there is an incentive to increase the power extracted under low wind-speed conditions.

The circulation control technology used by Tongchitpakdee et al. [13] is similar to that found in other studies. The basic premise is that a high-momentum jet of fluid is ejected tangential to a curved surface. As long as the pressure differential

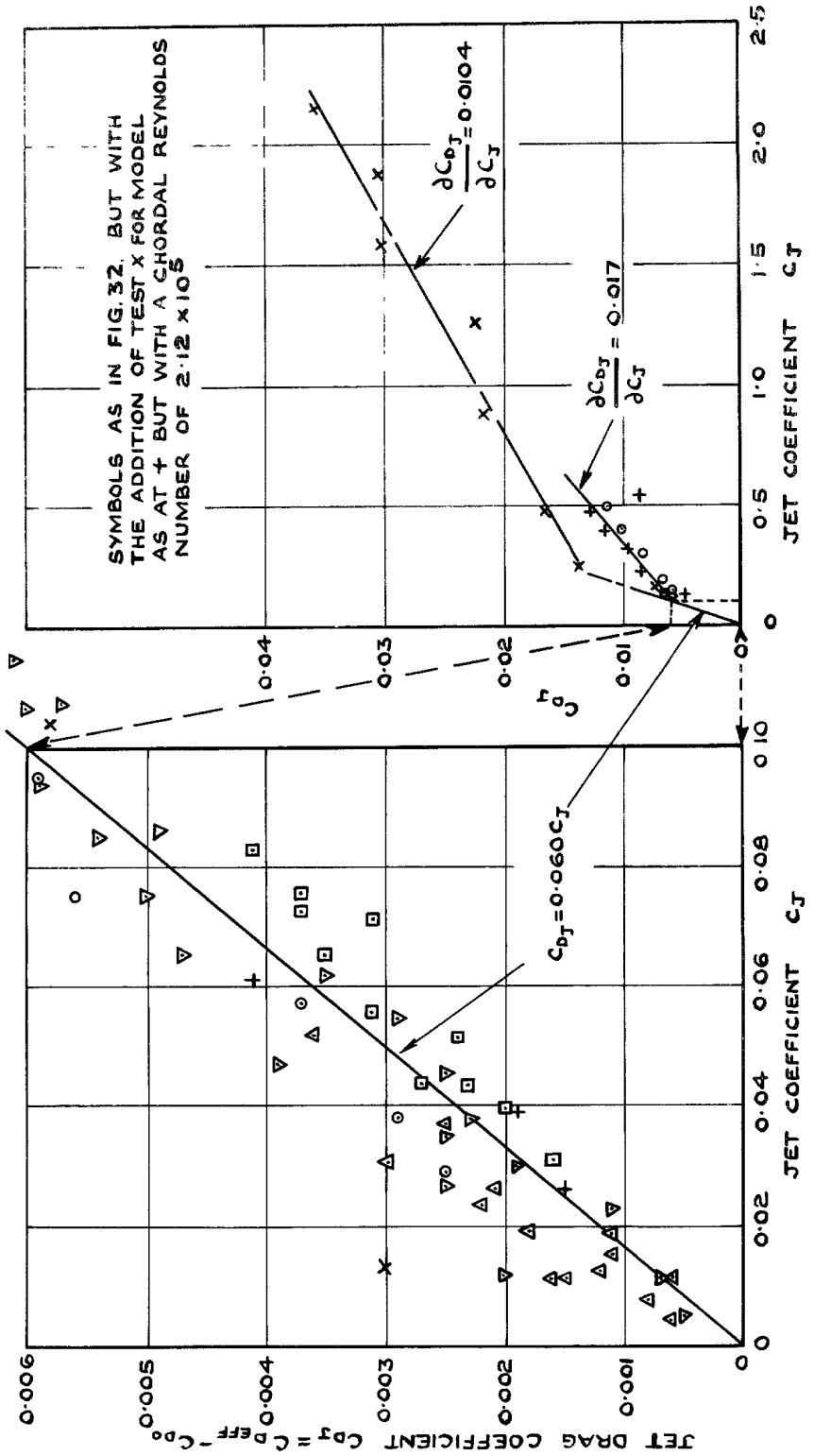

Figure 2.6: Jet drag coefficient from Dimmock [6]. All symbols except x's are from tests at $\mathrm{Re} = 0.425 \times 10^6$. Note also that $C_J \equiv C_\mu$.

across the jet is sufficient to balance the centripetal acceleration the fluid will follow the surface. This is the so called 'Coanda Effect'. In this case the S809 aerofoil was modified to have a small jet slot at 93% of chord on the suction surface and a rounded trailing edge. To minimize the drag penalty associated with a blunt trailing edge only the upper surface was curved, while the lower surface was maintained flat. In other studies a corner between upper and lower surfaces is avoided, since this essentially fixes the location of the rear stagnation point. The jet flow therefore causes only the front stagnation point to move backward along the lower aerofoil surface. Significant turning of the inviscid outer flow is still achieved.

Gurney flaps are also devices used to change the circulation, and hence the lift, of an aerofoil. In this study small tabs were placed at the trailing edge of the pressure surface. These tabs extended $0.015c$ into the flow from the rotor surface.

This study used unsteady compressible Reynolds-averaged Navier-Stokes (RaNS) equations in three dimensions. The Reynolds number of the rotor tip in this investigation was 1.3×10^6.

The key results of the study are as follows. The Coanda jet was effective at increasing both the lift and thrust at low wind speed (7 m s^{-1}). The Gurney flap was also able to increase the circulation of the blade, however with this method there was a drag penalty.

At high speed (15 m s^{-1}) the flow separated from the upper surface of the rotor with both methods. Neither method was able to augment the thrust or normal force of the rotor significantly, but only increase the drag on the rotor. The authors suggest that a leading-edge jet may be able to suppress leading-edge separation and allow the trailing-edge jet to be effective.

In this paper the authors introduce a potentially useful concept of excess power (Equation 2.5). The excess power represents the benefit of using the lift enhancement technology. The cost in terms of power consumed can also be represented as a percentage of the baseline power. The suggested expression for cost is Equation 2.6, where C is a coefficient to account for the inefficiencies of the jet supply system. Obviously if the excess power is greater than the power consumed then the circulation-control method is worthwhile.

$$\text{Excess Power} \equiv \frac{\begin{array}{c}\text{Power generated by} \\ \text{circulation control rotor}\end{array} - \begin{array}{c}\text{Power from the} \\ \text{baseline configuration}\end{array}}{\text{Power from the baseline configuration}} \times 100\% \tag{2.5}$$

$$\text{Power Consumed} \equiv \frac{1}{2} C \rho_j A_j V_j^3 \tag{2.6}$$

2.3.2 Experimental Comparison of a Gurney Flap and a Jet Flap

Another study, relevant to the current research, was the experimental work done by Traub et al. [14]. This study was a comparison between a trailing-edge jet flap and a Gurney flap. The central idea of this study was the ability to control the flow, or 'virtually alter' the aerofoil profile, without conventional moving parts. In the words of the authors "hingeless flow control." This has the stated advantage of: stealth, reduced weight, compactness, increased robustness and increased tolerance of damage. All but the first stated advantage are relevant to wind turbine technology.

The model used in the experiment was a NACA 0015 aerofoil fitted with end plates to ensure two-dimensional flow. The aerofoil dimensions were 0.71 m chord and 0.235 m span, thus the aspect ratio was a rather low one-third. The aerofoil was constructed with a 1×10^{-3} m jet slot located 15×10^{-3} m from the trailing edge or 98% of chord. The jet deflection angle (θ) was 90°. For comparison, data were also acquired with a $0.0075c$ Gurney-flap attached to the aerofoil at the location of the jet slot. The Reynolds number was 0.7×10^6 and turbulence intensity was less than 0.5%. A three-component force balance was used to measure forces.

The authors present some of the more interesting results in terms of 'lift-augmentation ratio'. This is defined in Equation (2.7) and essentially compares the lift increment to the momentum supplied. If this ratio is greater than one, then the change in lift is larger than the reactive (thrust) component of the jet.

$$\frac{C_{lC_{\mu \neq 0}} - C_{lC_{\mu=0}}}{C_\mu} \tag{2.7}$$

The authors found that, not surprisingly, the jet-flap shifts the C_l - α curve upwards increasing the lift for a given α similar to a conventional flap. It was determined that the lift-augmentation ratio is approximately 15 to 5 for $0.0037 \leq C_\mu \leq 0.029$. The key finding here is that the ratio decreases with increasing C_μ, but is still significantly larger than one. Another key finding is that a C_μ of 0.0068 causes the same lift increment as the $0.0075c$ height Gurney flap in the same location in this implementation.

It was determined that at low α the Gurney flap had a small drag penalty, since the combination of jet power plus jet-flap drag is smaller than the Gurney-flap drag. At higher α the drag of the Gurney flap decreases and the aforementioned trend reverses.

On surface flow visualization was done using a thin plate, attached parallel to the end plates, with a titanium dioxide and kerosene mixture applied to it. The resulting streaks gave a qualitative idea of the flow behaviour. The authors conclude that, though the C_l may be the same, the flow is different around the Gurney and jet flaps. The key difference is that, while the Gurney-flap deflects the flow and

creates a wake, the jet-flap absorbs the free stream and actually draws the flow around the sharp trailing edge.

A serious criticism of this work is the very low aspect-ratio model used. Though end plates were used to maintain two-dimensional flow the authors admit that the plates were not large enough. Given the strong aspect-ratio effect noted in other jet-flap research [7], the magnitudes of the lift increments are questionable.

The key fact brought to light in this study is that the lift-augmentation ratio decreases with increasing momentum. Furthermore the relation developed analytically by Spence ($C_l \propto \sqrt{C_\mu}$) [15] was found to model the diminishing returns in lift. The final key finding was that the flow was drawn down around the sharp trailing edge and that the jet essentially becomes the dividing streamline.

2.3.3 Experimental Comparison of Discrete Translating Micro-tabs to a Solid Gurney Flap

An experimental and computational comparison of discrete translating tabs, as opposed to hinged tabs, with solid Gurney flaps was done by Nakafuji et al. [16]. The motivation for this work was the lack of fast acting control mechanisms currently available to mitigate wind turbine blade loads. The authors propose the use of micro-electro-mechanical (MEM) translational tabs for trailing edge control. The stated advantage of these MEM devices is their low cost and light weight, as well as being appropriate for installation in a small trailing edge. The proposed method of use is in an on-off capacity, wherein the on state functions similar to a Gurney flap.

In order to optimize size and location of the tab devices a two-dimensional RaNS computational fluid dynamic (CFD) study was done on a GU25-5(11)-8 aerofoil. This aerofoil was chosen for its similarity to typical thick wind turbine blade sections. The CFD and wind-tunnel lift results agree well with previously published results up to approximately 8°. At higher angles the stall behaviour of the three results deviated significantly, the experiment having a higher stall angle and the computation having a lower maximum C_l. Thus computational results that include separated flow should, not surprisingly, be treated with caution.

In the CFD study the tab position was varied between $0c$ and $0.10c$ in distance *from* the trailing edge. It was found that the C_l increased with tab position between $0c$ and $0.02c$, and decreased slightly from that point to $0.10c$. In the experimental study the C_l was high at $0c$ and decreased slightly from that point to $0.10c$. In other words the experiment did not show the initial increase that the CFD showed. This brings to light the fact that, for Gurney flaps at least, it is unnecessary to place the flap directly at the trailing edge. The computation showed that the drag decreased from $0c$ to $0.02c$ and increased from there to $0.10c$. Experimental results for drag were not presented due to excessive uncertainty, which is a common problem. Again it must be remembered that the flow behind the flap is badly separated and it is therefore worth questioning the accuracy of the computations.

The effect of tab height was also studied. The lift coefficient increased with tab heights between $0.0025c$ and $0.02c$. The incremental improvement with tab height however was a decreasing trend, so the overall lift coefficient was limited. The computational C_l results generally agreed with the experimental C_l results. The computational drag results showed a sharp drop from $0c$ to $0.0025c$ in height and an increase from there to $0.02c$ in height.

The authors conclude that, if the internal volume of the aerofoil is considered along with the C_l and C_d results, the best compromise is to mount the flap at 95% of chord or $0.05c$ *from* the trailing edge.

The aforementioned results are for two-dimensional flow over a continuous flap. For practical application the individual tabs require a small gap between them. The effect of different gap spacings, as a fraction of tab height, was also investigated. The spacing/height ratios used were: 0.5, 1, and 2. With the solid tab the lift enhancement was approximately 50%, while with the 0.5 ratio it was 42%. With the largest ratio the enhancement dropped to 20%. The important fact to notice here is that, so long as the spacing is not large, discrete tabs are almost as effective as solid flaps. It was also noted by the authors that discontinuous flaps have some drag reduction benefits, so the optimal configuration may not be the one with the maximum lift. Though such a fact cannot be applied directly to jet flaps, it does suggest the possibility of using discontinuous blowing slots.

2.3.4 Numerical Simulation of Lift Control Using a Curved Mechanical Flap

A numerical aeroelastic study of an aerofoil with an actively controlled flap has been conducted by Buhl et al. [17]. Based on previous work, the authors state that there is significant potential for the reduction of wind turbine blade loads by using an active control scheme. The study corresponds to a rather large *hypothetical* 10 MW pitch regulated wind turbine with a *hypothetical* 6 s rotational period.

An aerodynamic model for unsteady two-dimensional potential flow over a thin aerofoil with a deflecting camber line was used in this study. Using this model to predict lift forces is suitable so long as separation does not occur. The chosen aerofoil used was the Risø B1-18 with a cubic spline superimposed on the trailing 10% to form a curved flap. In this study the aerofoil was modelled as a rigid mass suspended in the two-dimensional plane on x, y, and rotational spring/dampers. Two base cases were investigated: a step in wind velocity and turbulence superimposed on average wind velocity.

The aerodynamic model was validated against a RaNS code. It was found that this code was able to predict the steady forces on the aerofoil for flap deflection angles of $\pm 10^\circ$ and attached flow. It was however found that the code overestimated the dynamic amplitude of the forces by 50%, although the dynamic response was otherwise correct. According to the authors this is adequate for the purpose of

variable trailing edge testing, but the accuracy of the relative improvements was not proven.

The chosen control inputs, for determining the trailing-edge deflection, were: position, velocity, and acceleration all in the flap-wise direction, as well as the blade inflow angle. These inputs were chosen as they are measurable quantities with accelerometers, strain gauges, and pitot tubes. The authors note that blade mounted pitot tubes may not be the most robust sensor, hence inflow angle measurement is undesirable unless new sensors can be developed. The effectiveness of these selected control inputs with an orthodox flap should give some indication of the potential for their use with jet controls. Control effectiveness was measured by the reduction in the standard deviation of the normal force on the blade ($Std(N)$). Refer to Table 2.1 for the load reductions.

Table 2.1: Summary of $Std(N)$ reduction with wind step.

Input	$Std(N)$ reduction
Position	55%
Velocity	59%
Angle	95%
Position & velocity & acceleration	85%

It must be noted that adding a time lag into the control loop or limiting the flap speed has a significant effect on the load reductions possible. Adding a 0.1 s time lag changes the maximum reduction from 95% to 34% if using inflow angle. The restriction on maximum pitching rate is less severe as the majority of load reduction benefit can be achieved with pitching rates of ± 10 °/s. It must be noted that the cyclic variations have already been matched with cyclic pitching of the entire blade. While this may be achievable on a turbine with a 6 s period, this could be excessive pitch activity for the trailing edge device of a 2 MW or smaller turbine.

With the turbulent flow field the maximum reduction using inflow angle was 81% with no lag and unlimited flap speed. According to the authors with realistic lag (0.01 s) and flap speed (10-30 °/s) the reduction is 25% to 38%. Using control based on blade transverse velocity and position the maximum reduction in $Std(N)$ was 75% in the turbulent wind. With lag and actuator velocity limit this decreases to 27%. Again this emphasizes the point that the control effectiveness, particularly using inflow angle, is strongly reliant on the control system speed and authority.

Three key lessons are taken from this study. An effective load control system based on blade mounted accelerometers is realistic. Care also must be taken to avoid exciting oscillations in the blade. Control system speed is of highest importance, since the load reduction is reduced with increasing time lag and slower actuator speed.

Chapter 3

Experimental Model

In this section the design and construction of the experimental jet-flow control model is detailed. Since this research was directed toward industrial application, the wind-tunnel model was designed with full-scale manufacture in mind. Thus simple and scalable construction was utilized.

The wind tunnel available for experiments was a bench-scale, $0.152\ \text{m} \times 0.152\ \text{m}$, closed-return type tunnel documented by Sperandei [18]. The model size was determined mainly from the tunnel dimensions. The model span is the full width of the tunnel less a small clearance. The model was constructed with this clearance so that a wind-tunnel force balance could be used. Unfortunately this force balance was unsatisfactory for use in the following experiments. Consequently there was a small gap ($\approx 3 \times 10^{-3}$ m) between the rear wind tunnel wall and the aerofoil allowing for some additional three-dimensional flow in this region (Figure 6.4). The chord of the model was made as large as possible to maximize Reynolds number. Pankhurst and Holder [19] suggest that at low tunnel speeds the chord should not exceed $\frac{1}{3}$ of the tunnel height (h), while Rae and Pope [20] suggest that the model frontal area should not exceed 7.5% of the tunnel cross-sectional area. With c nominally 50×10^{-3} m the model is roughly $\frac{1}{3}$ of h. For the chosen aerofoil at zero incidence, the frontal area is approximately 8.2% of the tunnel area, slightly in excess of what is recommended. At large α, 15° for example, this blockage would increase by approximately 0.3% . Based on general practice, neglecting wake effects, the model should not be any larger if it is used in this tunnel.

A NACA 0025 aerofoil profile was chosen for this study. A symmetric section was chosen so that positive, negative, or zero α tests could be done without introducing camber effects. The standard symmetric shape also allows both upper and lower mold halves to be made with the same pattern. Although the 12% or 15% four-digit series symmetric sections are more commonly found in research, the 25% thick section was used as it allows more space for an air supply duct. Larger ducting allows for a wider range of air flow rates to be used without excessive pressure losses. Though this particular profile is not typically used on the inboard section of wind turbine blades, it is common to use relatively thick sections in this region,

which is the region of interest. A side benefit to choosing the NACA 0025 section is that it has a well rounded leading edge that is well suited to the jet flap as noted in Section 2.2.1.

3.1 Pattern and Mold

With the aerofoil section and chord chosen the half-thickness distribution [21] was computed (Equation 3.1). Note this is the equation for an aerofoil of unit chord where y_t and t are expressed as a fraction of the chord. ξ is a dummy coordinate for the chordal distance ($0 < \xi < 1$). The half profile was converted to a set of discrete 0.1×10^{-3} m vertical steps. The steps were designed 'over-sized', so that the exterior corners of the steps could be sanded off to obtain a smooth profile of the required dimensions. The half-profile pattern (Figure 3.1) was machined out of polyvinyl chloride using a vertical-axis milling machine. The pattern was then carefully sanded to a smooth finish.

$$y_t = \frac{t}{0.2}\left[0.29690\xi^{\frac{1}{2}} - 0.12600\xi^1 - 0.35160\xi^2 + 0.28430\xi^3 - 0.10150\xi^4\right] \qquad (3.1)$$

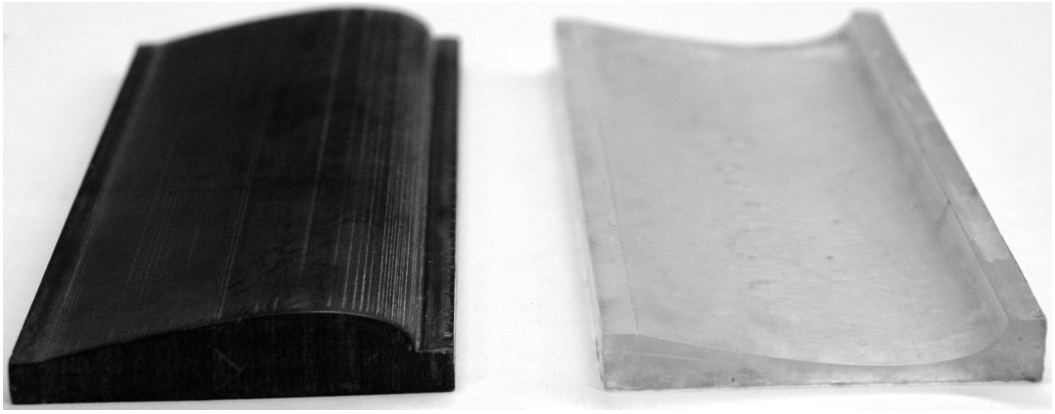

Figure 3.1: Finished half-profile pattern(left) and mold half (right) [22].

Both the mold and models were made with polyester casting resin from Environmental Technology Incorporated. Each mold half (Figure 3.1) was made by casting resin over the pattern to create a negative of the pattern. The models were subsequently made by pouring casting resin in the clamped-together mold halves to produce a positive.

3.2 Models

Before the final experimental model was made several preliminary models were constructed. In general each model consisted of a polyester wing with a 6.35×10^{-3} m steel tube cast in place. The tube served the dual purpose of providing structure and a mounting point for the model, as well as being an air supply duct. Various holes and machined slots were made to allow air ejection at either the leading or trailing edge. Several ideas were tested out in this process which eventually lead to the creation of the final model.

The final design (Figure 3.2) consists of a resin aerofoil with its air supply tube cast 18×10^{-3} m from the trailing edge. A strip of aluminium sheet metal is inset flush to the aerofoil surface at the trailing edge. Prior to bonding the aluminium sheet, an air distribution manifold was machined into both the plastic surface and the supply tube. A 0.397×10^{-3} m drill bit was used to create a row of holes to serve as jet nozzles. Henceforth d is used to symbolize the nominal diameter of the jet holes. Care was taken to maximize the area of the flow passages in order to minimize flow losses.

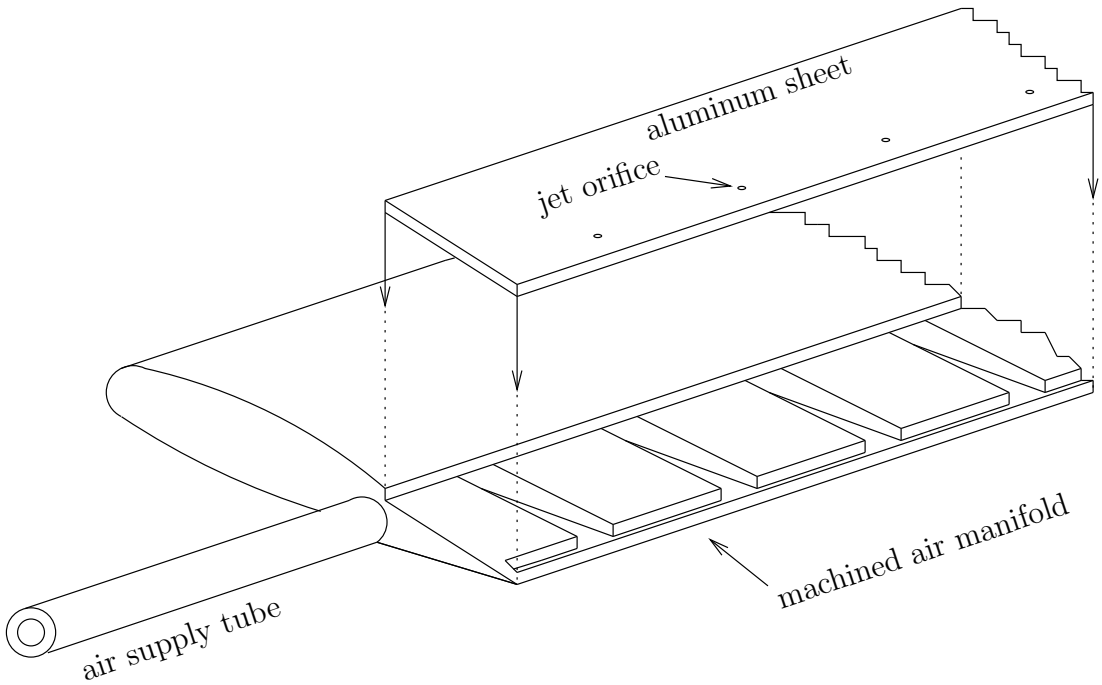

Figure 3.2: Schematic of in-wing air distribution manifold. Note that the chord-wise slots intersect with the supply tube.

In previous studies [6] continuous jet slots have been built into aerofoil models in order to simplify the analysis with ideal two-dimensional flow. In industry however, simple and robust methods are desirable, which is why a row of drilled holes was substituted for a continuous slot. For the same reason simple manufacturing methods were used such as: drilling, routing, molding, and bonding. Chapters 5 and 9 examine the effect the model geometry, and by extension the manufacture, had on the performance of the system.

Figure 3.3 shows the end view of the 'as built' aerofoil. The chord of the aerofoil is 49×10^{-3} m and the thickness is 11×10^{-3} m (23%); slightly shorter and thinner than intended due to the trailing edge modification and shrinkage respectively. The centre of the supply tube is 18×10^{-3} m from the trailing edge and the holes are located 4.5×10^{-3} m (9%) from the trailing edge (Figure 3.4). The jet holes were drilled perpendicular to the aerofoil surface at 5.0×10^{-3} m ($12.5d$) increments. The angle of the jet (θ) was determined to be approximately 1.40 rad (80°) from the measured jet velocity in the jet flow study (Chapter 4). Furthermore the angle of the aerofoil surface at the jet outlets was measured from images captured in the particle image velocimetry experiment (Chapter 6). The surface normal was determined to be approximately 1.36 rad (78°), which is consistent with the above θ. The work of Traub [14] and Nakafuji [16] suggest that placing a control device in front of, rather than at, the trailing edge is acceptable for lift, but creates a drag penalty. The 9% used in the current experiments is much larger than the recommended 2% [16] and so a significant drag penalty is possible. The following experimentation revealed what the true impact on performance was.

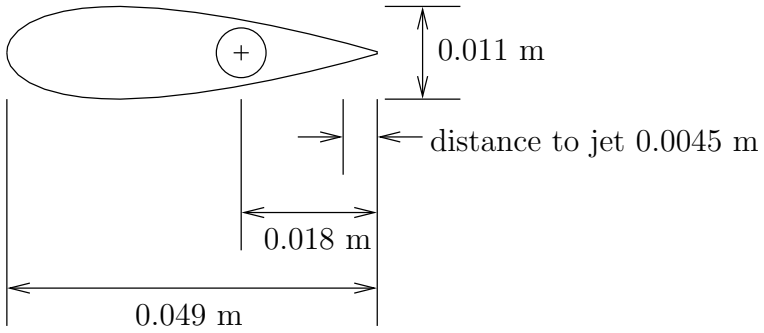

Figure 3.3: Dimensions of the aerofoil.

3.3 Model Air Supply

The compressed air supply (Figure 3.5) was connected through a needle valve. A Bourdon-type pressure gauge and variable area flow meter were connected to the valve with a one inch pipe tee and bushings. It was determined that the flow area

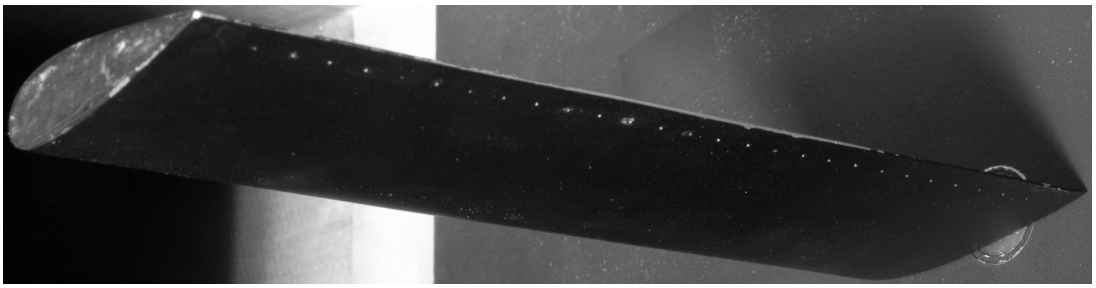

Figure 3.4: Model trailing edge. Note the row of jet outlets [22].

of the tee was large enough such that the measured pressure was approximately equal to its stagnation value. The model supply duct was connected to the outlet of the flow meter via a short length of flexible tubing. As mentioned previously the area of the air supply lines and channels between the needle valve and the jet outlets were maximized to minimize the pressure loss.

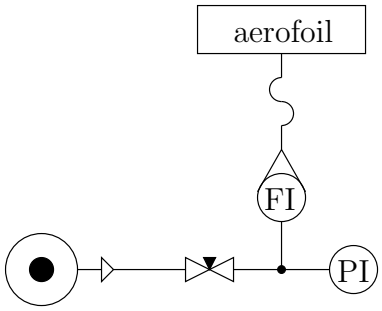

Figure 3.5: Model air supply. Note FI is a flow indicator (Rotameter) and PI is a pressure indicator (Bourdon Gauge)

A direct-read variable-area flow meter is calibrated to read the volumetric flow rate (q_V) at a specific design-flow temperature ($(T_f)_{des}$) and pressure ($(p_f)_{des}$). Since the flow conditions of the air supply are not at design conditions, the following correction factor [23] must be applied.

$$F_{VA} \equiv \frac{q_V}{(q_V)_{des}} = \sqrt{\frac{(\rho_f)_{des}}{\rho_f}} \tag{3.2}$$

Using the ideal gas law the flow density (ρ_f) can be expressed in terms of temperature and pressure.

$$\frac{q_V}{(q_V)_{des}} = \sqrt{\frac{(p_f)_{des}}{p_f} \cdot \frac{T_f}{(T_f)_{des}}} \tag{3.3}$$

According to Cole-Parmer Canada the variable-area flow-meter design pressure is 1.01×10^5 Pa (1 atm) and the design temperature is 294 K (70°F). By again using the ideal gas law to calculate the density, the mass flow rate per unit span is determined. Note s is the jet flapped span in meters and R_{air} is the specific gas constant for air.

$$\dot{m} = \frac{p_f \cdot q_V}{R_{air} \cdot T_f \cdot s} \tag{3.4}$$

Chapter 4

Jet Flow Study Setup

Laser Doppler anemometry (LDA) also known as laser Doppler velocimetry (LDV) is a point measurement technique that is useful to determine time-resolved velocity at a particular location. For the purpose of the current research this method was used to determine the velocity profile of the jets, check the span-wise uniformity of the jets, and to correlate the jet velocity against the stagnation pressure of the flow.

The jet velocity must be known in order to calculate C_μ. For an aerofoil this is defined by Equation (2.1). For the purpose of this research the aerofoil-based coefficient was used where the mass flow rate $\dot{m}$ was per unit span and the chord c was used as the physical scale. The alternative definition uses the wing plan-form area and total mass flow. Both definitions are given by Korbacher [7].

The aerofoil model was mounted horizontally in the wind tunnel as in Figure 4.1. The chord-line of the aerofoil was aligned parallel to the upper and lower tunnel walls. Optical access to the flow was through the glass front wall of the test section. Refer to Figure 4.2 for a schematic of the LDA measurement plane with respect to the aerofoil.

4.1 Particle Seeding

Both the LDV and the PIV methods require that the tunnel air flow be seeded with particles that scatter light. Refer to [24] and [25] for details on particle seeding and scattering. Smoke was introduced into the wind tunnel upstream of the fan as described by Sperandei [18] and allowed to recirculate through the tunnel and mix before entering the test section. During the LDA experiments the tunnel fan was not turned on, as the purpose was to characterize the jets in isolation. Thus the air recirculation was caused by the momentum injection of the jets only. The jets were not seeded with smoke due to the risk of condensation or deposition of the smoke in the small flow passages, and also the possible thrust loss effect on the jets mentioned by Korbacher [7]. Since the air supply was not seeded, particles could

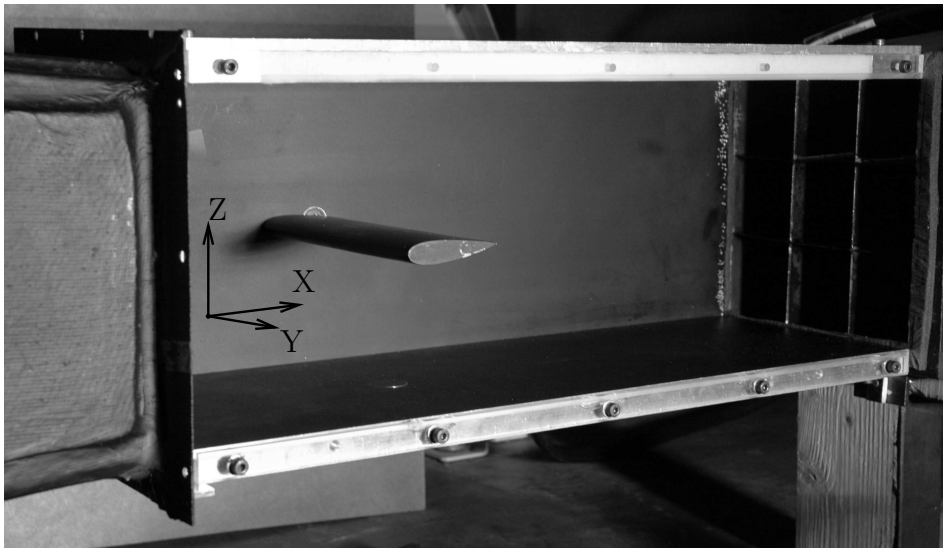

Figure 4.1: Aerofoil model mounted in test section. Note in the lift experiment (Chapter 9) glass walls were used on the top and bottom of the test section. Note flow is from left to right [22].

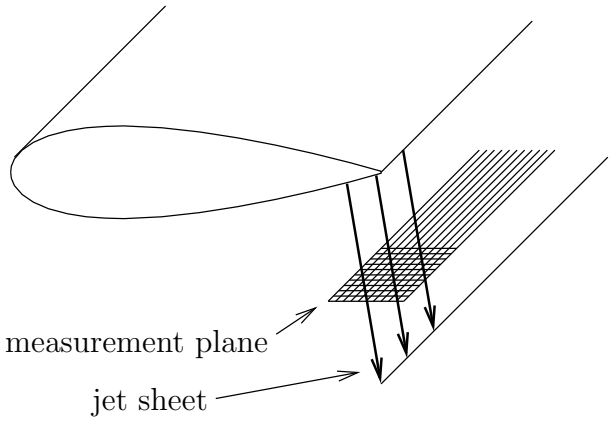

Figure 4.2: Schematic of aerofoil and LDA measurement plane.

only be entrained into the jet flow from the tunnel air. For this reason the core of the jet in the developing flow region near the orifice could not be measured.

The 'smoke' used to seed the flow in the LDA investigation, as well as the later PIV experiment, was vapourized glycerin. The type 100A glycerin-water mixture was supplied by Corona Integrated Technologies Inc. and was vapourized with a Red Devil smoke machine made by Le Maitre Special Effects Inc. Glycerin vapour was used as it is less irritating and considered safer than vapourized mineral oil or other forms of 'smoke'. Glycerin vapour has the disadvantage of condensing easily on contact with surfaces and therefore does not persist as long as vapourized mineral oil. Periodic injection of smoke during LDA data acquisition was required due to the continual purging of tunnel air by the air supply and the condensation of the glycerin.

As LDA and PIV require optical access to the test section, any smoke that condenses on the interior of the window will refract the laser and degrade the results. For this reason the end of the aerofoil model was placed flush against the glass front plane to minimize recirculation in this region.

4.2 LDA Probe Details

For this study a Dantec Dynamics FiberFlow two-dimensional back-scatter differential LDA probe was used. The light source was a Coherent Innova 70 argon-ion laser. This type of anemometer uses a beam splitter, a Bragg cell, and other optics to produce two pairs of intersecting laser beams. One beam pair is green and the other pair is blue. The virtual interference fringes of the beam pairs effectively form ellipsoidal measurement volumes as seen in Figure 4.3. This volume is described by three diameters. The diameters are: $2w_0$, $2w_0/cos\left(\frac{\phi}{2}\right)$, and $2w_0/sin\left(\frac{\phi}{2}\right)$ where $2w_0$ is the beam waist diameter.

The half width of a Gaussian beam at arbitrary distance l from the waist is calculated with $w(l) = w_0\sqrt{1+\left(\frac{l\lambda}{\pi w_0^2}\right)^2}$ [26]. Note that l is the length along the beam $\left(l = \sqrt{(d_s/2)^2 + f^2}\right)$. Since w_f is known then w_0 can be calculated for a given wavelength (λ). The calculated dimensions of the probe volume for the two wavelengths are listed in Table 4.1. Refer to Table A.1 for a list of the geometric beam parameters and their values.

Table 4.1: Dimensions of the probe volumes

$\lambda \times 10^9$ [m]	$2w_0 \times 10^6$ [m]	$2w_0/cos\left(\frac{\phi}{2}\right) \times 10^6$ [m]	$2w_0/sin\left(\frac{\phi}{2}\right) \times 10^6$ [m]
514.5	$47.8 \pm 1\%$	$48.2 \pm 1\%$	$396 \pm 2\%$
488.0	$45.3 \pm 1\%$	$45.7 \pm 1\%$	$376 \pm 2\%$

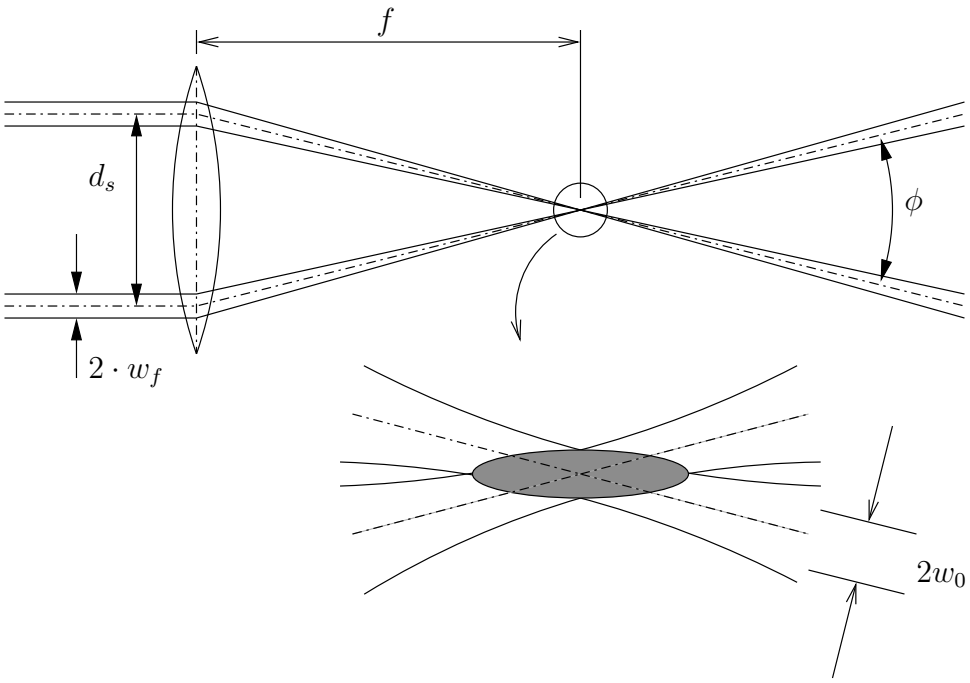

Figure 4.3: LDA probe geometry showing beam waists and ellipsoidal measurement volume.

Whereas Figure 4.3 shows two intersecting beams forming one volume the probe actually consists of two orthogonal beam pairs forming two intersecting measurement volumes. Light signals were received from both measurement volumes, however these signals were only considered valid if they were coincident in time. Thus the overlap of the two spheroids defined the measurement volume. Projected onto the X-Z plane this would appear as two crossed ellipses with the major axes aligned to $\pm 45°$. For the sake of simplicity this cross-section is approximated by a circle of 48.2×10^{-6} m diameter. Thus the composite measurement volume is bounded by a prolate spheroid of minor diameter 48.2×10^{-6} m and major diameter 396×10^{-6} m.

One consequence of the three dimensional LDA beam geometry (Figure 4.3) is the difficulty of measuring near walls. The area of interest extends along the span of the aerofoil (Figure 4.2) near the lower surface. Proximity of measurements to the surface is limited by the intersection of the laser beam(s) with the tip of the aerofoil. This is of course due to the non-zero beam intersection angle (ϕ). The nearer the measurement volume is to the rear wall, the further it must be from the aerofoil surface. In each test an effort was made to measure as close as possible to the outlet of the jets. Consequently flow measurements at the mid span could be made slightly closer than those of the full span.

Chapter 5

Jet Flow Validation

The purpose of this chapter is to review the velocity measurements of the air jets, and determine if they behave adequately and as predicted. With exception to the flow rate calibration test (Section 5.4), all of the other jet flow measurements used a medium mass flow rate of 12×10^{-3} kg m^{-1} s^{-1}. Herein the basic jet profile is reviewed in detail, the variation in the full set of jets is examined, the momentum of the jet is integrated over the measured area to check for conservation, and the jet momentum is compared with flow rate. In the following analysis both global wind-tunnel coordinates (X,Y,Z) and local jet-centric coordinates (x,y,z) are used depending on which is more useful. Both global and local coordinates are *aligned* in the *same direction*. Refer to Figure 4.1 for global wind-tunnel coordinates and Figure 5.1 for jet-centric coordinates.

5.1 Jet Velocity Profile

The jet velocity profiles are seen in Figures 5.2(a) and (b). The local coordinates are non-dimensionalized with the jet nozzle diameter (d). As expected the jet profile spreads laterally with distance from the outlet and merges with the adjacent jets. Between 5.2(a) and (b) the peaks decrease and the troughs increase, and thus the distribution of momentum becomes more uniform.

It is interesting to note that the vertical component of the velocity is increased on the downstream side of the jet (Figures 5.3(a) and 5.9). The horizontal component, however varies in the stream-wise direction, so that it is directed towards the jet core on both sides of the jet (Figure 5.3(b)). Clearly this is air being entrained into the jet.

The core of the jet is directed at an angle of $\theta = 80°$ from the aerofoil chord. This is 2° steeper than the measured value in Section 3.2. This being said $sin(\theta)$ changes only 0.8%, so the difference in the lift coefficient should be negligible. This provides some confirmation of the jet deflection angle, though it is possible that this initial angle could change slightly with nonzero free stream velocity.

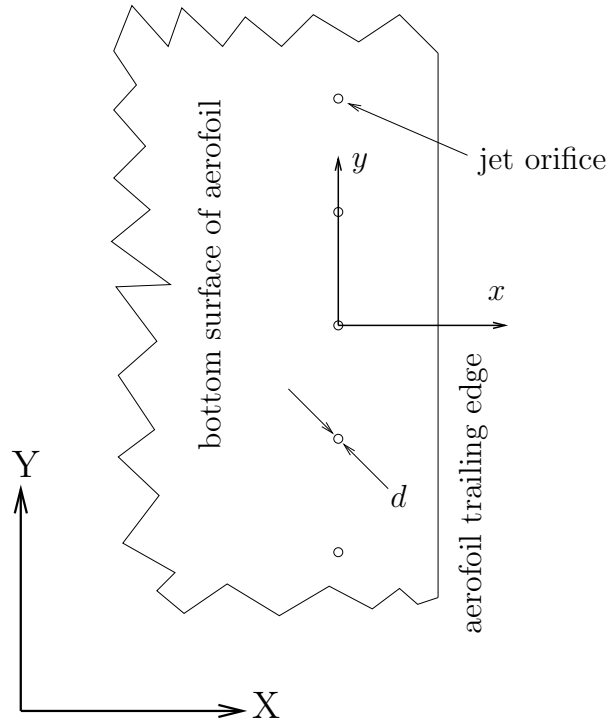

Figure 5.1: Local coordinate system. Note that x, y is aligned with X,Y.

5.2 Span-wise Jet Flow Uniformity

In order to determine the uniformity of the jet flow in the span-wise direction two surveys were done. The first survey consisted of chord-wise traverses across the nominal position of each of the 27 holes. The second more complete survey was a full grid across the span (Figure 4.2). The global coordinates of the first survey are summarized in Table 5.1. The results of this test revealed that there are slight variations in the jet ejection angle along the span, and hence the location of peak velocity. This is likely due to manufacturing variability in the drilled jet holes. The variation between jets demonstrated the need for a full-grid survey to properly characterize the jet flow. The data also revealed that three of the jets were partly plugged with debris; possibly from manufacture. An attempt was made to clear these jets.

Table 5.1: Full span centre line survey.

Direction	Start position $\times 10^3$ [m]	End position $\times 10^3$ [m]	$\Delta \times 10^3$ [m]
X	161.0	171.0	1.0
Y	12.9	142.9	5.0
Z	61.2	-	-

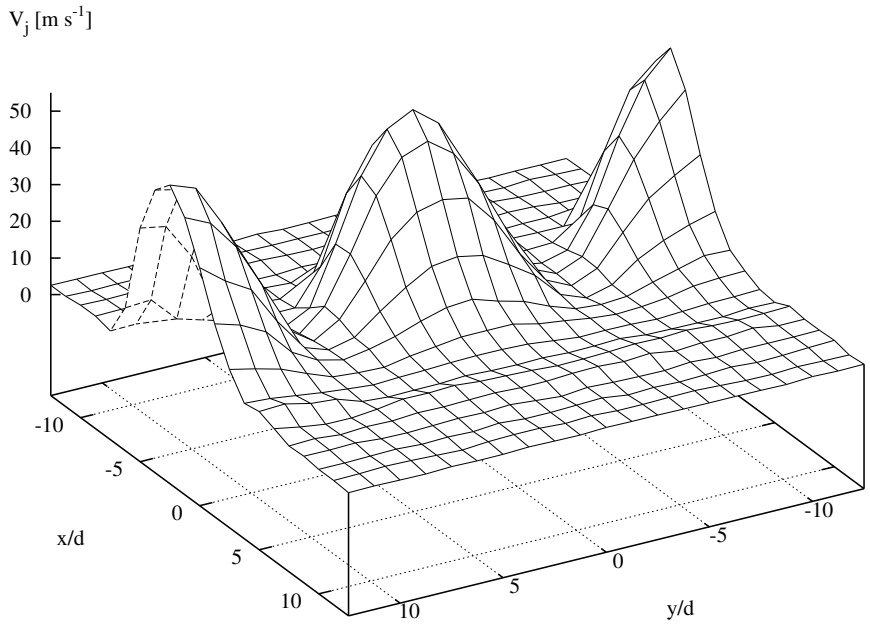

(a) 24 diameters downstream of jet orifice

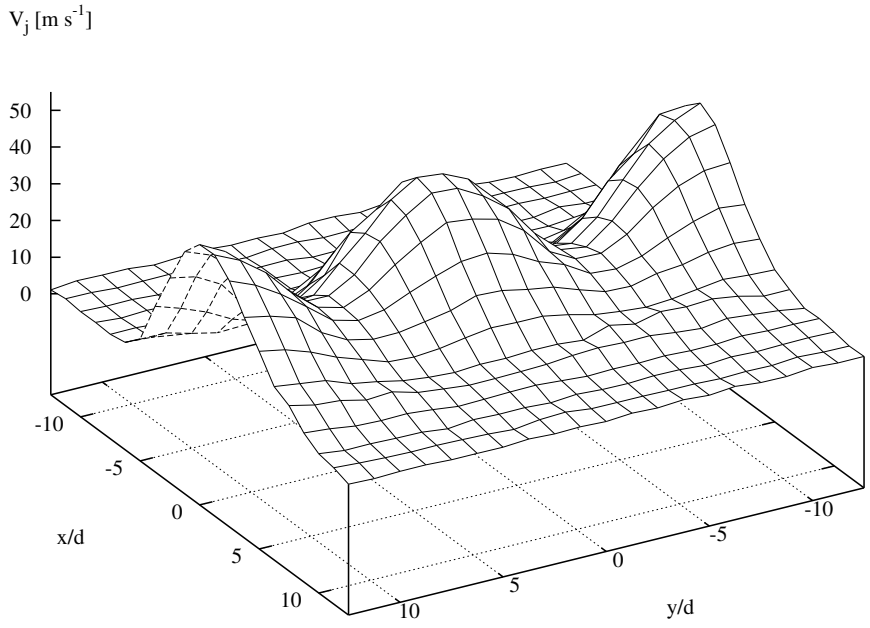

(b) 38 diameters downstream of jet orifice

Figure 5.2: Velocity field *magnitude* at given distance from jet orifice. Note raw data presented with no smoothing or interpolation. Grid spacing was 0.5×10^{-3} m in both x and y directions.

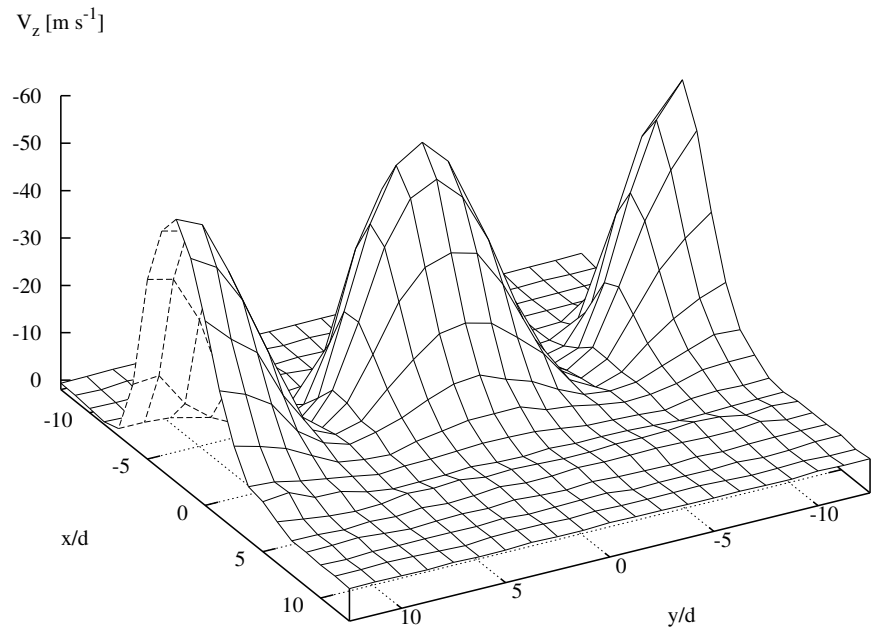

(a) Note velocity increase in stream-wise (x) direction.

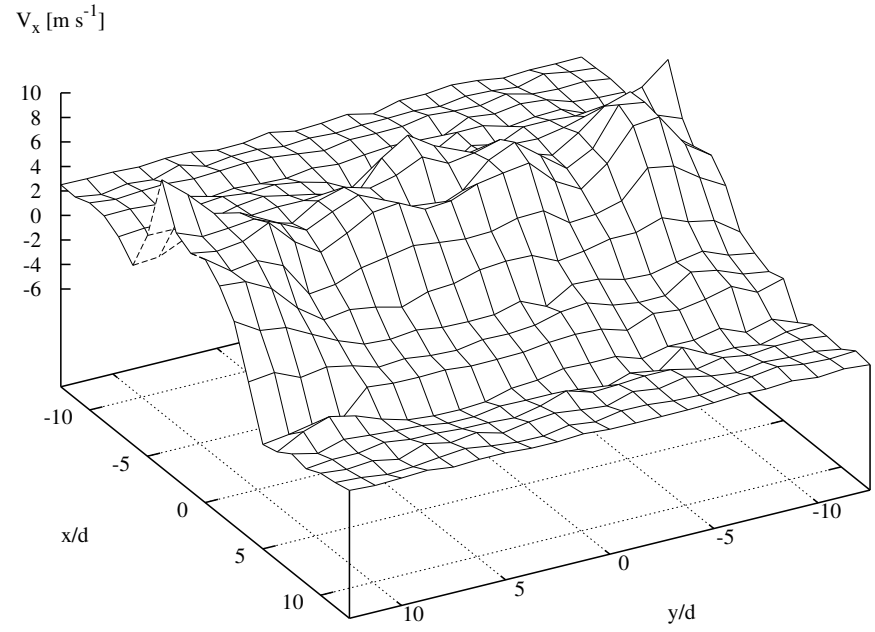

(b) Note entrainment of fluid into the jet. Velocity is positive upstream ($x < 0$) and negative downstream ($x > 0$) of the jet.

Figure 5.3: Velocity field *components* at 24 diameters downstream of jet orifice.

For the above reasons a full-resolution grid was subsequently run (Figure 5.4). This second velocity survey required a considerable investment of time (1507 grid points). The global coordinates of the second survey are summarized in Table 5.2. Examining Figure 5.4 reveals that the discrete jets create a velocity field somewhat similar to a sheet, but with significant spatial variation in the span-wise direction. There is no overall decreasing trend along the span of the aerofoil, which indicates that the manifold pressure drop along the span is negligible. The variation of the jet flow is attributed to variation from one orifice to another. Note it can be seen in Figure 5.4 that one of the jet orifices at Y = 122×10^{-3} m was still plugged during this test. Unfortunately due to equipment availability this grid could not be re-run, however it was decided that sufficient good data were acquired across the span to be useful. The data in the immediate vicinity of the plugged jet were not used in subsequent analysis.

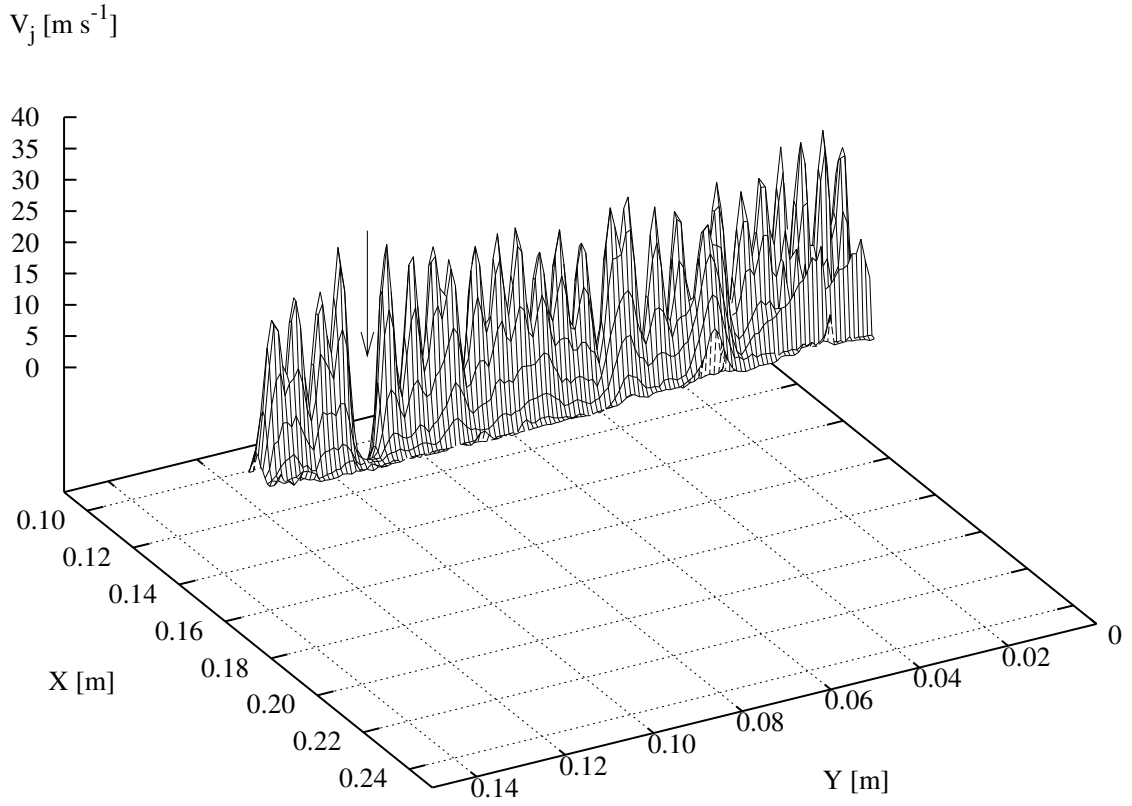

Figure 5.4: Full span flow field in global coordinates 43 diameters from the aerofoil surface. Note arrow indicating position of plugged jet.

To analyze these data the global coordinates were mapped to local coordinates for each jet as: X $\rightarrow x$, Y $\rightarrow y$, since there is spatial correspondence due to the repeated geometry (Figure 5.5). An average jet velocity profile was calculated with Equation 5.1, where $\mathbf{V_{x,y,n}}$ is the velocity at location (x, y) of the n^{th} jet. The

Table 5.2: Full span grid survey.

Direction	Start position $\times 10^3$ [m]	End position $\times 10^3$ [m]	$\Delta \times 10^3$ [m]
X	162.5	172.5	1.0
Y	9.9	145.9	1.0
Z	59.0	-	-

averaged jet profile is seen in Figure 5.6. Similarly the local standard deviation is calculated with Equation (5.2) and seen in Figure 5.7.

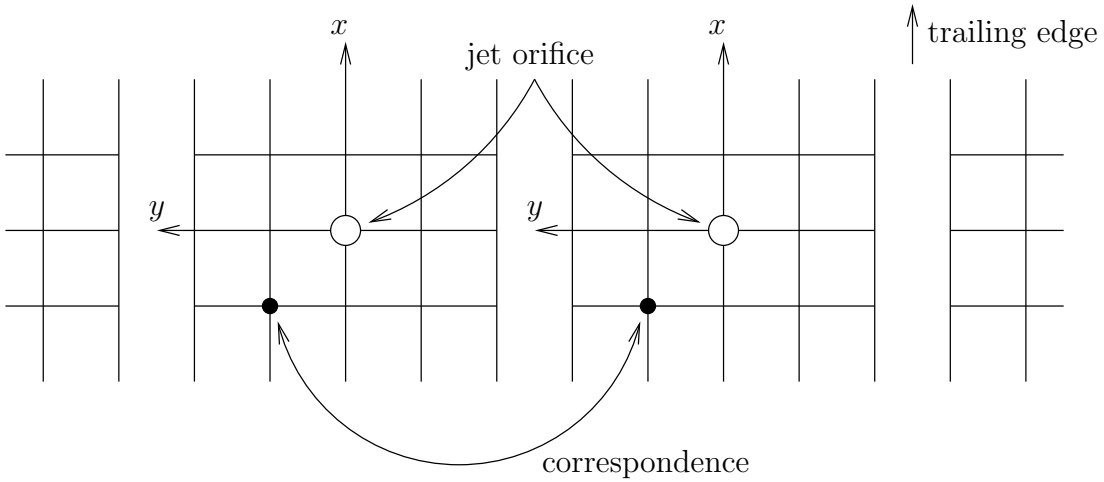

Figure 5.5: Repeated jet geometry as viewed from bottom. Note spatial correspondence between grids.

$$\overline{\mathbf{V}}_{\mathbf{x,y}} = \frac{1}{26} \sum_{n=1}^{26} \mathbf{V}_{\mathbf{x,y,n}} \tag{5.1}$$

$$\boldsymbol{\sigma}_{\mathbf{x,y}} = \sqrt{\frac{1}{26} \sum_{n=1}^{26} \left(\mathbf{V}_{\mathbf{x,y,n}} - \overline{\mathbf{V}}_{\mathbf{x,y}} \right)^2} \tag{5.2}$$

Even without calculating $\boldsymbol{\sigma}_{\mathbf{x,y}}$ it is easy to see considerable span-wise non-uniformity in Figure 5.4. Table 5.3 compares the maximum of each velocity component of the averaged jet profile to the maximum standard deviation of that component. From this it is seen that the variation in the chord-wise direction (x) of the jet flow is larger than the average speed. With the wind tunnel fan not running, a low and highly variable chord-wise flow speed is not unexpected. The ratio of

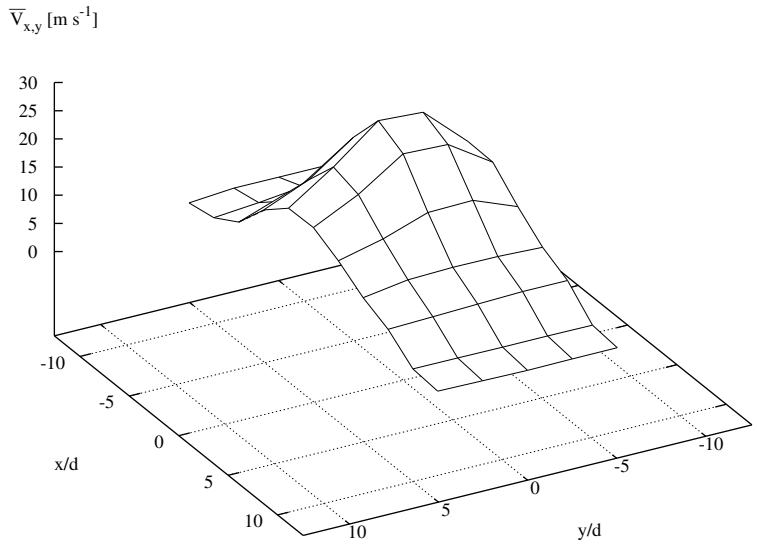

Figure 5.6: Average magnitude of all jets in local coordinates excluding blocked one.

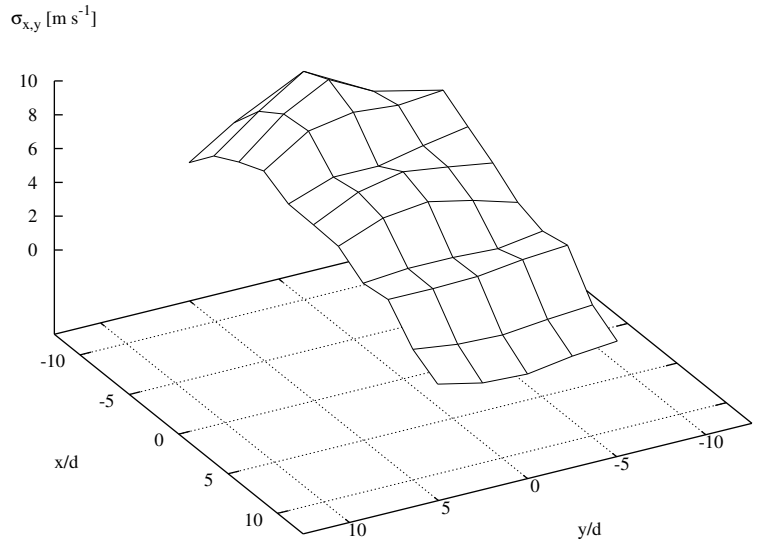

Figure 5.7: Standard deviation of jet velocity magnitude.

σ_x over V_x should be smaller with $U_\infty > 0$. In the jet axial direction there is less variation in the flow speed, however it is still about one third of the mean value. One can easily see from these data that the series of jets do not closely simulate a blowing slot, though this does not necessarily imply ineffectiveness. The variation in the jets introduces three dimensionality into the flow and increases uncertainty in correlations with C_μ. This three-dimensionality could cause increased mixing, more rapid jet decay, or other unknown effects.

Table 5.3: Comparison between maximum velocity and maximum standard deviation.

Direction	Maximum $\overline{\mathbf{V}}_{\mathbf{x,y}}$ [m s^{-1}]	Maximum $\boldsymbol{\sigma}_{\mathbf{x,y}}$ [m s^{-1}]
x	4.82	5.75
z	-27.4	9.48
Magnitude	27.6	9.18

5.3 Jet Momentum Integration

Using Simpson's rule for double integrals (Equation 5.3) the momentum of the jet was calculated. The derivation [27] of the rule shows that the weighting factor W follows a simple pattern as shown below. At low supply pressures, below that required to achieve the critical pressure ratio ($\frac{p_f}{p_{atm}} = 0.5283$) [28], the flow from a convergent nozzle should expand fully to atmospheric pressure at the outlet. This fact is easily seen by examining compressible flow tables. At higher supply pressures there will be some expansion beyond the jet outlet due to the sonic condition at the throat.

$$\dot{\mathbf{M}} = \int\int \rho V \mathbf{V} dx dy = \tfrac{1}{9}\Delta x \Delta y \textstyle\sum_{x,y} (W \cdot \rho V \mathbf{V}) + O(\Delta x^4) + O(\Delta y^4) \quad (5.3)$$

$$W = \begin{bmatrix} 1 & 4 & 2 & 4 & \dots & 2 & 4 & 1 \\ 4 & 16 & 8 & 16 & & 8 & 16 & 4 \\ 2 & 8 & 4 & 8 & & 4 & 8 & 2 \\ 4 & 16 & 8 & 16 & & 8 & 16 & 4 \\ \vdots & & & & \ddots & & & \\ 2 & 8 & 4 & 8 & & 4 & 8 & 2 \\ 4 & 16 & 8 & 16 & & 8 & 16 & 4 \\ 1 & 4 & 2 & 4 & & 2 & 4 & 1 \end{bmatrix}$$

The results of momentum integration at distances: $24d$ (10×10^{-3} m) and $38d$ (15×10^{-3} m) (Figures 5.2(a) and (b)) are listed in Table 5.4. Immediately obvious

on examining the momentum results is that momentum is *apparently* not conserved with increasing distance from the jet outlet. Momentum must be conserved however, and free jets are no exception [29]. This suggests therefore, that there is some error in the measurements or the calculations. The uncertainty on $\dot{M}$ was computed to be 10% at $24d$ and 8% at $38d$ (Section A.2). Thus the discrepancy between the momentum flux at the two cross sections is outside of the experimental uncertainty and statistically significant. Although a decrease in measured momentum with distance could be explained by some unaccounted loss or simply the diffusion of momentum outside the measured area, an increase should not occur since the jet itself is the only source.

Table 5.4: Momentum integrated over the cross-section. Note this is the momentum of one full jet plus two half jets.

Distance [ ]	$\dot{M}_x \times 10^3$ [kg m s^{-2}]	$\dot{M}_z \times 10^3$ [kg m s^{-2}]	$\dot{M} \times 10^3$ [kg m s^{-2}]
$24d$	-2	25	25
$38d$	-4	35	35

Since the momentum of the jet is proportional to the square of the velocity, it is particularly important to measure the peak velocity correctly. One potential problem is with the relative sizes of the LDA measurement volume and the jet. As already seen, the coincident measurement volume could be described as a spheroid of major dimension 396×10^{-6} m and minor dimension 48.2×10^{-6} m. Examining the flow fields presented in Figures 5.2(a) and (b) it is seen that the width of the jets are roughly $10d$ (4×10^{-3} m). Hence in the stream-wise direction the probe width is approximately 1% of the jet width, but in the span-wise direction the probe is 10% of the jet width. The length of the probe (396×10^{-6} m) is comparable to the grid spacing Δy of the jet measurement (Figure 5.2(a) and (b)), which is 500×10^{-6} m. The result of a long probe in the span-wise direction is spatial averaging in this direction and possibly bias due to nonuniform particle seeding. If the particle seeding were non-uniform, and the cores of the jets had a lower concentration, then one would expect that the measured velocities would be biased low. With uniform seeding and a large probe there is an equal chance of measuring a 'fast' or 'slow' particle and averaging them. With nonuniform seeding there is a greater chance of measuring the 'slow' particle, so the average is consequently lower. An examination of the data rate shows a decrease in the rate at the location of each jet core in the near field ($24d$) but not the far field ($38d$). Unfortunately no data were collected on the time variation of the tunnel seeding. Thus it is possible, though unlikely, that the temporal variations coincided with the measurement of those particular grid locations. Refer to Figures A.1(a) and (b) for the data rate surfaces.

5.4 Jet Momentum Comparison

The final LDA test conducted was intended to relate the momentum of the jet sheet to the measured flow rate ($(q_V)_{des}$). The jet momentum can be calculated using the mass flow rate ($\dot{m}$), pressure (p_f), and an assumption of isentropic flow. Since the aforementioned method relies on an assumption, an independent LDA based method was used for comparison. Velocity measurements were taken over three grids surrounding the first, middle, and last jets over the full range of jet flow rates. The distance from the aerofoil surface was $43d$. Due to time constraints, the size of the grids were limited, hence only the velocity around the core of the jets were measured. With the additional distance and the limited grid size, the whole jet profiles were not captured. It was therefore not possible to numerically integrate the velocity field to obtain the jet momentum.

If the shape of the velocity profile were known, it might be possible to calculate the total momentum of the jet, given that the maximum velocity was measured. An attempt was made to fit a curve to the full jet velocity fields presented in Figures 5.2(a) and (b). A reasonable hypothesis is that the velocity field of a single jet in isolation is approximately Gaussian [29] in form far downstream in the fully developed region. According to Pope [30] the profile of a round jet develops by about $25d$ and a jet sheet by $40d$. It is further reasonable to assume that superposition can be applied to determine the response of the entire row of jets and that the response resembles both the round jet and the jet sheet. The equation for the two dimensional Gaussian jet profile is:

$$V_j(x,y) = V_{j,max} \cdot e^{ln(0.5)\cdot\left[\left(\frac{x}{w_x}\right)^2+\left(\frac{y}{w_y}\right)^2\right]} \tag{5.4}$$

where $V_{j,max}$ is the maximum velocity of the jet and (w_x, w_y) are the half-widths of the jet. Refer to Section A.5 in the appendix for the development of this equation.

The half-widths of the jets in both profile surveys (Figures 5.2(a) and (b)) were measured and tabulated in Tables A.2 and A.3. The half-width w_y differs from w_x due to interaction with the adjacent jets in the y direction. The average w_x and w_y are listed in Table 5.5 below. The average peak velocities are 53.8 m s^{-1} and

Table 5.5: Average half-widths of the jets at two distances.

Distance		$\overline{w}_x$		$\overline{w}_y$	
[mm]	[ ]	[mm]	[ ]	[mm]	[ ]
10	$24d$	1.2	$3.0d$	1.3	$3.3d$
15	$38d$	1.7	$4.3d$	2.0	$5.0d$

43.7 m s^{-1} for the near and far locations respectively. If the square of Equation 5.4 at three different grid locations is summed, then the square root of the sum gives

an approximation of the composite velocity field.

$$V_J(x,y) \approx \sqrt{[V_j(x, y - 0.005 \text{ m})]^2 + [V_j(x,y)]^2 + [V_j(x, y + 0.005 \text{ m})]^2}$$

Using the measured w_x, w_y, and $V_{j,max}$, the profile shown in Figure 5.8 results.

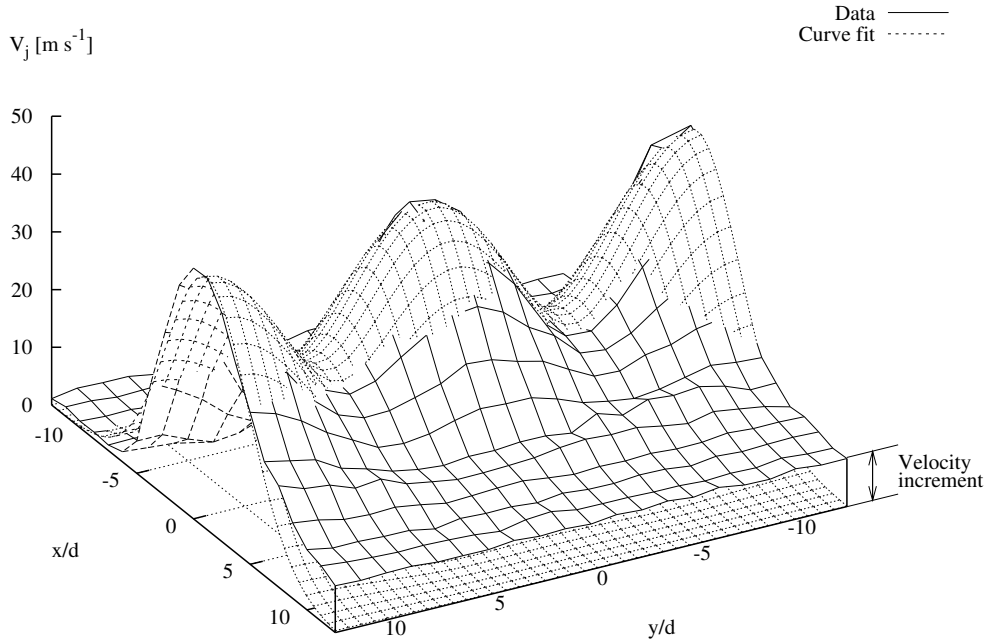

Figure 5.8: Gaussian curve overlaid on experimental jet profile at 38 diameters downstream of the jet orifice. Note velocity increment in the x direction due to co-flow.

Note that Figure 5.8 is presented to convey the *idea* of superposition of the jets. Since the momentum is proportional to the square of the velocity, the square root of the sum-of-squares is used rather than a direct summation. This is not a 'proper' solution, but despite its crudeness, it fits the experimental data rather well. The only feature not captured is the stream wise (x direction) increment in velocity across the jet. This velocity increment is seen in Figure 5.8 and is approximately 10 m s^{-1} at position $\frac{x}{d} = 12.5$.

Based on the average w_x and w_y from the two experiments the linear spreading rates are approximately 0.092 and 0.13 in the x and y directions respectively. For a turbulent round jet Pope [30] gives spreading rates of 0.096, 0.102, and 0.094 from three different experiments. Pope also gives 0.10 as an approximate spreading rate for a jet sheet. The spreading rate in the x direction is slightly lower than both that of a round jet and a two dimensional sheet, while the y direction spreading is higher. The slight discrepancy is almost certainly due to interaction with the adjacent jets, since this is not a single jet in isolation. Since the spreading rate is

independent of the Reynolds number [30], these values are used to extrapolate the width of the jet in the final experiment.

By integration of Equation 5.4 the momentum of a single jet is:

$$\dot{M} = \int_{-\infty}^{\infty}\int_{-\infty}^{\infty} \rho V_j^2 dxdy = \frac{\pi\rho(w_x w_y)V_{j,max}^2}{-2 \cdot ln(0.5)} \tag{5.5}$$

Refer to Section A.6 for details of the integration. The measured stagnation pressure (p_f) and flow rate (q_V) are listed in Table A.4. Using Equation 3.4 the mass flow of the jet was calculated. Using the ratio of absolute pressure between the gauge and atmosphere, isentropic compressible flow relations, and air properties the velocity of the flow at the orifice can be estimated. Consequently the momentum flux of the jet sheet ($\dot{m}V_j$) per unit span can be estimated. It was found that the momentum of the sheet calculated with Equation 5.5 and that from the isentropic calculations diverged sharply at higher mass flow rates (Figure 5.9).

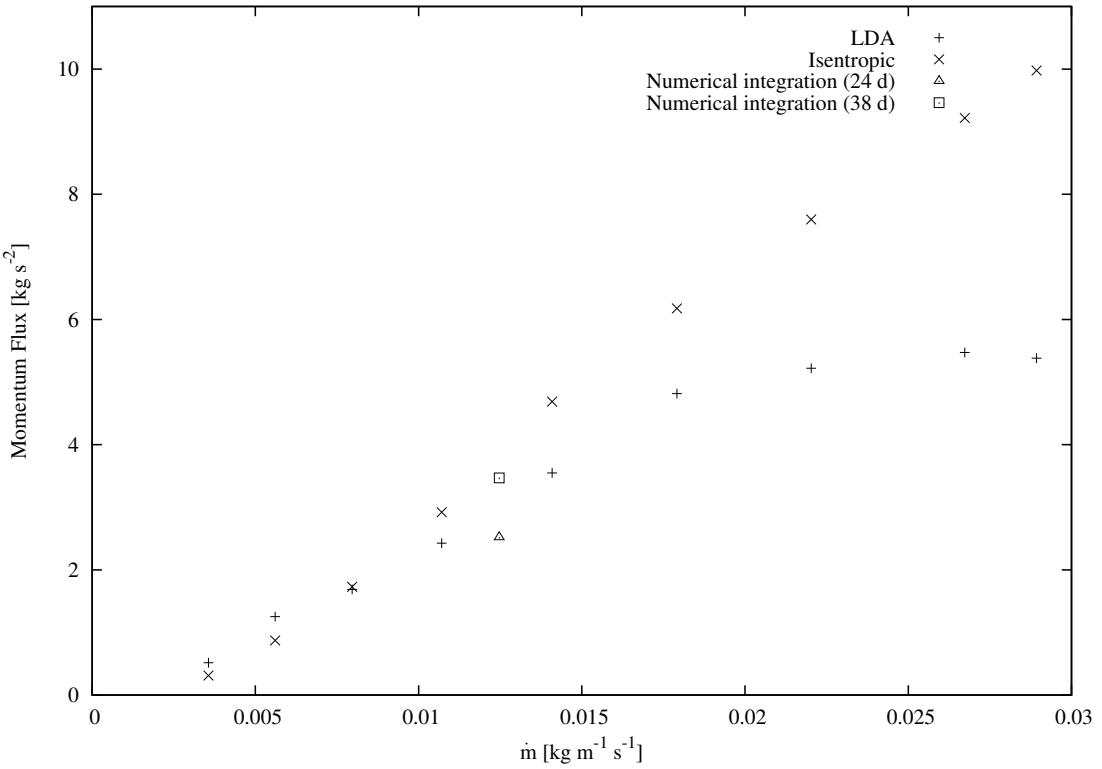

Figure 5.9: Comparison between the jet momentum calculated using the LDA velocity field and the momentum calculated using the isentropic flow assumption. Note the two momentum values integrated directly from the flow field data (Section 5.3) for comparison.

Since the jet orifices are essentially converging nozzles, the flow is less than or equal to the speed of sound at the exit. Over the highest four mass flow rates the

nozzle is choked and the jet speed is constant. Thus in the isentropic case the slope of the data (Figure 5.9) is constant at high $\dot{m}$. The momentum flux calculated from the LDA velocity measurements however is relatively constant over the last four points. Since the nozzle velocity should not decrease with increasing stagnation pressure, the discrepancy must therefore be an error in calculating the momentum or a loss of momentum occurring somewhere between $0d$ and $43d$.

Looking at Equation 5.5 there are $V_{j,max}$, ρ, and the two half widths that could be the source of error. Since the velocity field was measured directly, it seems unlikely that the error on $V_{j,max}$ could account for such a large discrepancy. For example at the highest mass flow rate the isentropic result is approximately 1.85 times the LDA result. This would translate to 26% error on the velocity measurement. It also seems unlikely that the jet flow remains nearly twice as dense as atmospheric air at 43 diameters downstream of the outlet. The greatest uncertainty surrounds the profile of the jet, which is governed by the half widths w_x and w_y. If the profile was much larger than expected, due to some compressible flow phenomena, the calculated momentum could greatly underestimate the true momentum. Though the full profile was not measured, the experimental data and curve fit can still be compared. Figure 5.10 shows the two velocity fields superimposed. It is seen that there is a very good fit between the two surfaces over the range of the collected data. If both half widths were 28% larger then the momentum would match, however this is clearly not the case, since the velocity profile would no longer match.

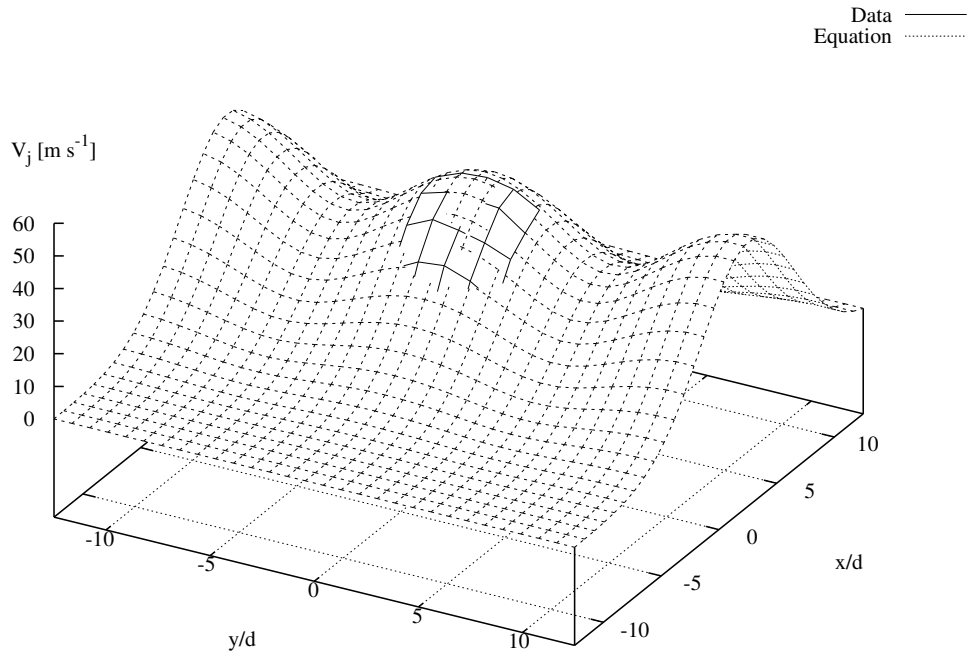

Figure 5.10: Comparison between the LDA velocity measurements at maximum mass flow rate and the Gaussian curve fit.

From the preceding it is concluded that there is a loss in momentum flux downstream of the jet outlets, which limits the momentum observed in the far field. It can further be concluded that this loss is related to compressible flow as it only occurs above the critical pressure ratio ($\frac{p*}{p_f} = 0.5283$).

Chapter 6

Particle Image Velocimetry Experiment

The effect of the jet on the flow over the aerofoil was recorded with the particle image velocimetry (PIV) method. A thorough description of the PIV method is given by Raffel et al. [24]. Digital image pairs of smoke particles in the wind tunnel are captured in rapid succession. During the time interval between frames (Δt), the smoke particles shift position due to the flow velocity. Using a cross-correlation the particle shift (ΔX) between frames is determined for sub regions of the image. An estimate of the instantaneous velocity in each sub region is calculated by $\Delta X/\Delta t$.

6.1 Aerofoil Setup

The model aerofoil was clamped horizontally by the 6.35×10^{-3} m air supply tube at the centre line of the tunnel. Note that the aerofoil was mounted inverted in the tunnel (Figure 6.1) so the positive lift direction is downward. The model was pivoted about the air supply tube to set the angle of attack.

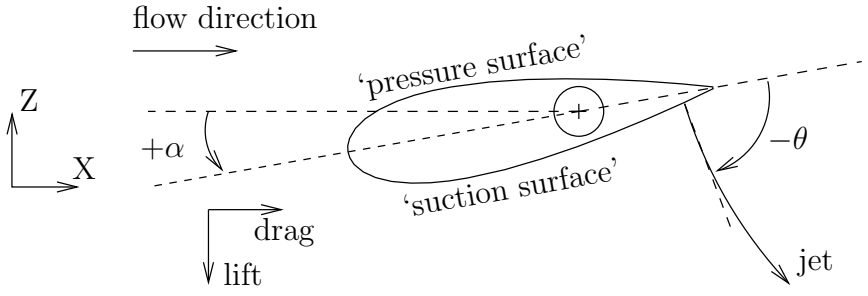

Figure 6.1: Aerofoil angle and force sign conventions.

6.2 Light Sheet Setup

A cross section of the smoke particles in the tunnel flow were illuminated by a laser light sheet. The pulsed light sheet serves both as the camera's 'flash' and its 'shutter'. A Gemini PIV Nd:YAG laser, made by New Wave Research Incorporated, was used as the light source. The laser beam was divided with a beam splitter, spread into two sheets with cylindrical lenses, and reflected into the tunnel test section. Figure 6.2 shows the two light sheets illuminating the flow field from above and below the model. Illumination from both sides was required to avoid a shadow directly above or below the aerofoil.

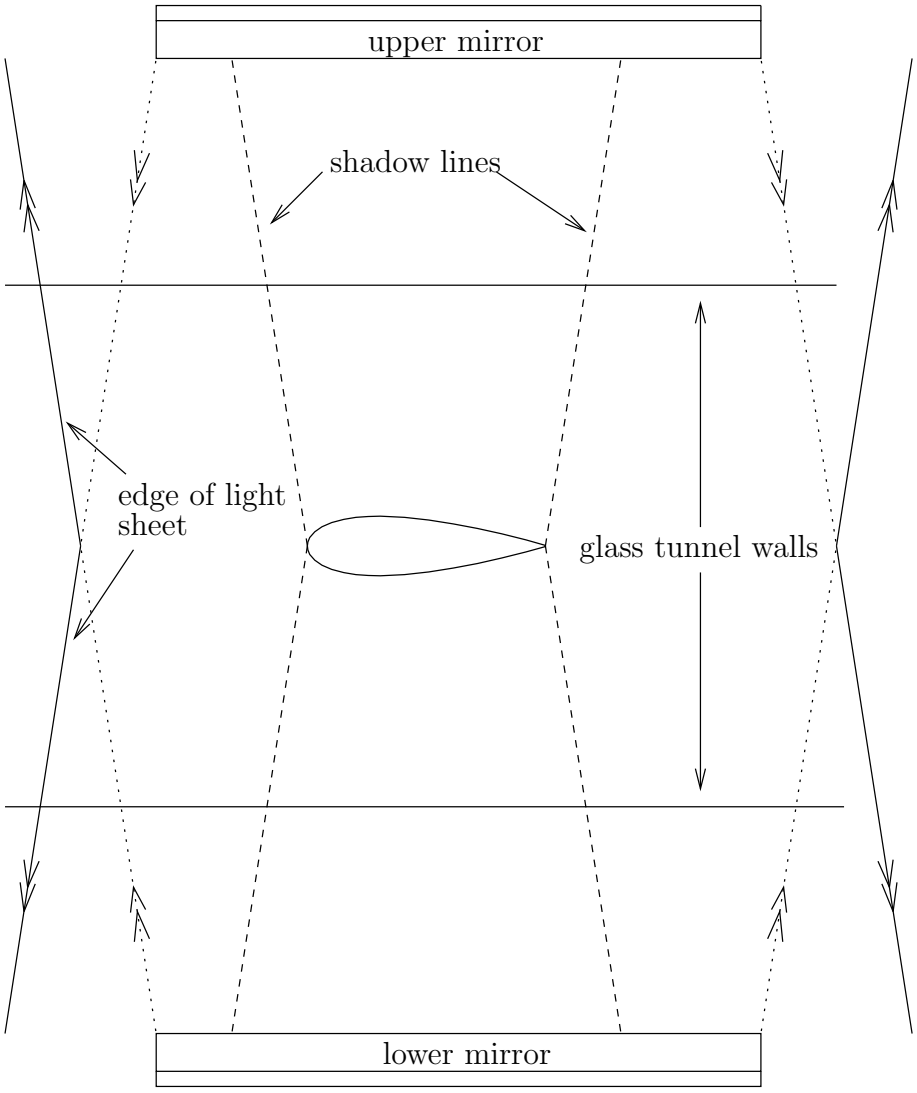

Figure 6.2: Front view of double light sheet used in PIV experiment. Note the two sheets are coplanar.

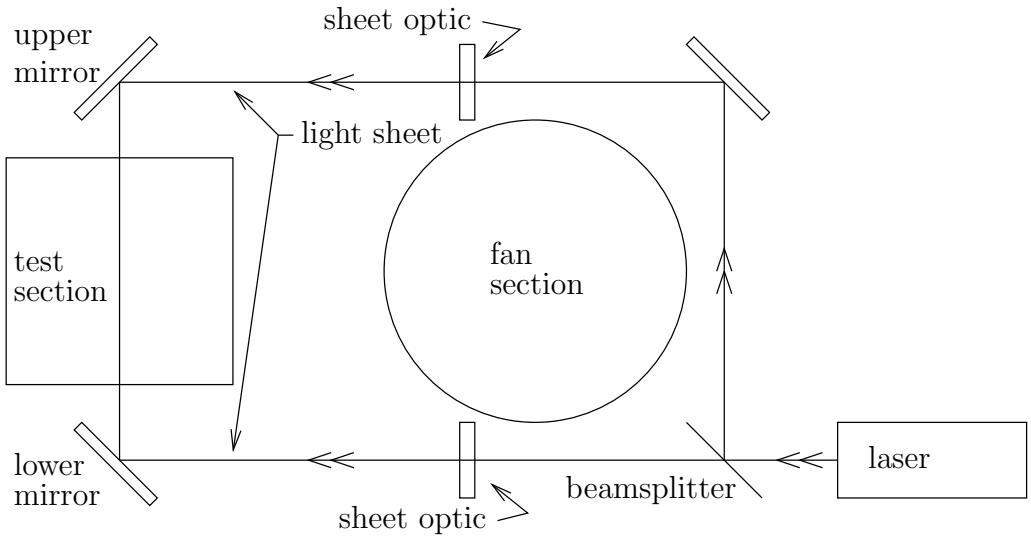

Figure 6.3: Side view of optical layout used in PIV experiment. Note light sheets are perpendicular to the page.

6.3 Camera and Data Acquisition System Setup

The camera used to capture the flow was a Kodak MEGAPLUS ES 1.0 which has a resolution of 1008 by 1018 pixels. The synchronization of the camera and laser, as well as the data acquisition was done using a FlowMap 1100 PIV processor and the FlowManager 3.12.08 software made by Dantec Dynamics A/S.

The camera was set up on a heavy steel table in front of the tunnel test section (Figure 6.4) and was positioned such that the entire height of the test section was imaged. The camera was then carefully focused on the mid-plane of the tunnel.

The scale factor for the images was determined by recording an image of a ruler set perpendicular to the camera at the focal plane. The camera, viewing area, and scale factor was checked before each set of tests to assure the setup remained unaltered. Based on the camera resolution, a standard 32 by 32 pixel interrogation area, and a 50% overlap of interrogation areas, a 62 by 62 vector field can be computed. In the current experiment that translates to each vector representing an area of approximately 2.7×10^{-3} m by 2.7×10^{-3} m.

6.4 Experimental Cases

In the flow control experiment three parameters were varied: C_μ, α, and Re.

Eleven jet flow cases were chosen based on the gradations of the direct-read flow meter. The flow rates listed in Table A.4 have been converted to SI units and

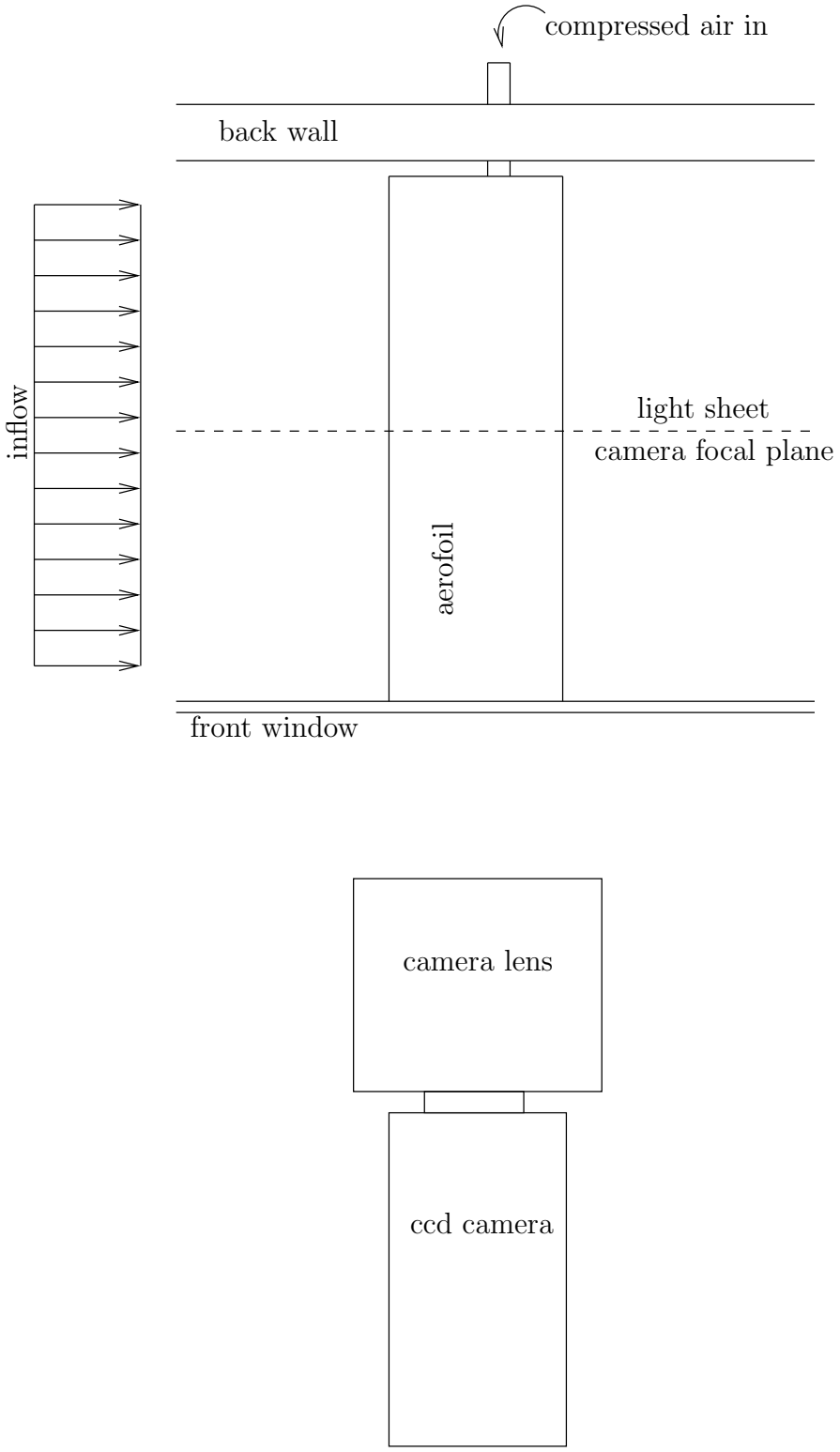

Figure 6.4: Top view of PIV setup.

corrected for temperature and pressure as described in Chapter 3.

The wind tunnel fan was controlled by a variable frequency drive. The chosen drive frequencies for the experiment were the maximum possible (60 Hz) and 20 Hz. Thus half the data were collected at maximum Reynolds number and the other half at approximately 30% of maximum. This was done in an attempt to distinguish Reynolds number effects from α effects and jet momentum effects. The high and low speed cases resulted in an overlap in C_μ over a useful range.

The nominal angles of attack chosen were 0°, +5°, +10°, +15°. The 15° case was included at the suggestion that the 10° case might not fully capture the stall behaviour of the system. The angle of attack is altered as a result of tunnel interference effects and the three dimensional nature of the flow. In the following sections it must be remembered that when angle of attack is referred to, it is the nominal angle of the aerofoil in tunnel coordinates, rather than the measured value.

It would have been desirable to specify values of C_μ and Re directly, instead of varying a needle valve and a frequency controller, however this would have required on-line measurements, calculations, and feedback. The tunnel speed and and air supply would have to be coordinated. Doing this manually would slow the already lengthy process and introduce reading errors, since it would inevitably require fractional flow meter settings.

6.5 Data Collection

The maximum frame rate in this system is limited by the aforementioned laser and is 7.5 Hz. It was suggested that some low frequency variation in the flow might be detectable. For this the highest sampling rate possible would be required and losing synchronization (dropping frames) would be unacceptable. Due to memory limitations, data transfer rate, and bulk storage usage only 37 sequential image frames could be reliably acquired into one ensemble. The reason why one or two extra frame pairs could occasionally be gathered is unknown. For each combination of C_μ, α, and Re two ensembles of 37 image pairs were recorded. The entire experiment was replicated three times to determine repeatability. During the later PIV data analysis (Chapter 7) it was found that no useful time related information could be extracted from the data, so the above limitations were unnecessarily strict. In addition to the PIV image pairs, additional flow images were gathered with increased smoke levels for qualitative flow observations.

A key parameter in any PIV setup is the inter-frame time, since the shift in smoke particles between images is proportional to this time interval. Obviously the particle shift is also proportional to the speed of the flow, thus the time must be adjusted so that the particle displacement is not too large or too small. Based on approximate tunnel speed and qualitative evaluation of a number of test ensembles, the inter-frame times were set to 25 μs and 100 μs for the low and high tunnel speeds respectively.

Chapter 7

PIV Data Processing

The following chapter summarizes the methods used to process the raw images acquired and compute the lift coefficient and error at each momentum flux rate. First the cross-correlation that was performed on the digital images is outlined. The influence on the flow of the tunnel walls is then discussed. The method of calculating lift from the correlated images is detailed. The validity of pooling the data to create a master set is stated. Finally the equations for calculating the error in lift and momentum coefficients are given.

7.1 PIV Cross-correlation

The data were acquired with the Dantec FlowMap PIV system. During the data acquisition process a selection of images were cross-correlated on the acquisition computer to assure seeding and light levels were adequate. The main image processing and flow-map calculations however, were later done on a second computer using the more recent Dantec DynamicStudio software.

Before correlation the raw images were intensity balanced. The reason for this was to minimize the effect of varying light intensity across the light sheet. The intensity near the edges of the laser beam was found to vary slightly from pulse to pulse. As seen in Figure 7.1 the aerofoil casts shadows both above and below. So long as the intensity of an area is between the detection limit and saturation, good cross correlations can be achieved. The problem is found at the edges of light and dark areas where erroneous vectors in the direction of the edge are often computed. Thus the edges of the shadows in the image would likely result in four rows of vectors pointing up and down, while the remainder of the flow field would reflect the dominant left to right flow. The image balancing algorithm reduces, but does not eliminate this problem.

One way to prevent the shadow lines is to illuminate from one side at a time (Figure 7.2). For the second and third replicates of the experiment the aerofoil was illuminated from the top in the first 37 images and the bottom in the second 37

Figure 7.1: Example of raw flow-field image. Note light intensity is significantly higher than that used for data images. This was done for visualization purposes.

images. Using this method sacrifices the data in the shadow region, for improved data in the remaining flow field. Thus the pairs of ensembles in the second and third replicates must be used together to 'see' the entire field.

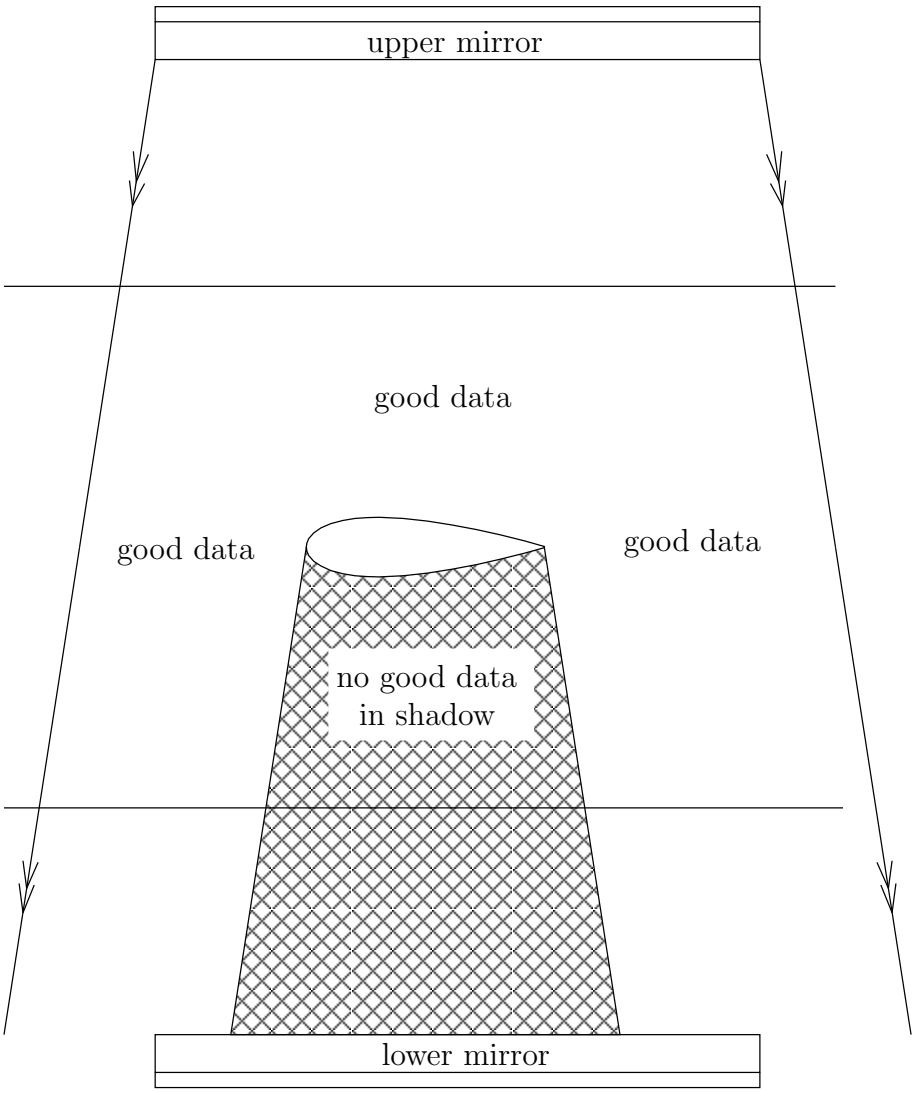

Figure 7.2: Schematic of single light sheet. Note shadow region that creates a 'hole' in the vector field.

The balanced images were then cross-correlated using an adaptive scheme. This scheme uses 64 by 64 pixel interrogation areas to determine the general flow field. The general field is then refined using 32 by 32 pixel interrogation areas. The adaptive scheme has a slight advantage in this case, since there are two distinct speeds. There is the speed of the wind tunnel and there is the speed of the jet. Since the inter-frame time was optimized for the tunnel speed, the use of larger interrogation areas results in more accurate correlations in the region of the jet. In

each case a 50% overlap in the interrogation areas was used.

Validation was done on the flow maps to ensure that only good data were recorded. The peak validation threshold was set so that the dominant correlation peak would be located rather than a noise peak. Peaks were accepted with pixel displacements between 2 and 5 pixels. The range of accepted stream-wise velocities were -20 to 60 m s^{-1}. The range of accepted cross-stream velocities were -25 to 25 m s^{-1}. A large range in accepted velocities was used to encompass all cases, including those with strong recirculation and high jet velocities. The range validation mainly functioned to remove spurious vectors, which were much larger than the range values and obviously erroneous.

Following the validation, statistics were computed on the ensembles of 37 flow fields using DynamicStudio and the data were exported. Figure 7.3 is an example of the average vector field exported from DynamicStudio. No replaced vectors were included in the exported data.

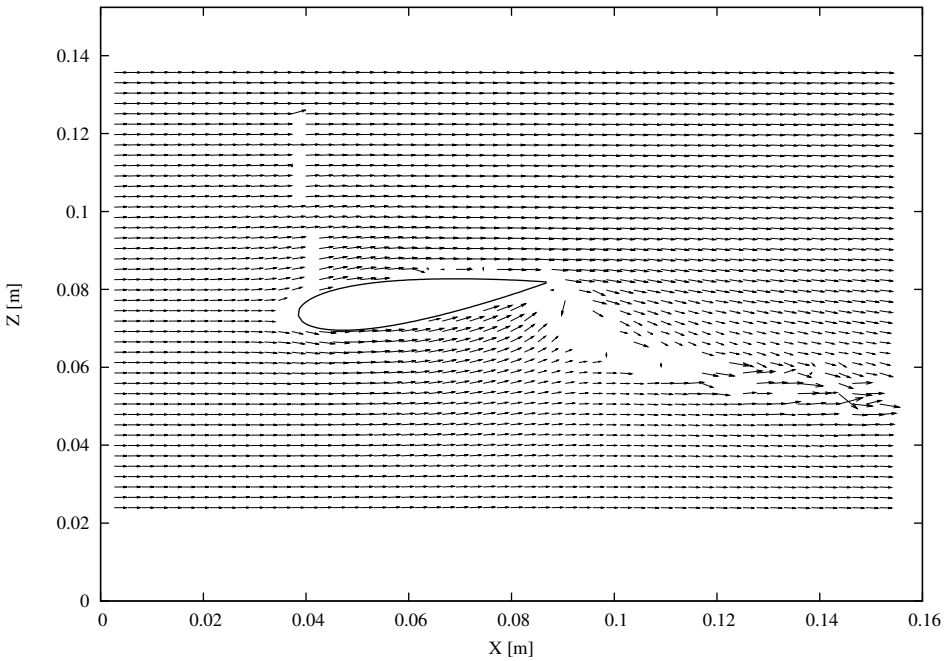

Figure 7.3: Example of 10° angle of attack at low speed with maximum jet flow rate. Note the 'shadow line' above the leading edge resulting from two sided illumination.

7.2 Correction of the Flow

When an aerofoil is placed in a wind tunnel, rather than an infinite body of air, the flow field is distorted by the presence of the impermeable walls. The classical wind-tunnel blockage corrections are described in depth in works such as "Low-Speed Wind Tunnel Testing" [20]. These corrections were not applied in this analysis, since the basic assumptions used to derive them are not correct in this case. Naturally the classical corrections do not account for the effect of the jet, which is a dominant factor in the tunnel flow.

The derivation of the corrections begins by considering two-dimensional potential flow around the aerofoil. In free air the streamlines away from the surface will be curved because of the aerofoil. In tunnel flow the upper and lower walls present a constraint on the flow in the vertical direction. Neglecting the tunnel wall boundary layer, the two walls effectively form straight streamlines at known locations. To model this effect analytically, fictitious mirror images (Figure 7.4) of the aerofoil are *placed* periodically above and below the real aerofoil extending to infinity. This causes straight streamlines to occur at the location of the walls in potential flow. The tunnel interference is the net effect of all of the images.

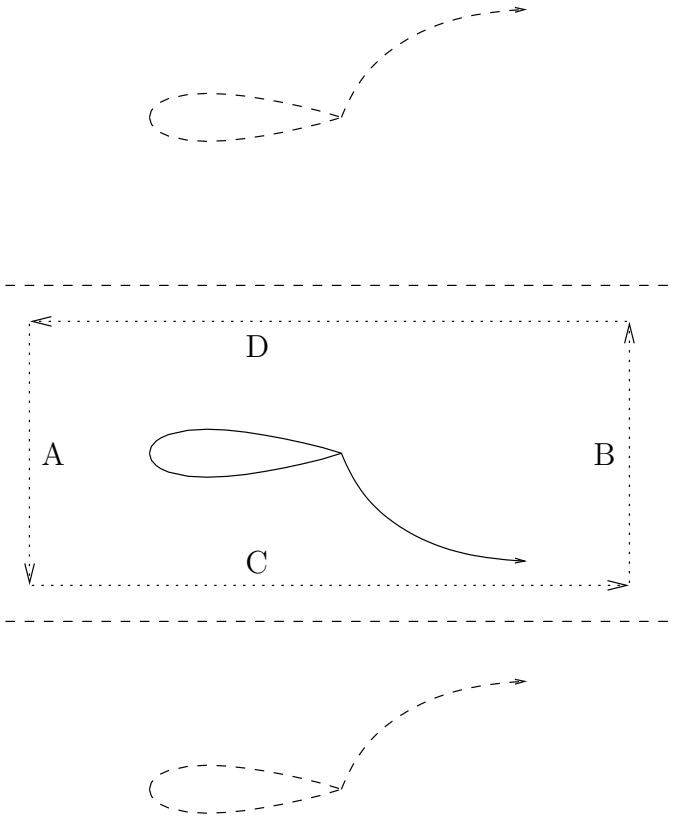

Figure 7.4: Aerofoil mirror images. Note path of circulation integral.

In potential flow the aerofoil is modelled by superimposing sources, sinks, and point vortexes in the flow. This creates the *effect* of the solid shape, lift, and the wake that is caused in real flow by viscous friction. The solid blockage effect of the aerofoil is modelled with one or more fluid sources and one or more fluid sinks arranged in the free stream. The lift of the aerofoil is modelled as either a single point vortex or a distribution of point vortexes. Viscous effects and the aerofoil wake is represented by a source at the location of the aerofoil and a sink far downstream. The fluid source-sink pair act to displace the free stream outward in the same manner as the lower momentum wake in viscous flow.

As detailed below in Section 7.3, the lift of the aerofoil is determined from the flow circulation, which in turn is calculated with a line integral enclosing the aerofoil and jet. The net effect of this method is that only sources of vorticity located within the line integral contribute to the circulation; the 'image' vortex sources being outside of the line. So long as the integration path encloses the aerofoil and jet, but excludes the wall boundary layers, the calculated lift will be unaffected by the presence of the walls. Interestingly this means that more than one integration path will yield the same result within the precision of the method.

7.3 Lift and Drag Calculation

The circulation is computed on a path over the flow field (Figure 7.4). Due to multiple factors the entire 62 by 62 vector field was not used. One reason was that the upper and lower walls are visible in the raw images (Figure 7.1) and obviously there are no valid vectors outside of the test section. The other factor is light sheet variability at the edges. The left and right of the usable area are A and B respectively. The bottom and top of the area are defined by C and D respectively. Note the flow field origin is in the lower left corner.

By the Kutta-Joukowski theorem the aerofoil lift coefficient is: $C_l = \frac{2\Gamma}{U_\infty c}$ [28]. In Cartesian coordinates the circulation about path P is simply $\Gamma = \oint_P (u \cdot dX + v \cdot dZ)$ [24] for two dimensional flow in the (X,Z) plane. Note the importance of encircling all vorticity generated by the aerofoil within the path P. Vorticity generation outside results in a bias in Γ, thus the importance of placing line segment B *sufficiently* far downstream (ideally at $X = \infty$). For a rectangular path on a uniform grid with spacing Δ the equation is approximated by four sums:

$$\Gamma \approx \Delta \cdot \sum_{i=A}^{B} u(i, C) + \Delta \cdot \sum_{j=C}^{D} v(B, j) + \Delta \cdot \sum_{i=B}^{A} u(i, D) + \Delta \cdot \sum_{j=D}^{C} v(A, j) \qquad (7.1)$$

The function was tested with a simulated uniform flow field at arbitrary angle, and with a simulated free vortex of strength Γ over varying paths. In each test the

error on the calculated circulation was much less than 1% and therefore well within experimental error. The error is most likely due to discretisation of the velocity.

If the flow is attached, two dimensional, and a sufficiently large field of view is used then it may be possible to apply a one dimensional momentum balance to upstream and downstream cross-sections and estimate the drag of the aerofoil. In many cases during this study the flow was not attached. 25% of the flow cases were deeply stalled and a further 12.5% of the cases were at best marginal. With significant linear momentum converted to angular momentum in the recirculating wake, calculating drag by a wake survey is not valid. If it were not necessary to average the flow data, then it would be possible to account for the instantaneous angular momentum of the wake. The average angular momentum of the recirculating region is small, however the instantaneous value is not. Nevertheless qualitative results can be obtained from examinations of the wake profiles as they change with the independent variables.

7.4 Error Propagation

Due to the 50% overlap in the interrogation areas one can not say that a vector and its neighbours are independent. The variance propagated through the circulation integral is calculated with Equation 7.2 following the method presented by Bevington [31].

$$\sigma_\Gamma^2 = \Delta^2 \left[\sigma_N^2 + 2(\sigma_N)(\sigma_1)\rho_{N,1} + \sum_{i=1}^{N-1} \sigma_i^2 + 2(\sigma_i)(\sigma_{i+1})\rho_{i,i+1} \right] + \left[\frac{\Gamma \cdot \epsilon_\Delta}{\Delta} \right]^2 \qquad (7.2)$$

The standard deviation of the i^{th} velocity (σ_i) and the length scale (Δ) are read directly from the exported data files. The error on the length scale (ϵ_Δ) is approximately $\pm 0.2\%$ of Δ based on a estimated combined error of ± 1.5 pixel in the length scale calibration process.

The problem remains how strongly correlated a given point i is with its neighbours $i-1$ and $i+1$? To determine this along the integration path of each flow field would be a lengthy process. For the purpose of this work it was assumed that each grid point and its two neighbours were perfectly correlated. This results in a slight overestimation in the error. It should be conservative to assume that the results are less reliable, so long as conclusions are not based heavily on the limits of the range.

Similarly the error in the free-stream velocity, which has been defined as the average of the inlet cross-section, is calculated by Equation 7.3 with the same assumption of perfectly correlated neighbours.

$$\sigma_{U_\infty}^2 = \frac{1}{N^2}\left[\sigma_N^2 + \sum_{i=1}^{N-1}\sigma_i^2 + 2\left(\sigma_i\right)\left(\sigma_{i+1}\right)\rho_{i,i+1}\right] \tag{7.3}$$

Based on the previously stated lift coefficient ($C_l = \frac{2\Gamma}{U_\infty c}$) and Equations 7.2 and 7.3 an expression for the variance of the lift coefficient was derived (7.4). In this expression the effect of the third term depends on whether the circulation is positive or negative. If the circulation is positive the error in the lift is reduced by assuming a positive correlation between the free-stream velocity and the circulation. Alternatively if the circulation is negative, all else being equal, the third term increases the calculated error. Again the error was overestimated by calculating using extreme values of correlation coefficient ($\rho_{\Gamma,U_\infty} = \pm 1$) and recording whichever is larger.

$$\left(\frac{\sigma_{C_l}}{C_l}\right)^2 = \left(\frac{\sigma_\Gamma}{\Gamma}\right)^2 + \left(\frac{\sigma_{U_\infty}}{U_\infty}\right)^2 - 2\left(\frac{\sigma_\Gamma}{\Gamma}\right)\left(\frac{\sigma_{U_\infty}}{U_\infty}\right)\rho_{\Gamma,U_\infty} \tag{7.4}$$

Combining the equations for the momentum coefficient (3.3, 3.4) results in Equation 7.5. Using the same methods the expression for the error propagated through to the momentum coefficient can be derived as in Equation 7.6.

$$C_\mu = \left(\frac{2}{\rho_\infty \cdot c \cdot s}\right)\sqrt{\frac{k\cdot(p_f)_{des}}{R\cdot(T_f)_{des}}}\left[\frac{\sqrt{p_f}\cdot(q_V)_{des}\cdot Ma}{U_\infty^2}\right] \tag{7.5}$$

$$\left(\frac{\epsilon_{C_\mu}}{C_\mu}\right)^2 = \left(\frac{\epsilon_{(q_V)_{des}}}{(q_V)_{des}}\right)^2 + 4\left(\frac{\sigma_{U_\infty}}{U_\infty}\right)^2 + \left(\frac{\epsilon_{Ma}}{Ma}\right)^2 + \frac{1}{4}\left(\frac{\epsilon_{p_f}}{p_f}\right)^2 + 2\left(\frac{\epsilon_{Ma}}{Ma}\right)\left(\frac{\epsilon_{p_f}}{p_f}\right)\rho_{Ma,p_f} \tag{7.6}$$

Stated accuracy of the rotameter is $\pm 5\%$ full scale which is about $\pm 1.2 \times 10^{-4}$ m^3 s^{-1}. The accuracy of the pressure gauge is unknown. The manufacturer of the pressure gauge makes industrial gauges with $\pm 1.6\%$ full scale accuracy, which is just under one half of the smallest division, but since no calibration information is available the assumed accuracy is $\pm 5\%$ of full scale. The reading error on setting the flow rate results in a $\pm 4\%$ of value error on the pressure. Also there is a $\pm 1.7\%$ slow fluctuation in the supply pressure. Thus the accuracy of the pressure is $\pm 1.4 \times 10^4$ Pa or better.

Chapter 8

PIV Data Pooling

For each combination of tunnel speed, angle of attack, and jet flow rate two ensembles of 37 images were stored. Six to eight ensembles were initially recorded and checked as previously noted, however only the best two were kept. This was repeated three times, over a period of days, to assess repeatability. Thus for each flow state there are six ensembles totalling 222 images, which in theory, could be combined to result in a master flow field or lift coefficient. Refer to Tables 8.1 and 8.2 for a summary of the stored cases.

Table 8.1: Summary of PIV cases tested.

Parameter	#	Values
Chordal Reynolds number	2	0.038×10^6 and 0.120×10^6
Angles	4	0°, 5°, 10°, and 15°
Flow rates	11	
Total cases	88	

Table 8.2: Summary of data stored from PIV experiment.

Image pairs per ensemble	37
Ensembles per case	2
Replicates per case	3
Total image pairs per case	222

Due to the rate of data acquisition (7.5 Hz) it is reasonable to assume that each image in an ensemble is acquired under the same flow conditions, and is not subject to long term variation or differences in the setup. For this reason the average flow field was exported from DynamicStudio rather than all 37 individual flow fields. The two important questions are: how do the six ensemble-averaged flow fields compare and are they consistent?

The lift coefficient versus jet momentum curves for the first and second ensembles acquired can be compared. As mentioned previously the third ensemble cannot stand alone from the fourth and likewise the fifth from the sixth. This is a result of the 'hole' in the flow map (Figure 7.2) either above or below the aerofoil due to the shadow.

To compare the first and second ensembles the lift was computed for each set and averaged. The result is plotted versus C_μ in Figures 8.1(a) and (b). Error bars are used to show the discrepancy between the two results. Clearly there are differences between the two ensembles at multiple points, however it is also clear that the two data sets are comparable in both trend and magnitude. Thus the statistics of the ensembles can be pooled within a replicate.

The statistics of each ensemble pair were pooled to create a master set for the given replicate. The lift and momentum flux were then recalculated resulting in Figures 8.2(a) through 8.6(b). In the 0° and 15° cases (Figures 8.2(a) and (b), 8.6(a) and (b)), at both high and low Reynolds number, the trend is approximately linear. Clearly each of the three replicates, in these four cases, follows the same general trend. Although the three replicates do not all fall on the same curve, Figure 8.2(b) in particular, the data can still be pooled.

Refer to Figures 8.3(a) and 8.4(a) for the 5° and 10° low Reynolds number cases respectively. Though the two curves are different there is consistency between the data of the three replicates. This is with exception to the region about $C_\mu = 0$ in the 5° case where replicate three diverges. Qualitatively it appears that the third replicate is shifted in the negative C_μ direction.

In the 5° high Re case, and to a lesser extent the 0° high Re case, the three replicates are similar in slope, but appear to be offset in the lift direction by a constant. Alternatively the curves could be thought of as shifted in the momentum direction, since changing the y- or x-intercept of a straight line has the same effect. One possible reason for this difference is the relatively crude apparatus for setting the angle of attack. The angle of attack was measured, in tunnel coordinates, from the raw images. The true angle for each ensemble is presented in Tables B.1 and B.2. The lift offset in the 5° high Re case follows the expected trend with α (Table B.2) and the 0° high Re case also does over a limited range. It is interesting to note that with decreasing measured α the previously mentioned low Re curves at nominal 5° shift in the negative C_μ direction. Overall there is a trend in lift values with angle of attack between the replicates, however it cannot be concluded that this is the only factor responsible for the variation between the replicates. Nevertheless it is still reasonable to conclude that the data of the three replicates at 5°, in high and low speed flow, are comparable.

The 10° high Reynolds number results are problematic. In the first replicate the C_l begins at 0.98 and decreases smoothly with increasing C_μ as expected. The second and third replicates do not follow this trend. The second and third replicate begin at 0.64 and 0.87 respectively then drop sharply to approximately 0.1 at low momentum flux. The lift coefficient of these two curves behave erratically until they

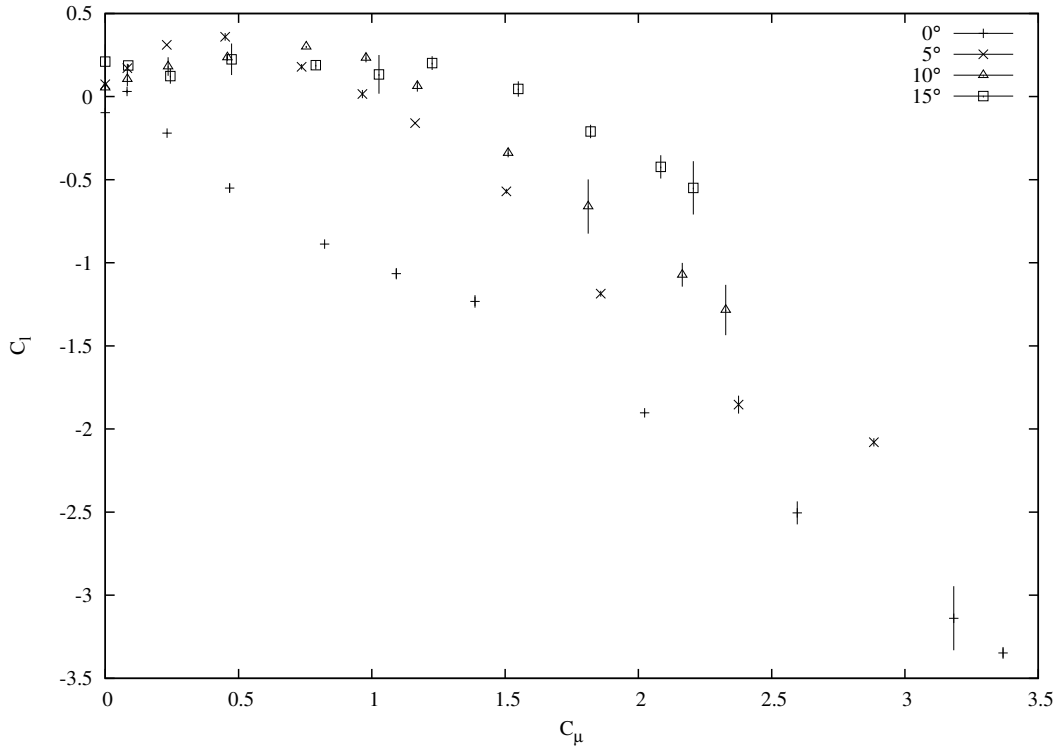

(a) Lift-jet momentum at $\mathrm{Re} = 0.038 \times 10^6$.

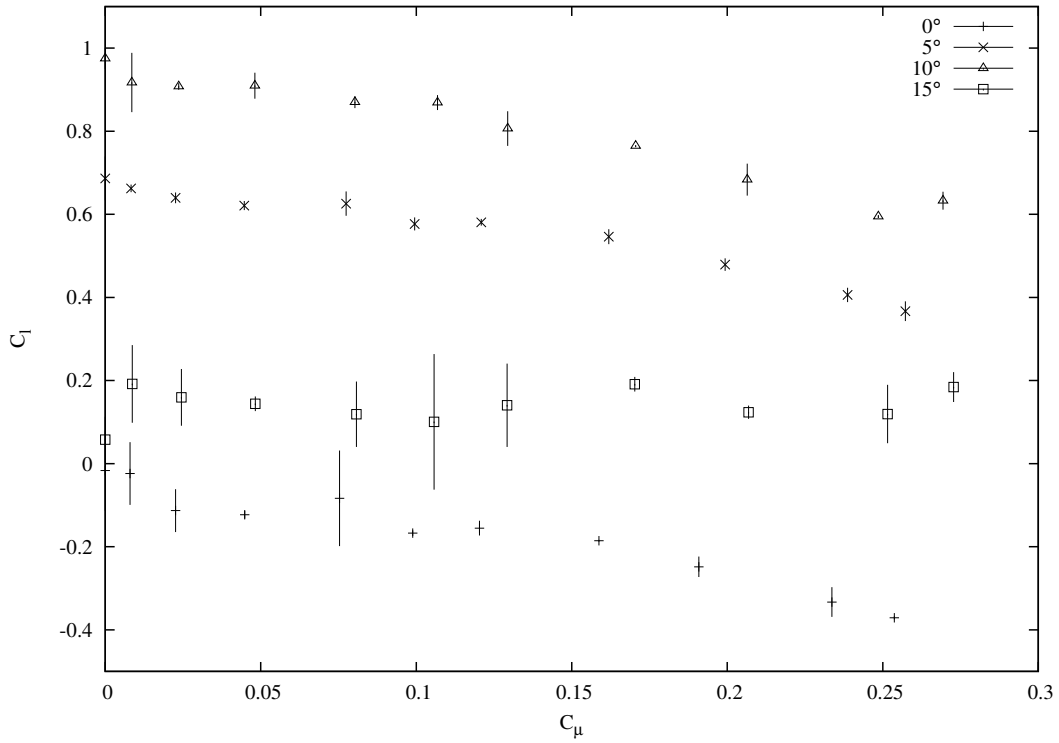

(b) Lift-jet momentum at $\mathrm{Re} = 0.120 \times 10^6$.

Figure 8.1: Mean lift computed from first and second ensemble. Note error bars indicating discrepancy between the individual ensembles and their mean.

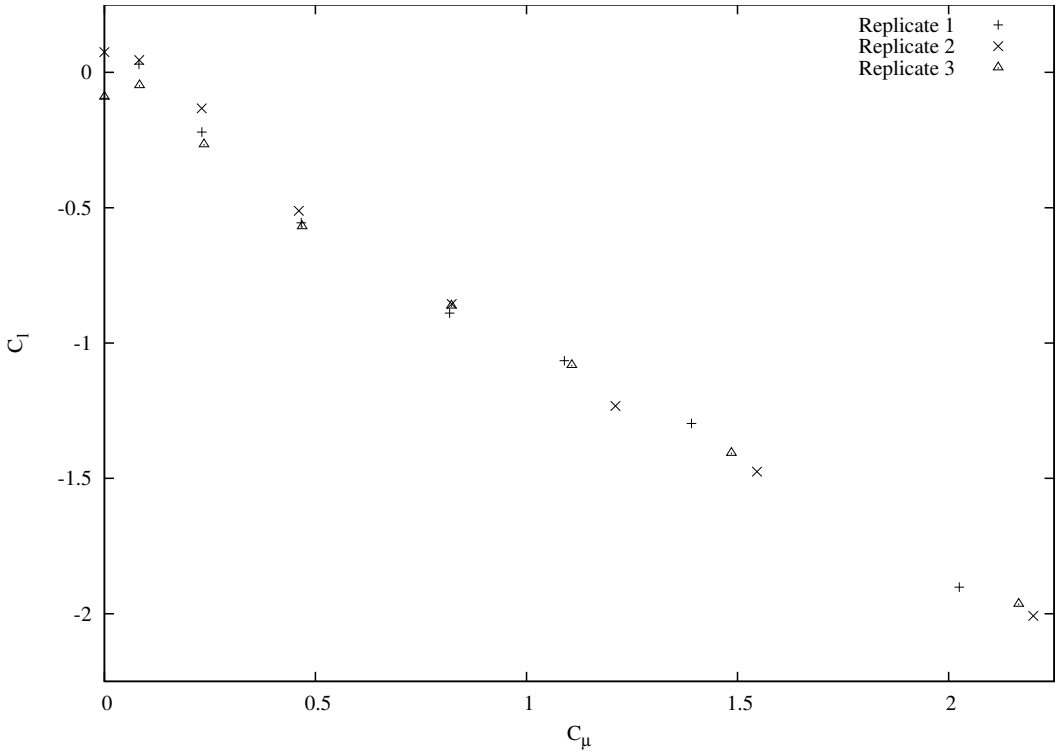

(a) $\mathrm{Re} = 0.038 \times 10^6$

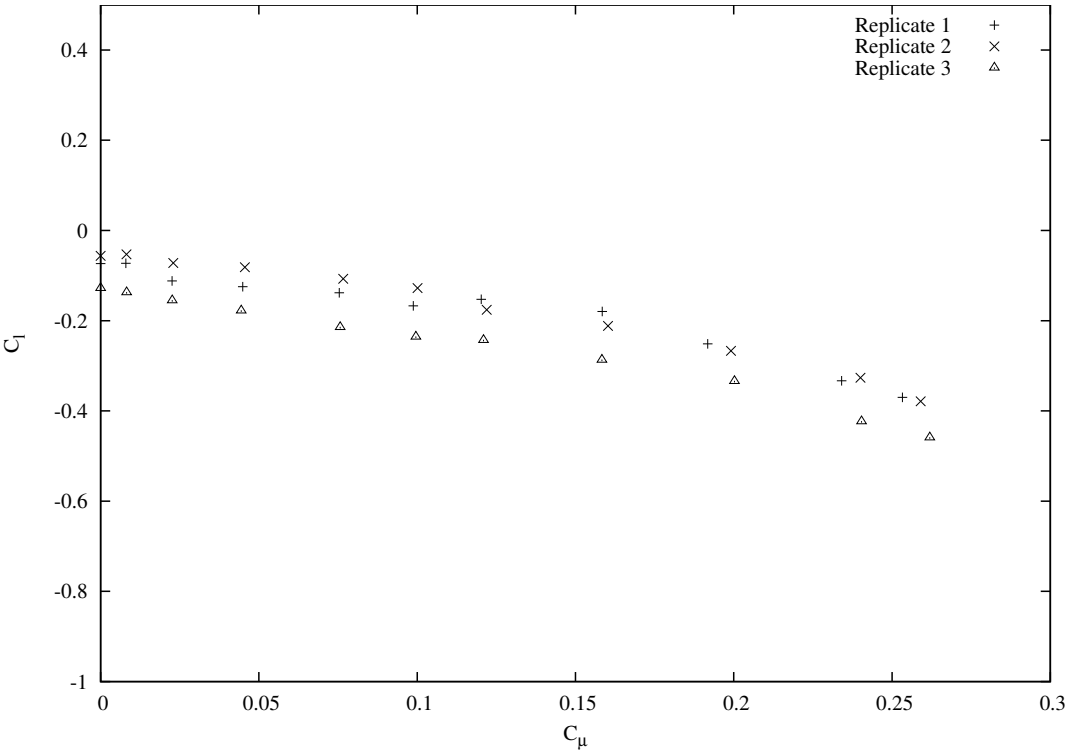

(b) $\mathrm{Re} = 0.120 \times 10^6$

Figure 8.2: Pooled ensemble pairs at $\alpha = 0°$.

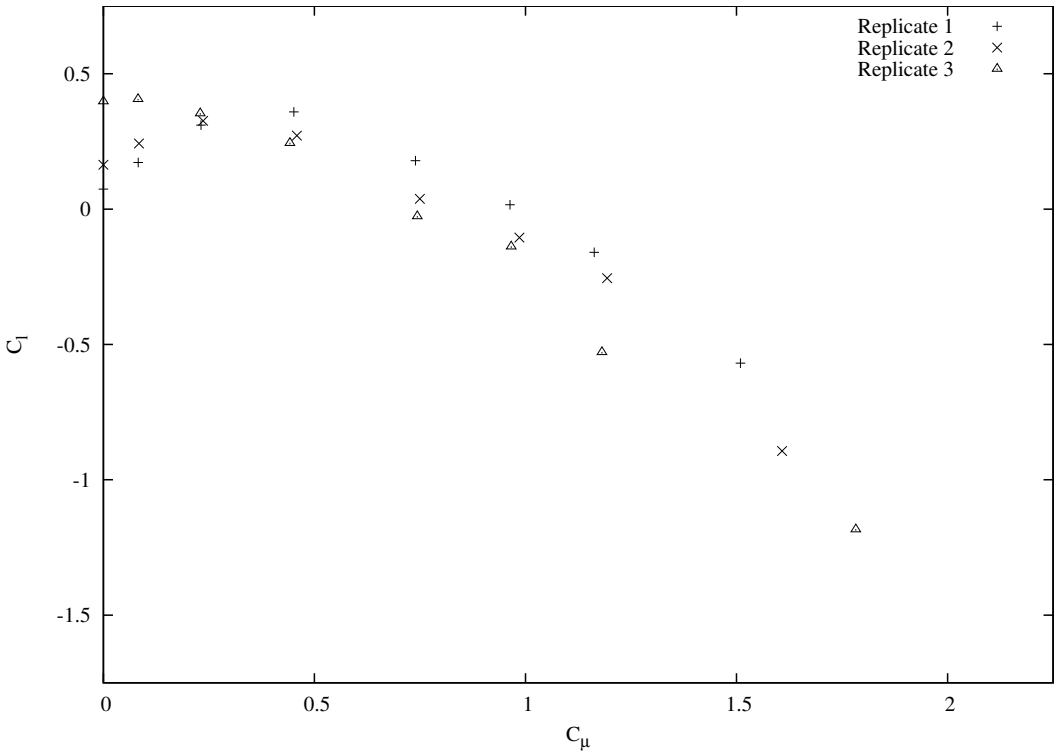

(a) $\mathrm{Re} = 0.038 \times 10^6$

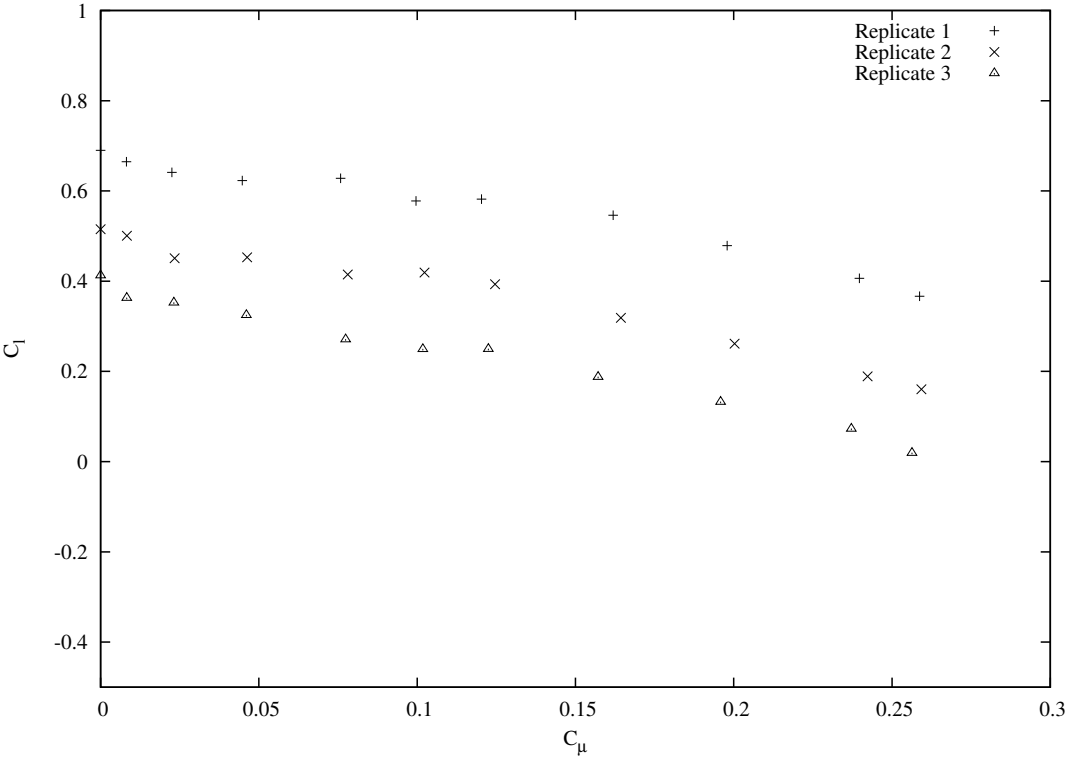

(b) $\mathrm{Re} = 0.120 \times 10^6$

Figure 8.3: Pooled ensemble pairs at $\alpha = 5°$.

recover to the level of the smooth curve. The third curve recovers at $C_\mu = 0.11$ to $C_l = 0.95$. The second curve recovers later at $C_\mu = 0.16$ to $C_l = 0.86$. It is interesting to note from Table B.2 that the first replicate has the lowest measured angle of attack followed by the third and the second replicates in that order. This response looks suspiciously like abrupt stall behaviour and suggests that the three replicates in this case are not in fact comparable. Further evidence is provided by Figures 8.5(a) and (b), which show recirculation behind the aerofoil in the second replicate. One hypothesis for this behaviour is that the application of low jet momentum has a destabilizing effect on the flow actually causing it to separate if the angle of attack is above a certain limit. A further hypothesis is that with a sufficiently high momentum flux the flow will either remain attached or reattach. To confirm this behaviour the wake profile can be examined with increasing jet flow rate as shown in Figures 8.7, 8.8, and 8.9.

Figure 8.7 clearly shows a narrow wake that changes little with increasing jet flow rate. Figure 8.8 however shows a wake that varies irregularly in both width and position with increasing jet flow before returning to a tightly confined wake at the last four flow rates ($C_\mu \geq 0.16$). Figure 8.9 is perhaps the clearest example of the effect of momentum addition in this case. Initially the wake is narrow. The wake immediately widens when a small jet flow is applied. As jet flow increases the wake narrows and at high momentum ($C_\mu = 0.11$) the wake profile becomes S-shaped showing the decrease in velocity due to viscous effects and the increase in velocity due to jet momentum addition.

It can be said therefore, that the interpretation of the lift data is correct and that under the right circumstances the jet can cause attached flow to separate just as it can cause separated flow to reattach. The conclusion drawn is that to avoid abrupt, and possibly dangerous, stall behaviour there is a minimum jet momentum that should be applied when operating in marginal conditions.

Clearly it is worth being cautious about pooling the data, since in the 10° high Reynolds number case this would result in misleading interpretations. With exception to the 10° high speed case the statistics of the three replicates of the experiment were pooled for each flow rate and angle of attack. For the high Reynolds number 10° case the flow fields corresponding to the outliers in Figure 8.4(b) were discarded before calculating the new average flow field for each flow rate. The C_l versus C_μ curves were subsequently recalculated for each case.

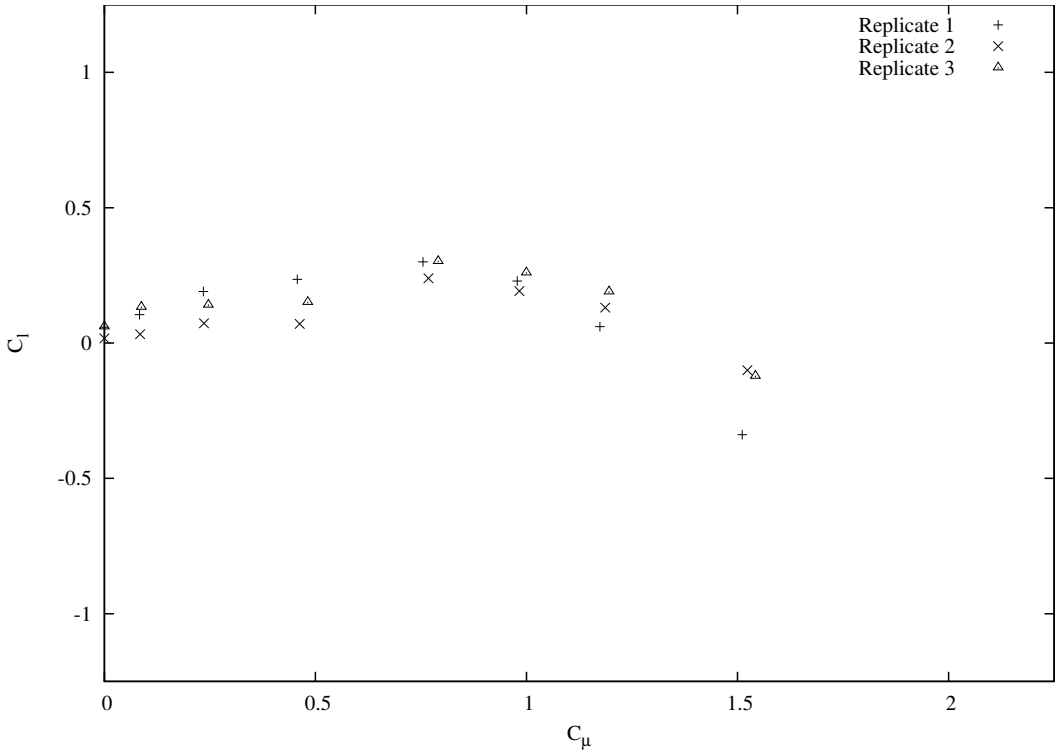

(a) $\mathrm{Re} = 0.038 \times 10^6$

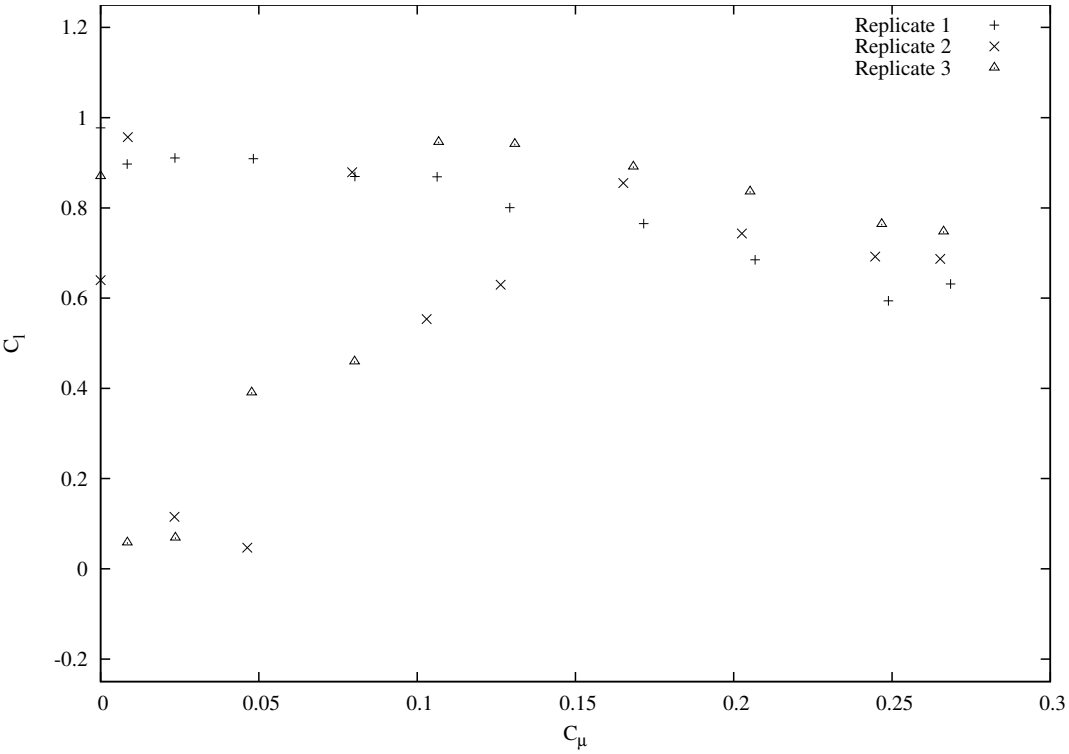

(b) $\mathrm{Re} = 0.120 \times 10^6$

Figure 8.4: Pooled ensemble pairs at $\alpha = 10°$.

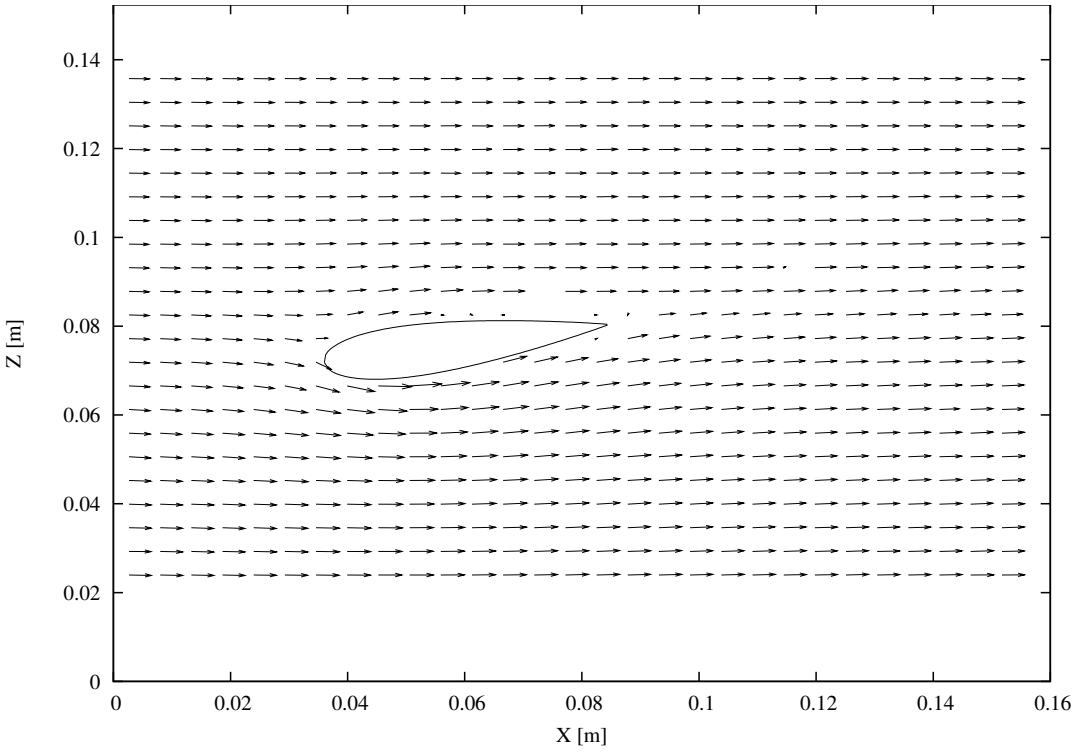

(a) Replicate 1

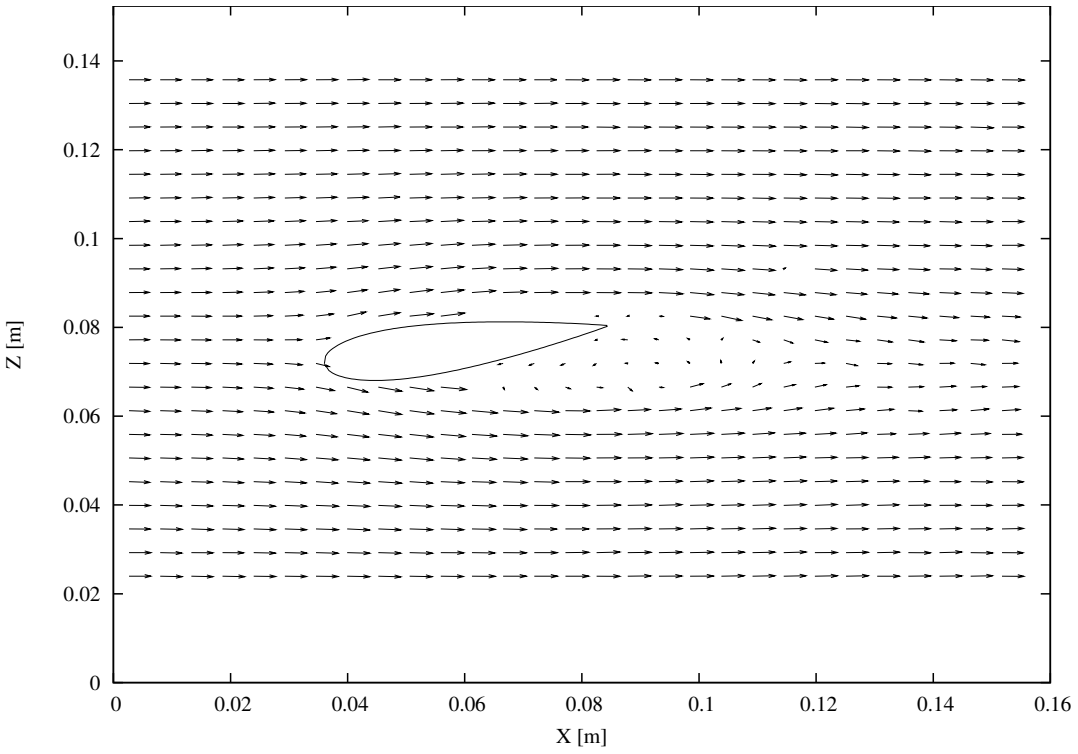

(b) Replicate 2

Figure 8.5: Notice recirculating flow in replicate 2 is not seen in replicate 1. Nominal $\alpha = 10°$, $C_\mu = 0.02$, Re $= 0.120 \times 10^6$. Replicate 3 (not shown) similarly shows recirculation.

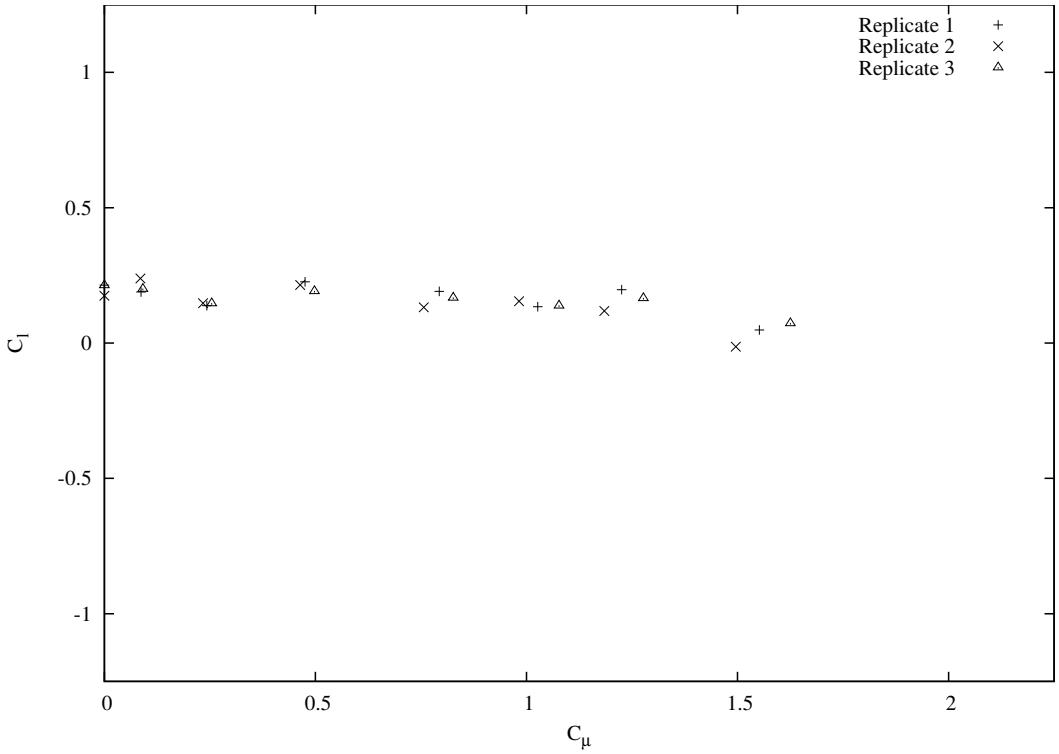

(a) $\mathrm{Re} = 0.038 \times 10^6$

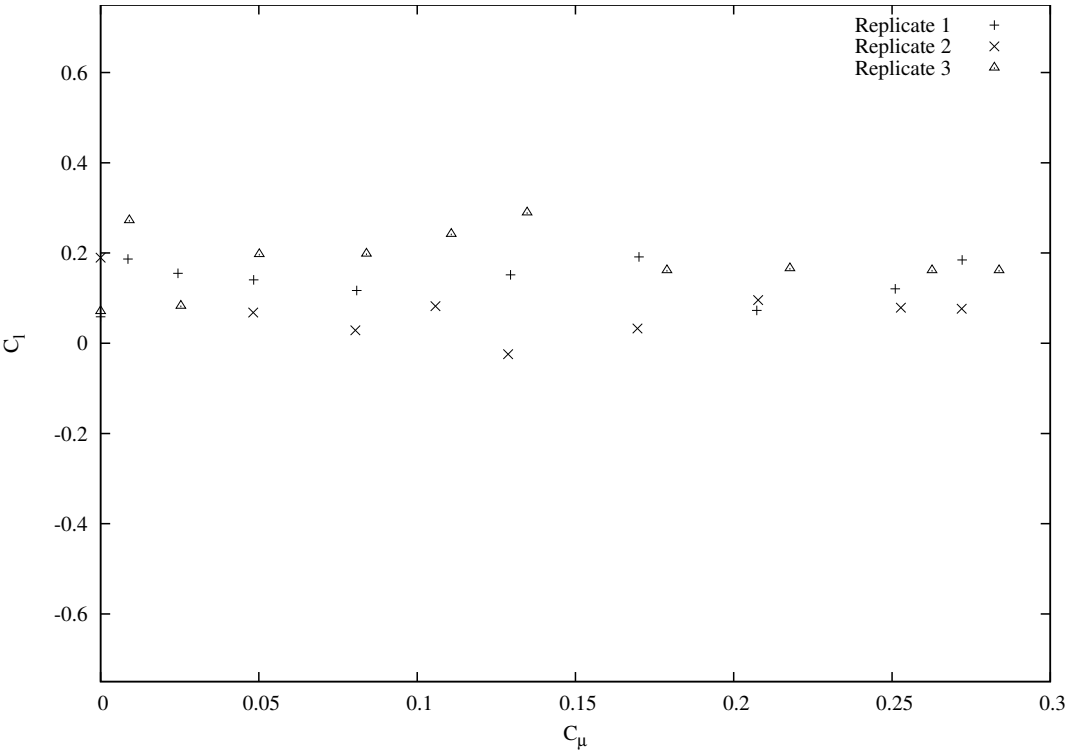

(b) $\mathrm{Re} = 0.120 \times 10^6$

Figure 8.6: Pooled ensemble pairs at $\alpha = 15°$.

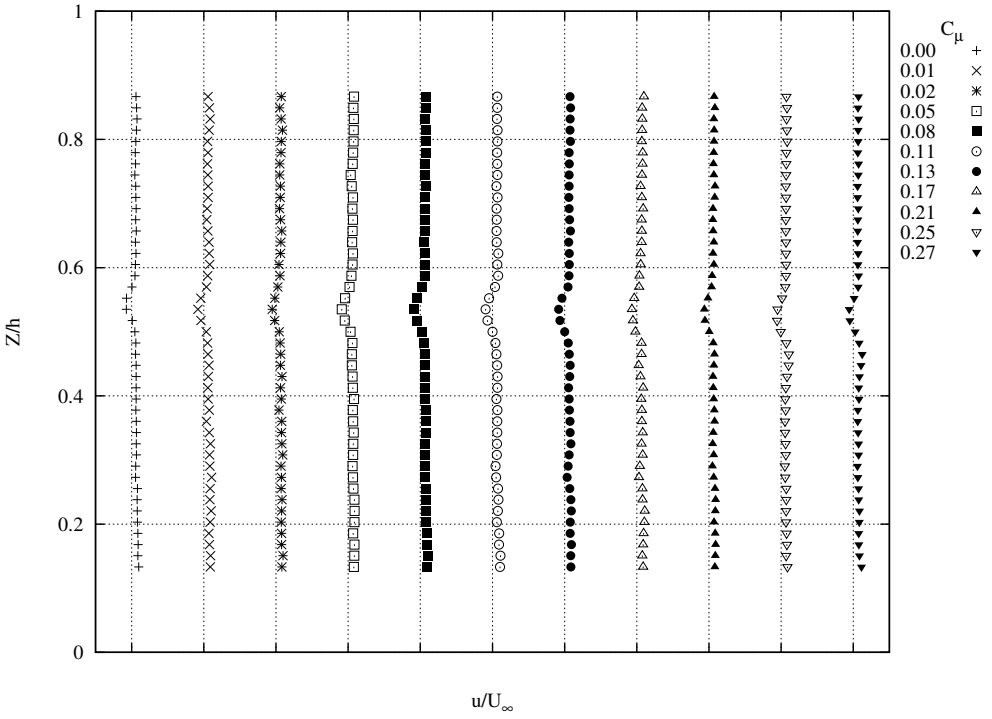

Figure 8.7: Wake profiles with increasing C_μ at 10° and Re $= 0.120 \times 10^6$ (replicate 1). Note also curves have been offset for clarity; vertical grid-lines indicate $\frac{u}{U_\infty} = 1$.

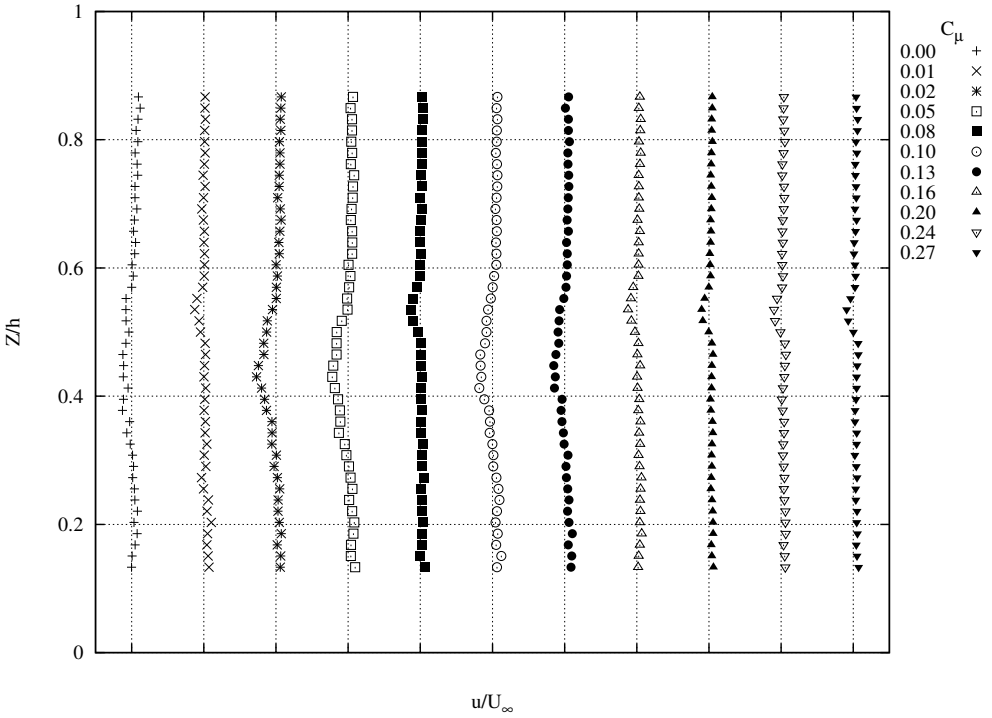

Figure 8.8: Wake profiles with increasing C_μ at 10° and Re $= 0.120 \times 10^6$ (replicate 2). Note also curves have been offset for clarity; vertical grid-lines indicate $\frac{u}{U_\infty} = 1$.

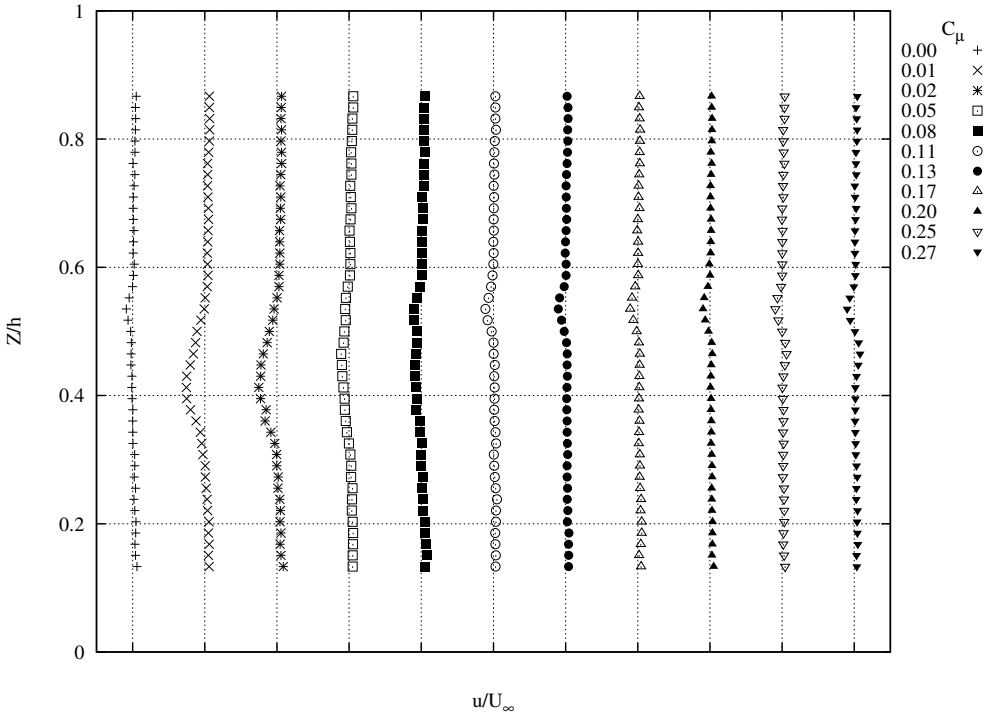

Figure 8.9: Wake profiles with increasing C_μ at 10° and $\mathrm{Re} = 0.120 \times 10^6$ (replicate 3). Note also curves have been offset for clarity; vertical grid-lines indicate $\frac{u}{U_\infty} = 1$.

Chapter 9

Lift Control Results

The pooled results of the data processing are presented in the following sections. Low and high Reynolds number results are given with a general discussion of the trends. The results are further compared with two prior works to check validity and understand the current trends. From this, an interpretation of the flow behaviour is drawn.

9.1 Low Speed Results

The low Reynolds number lift results from the current experiment are presented below in Figure 9.1. As expected the lift coefficient decreases with increasing momentum flux. One clear trend is the shift of the lift curves towards higher momentum flux with increasing angle of attack. This means that in general, the use of jet flow to reduce the lift becomes less effective with increasing angle of attack. In deep stall a large C_μ is required to affect significant control. Such levels may not be practical or economical. With the exception of stall controlled machines this operational envelope is avoided anyway, so this may be inconsequential.

Notice in the figure that the highest four flow rates, at each angle of attack, follow the same trend as the preceding points. This provides incidental support for the interpretation given in Chapter 5 that the loss in jet momentum occurs downstream of the nozzle and is related to the nozzle pressure ratio. If the momentum coefficient at the orifice were to approach a constant, then the lift coefficient should also approach a constant. C_l clearly continues to increase in magnitude however, and there is no evidence to suggest that there *should* be a discontinuity at this particular location.

9.2 High Speed Results

The pooled high Reynolds number results are presented in Figure 9.2. As expected increased α results in increased C_l, and increased C_μ results in decreased C_l. At 15°

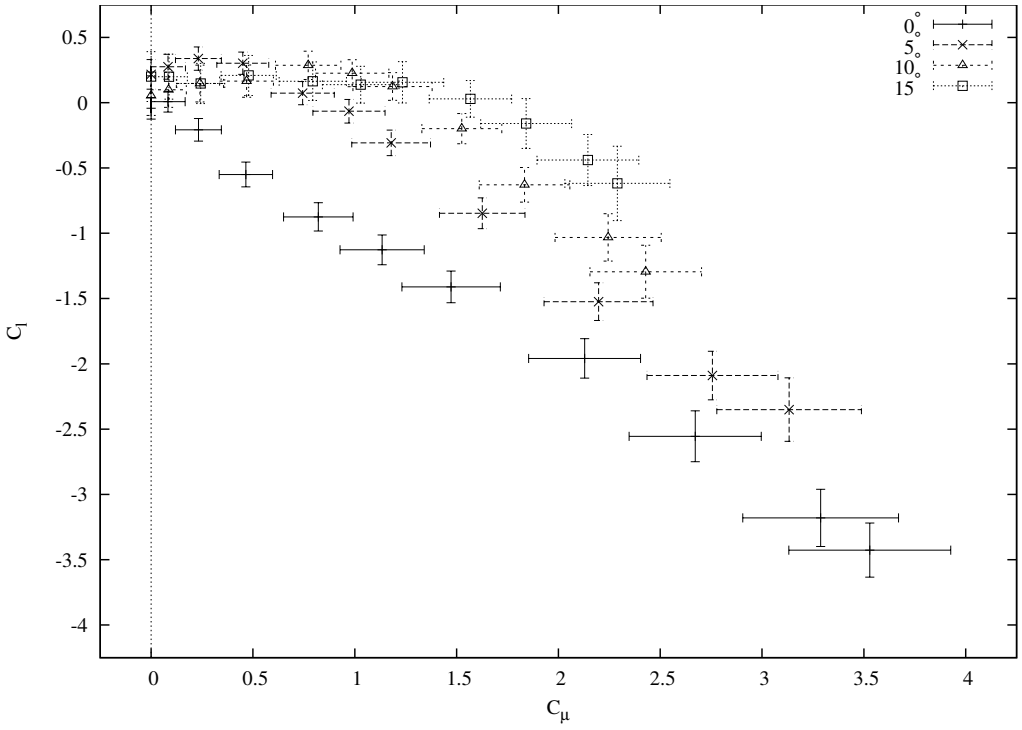

Figure 9.1: Pooled C_l versus C_μ curves at low Re.

the aerofoil is clearly stalled, thus it no longer follows either of the aforementioned trends. Qualitatively the lift response with momentum flux is nearly linear with a slope on the order of one. A slightly concave downward trend is visible in Figure 9.2.

The definition of the momentum coefficient (Equation 2.1) shows how it is increasingly difficult to affect control as the free-stream velocity increases. In the 'high speed' condition, which is still relatively low Re, the range of C_μ achievable is relatively small. Since $C_\mu = f(U_\infty^{-2})$ and $\mathrm{Re} = f(U_\infty)$, C_μ decreases faster than Re increases with increasing U_∞. This means that for a given Re, C_μ is increased by decreasing U_∞ and increasing the chord. In other words, if all else is equal, larger aerofoils should have larger ΔC_l.

It must be borne in mind that under the test conditions the 10° (nominal) experiment showed a very abrupt stall response, which is likely related to the low momentum boundary layer. The pooled results shown in Figure 9.2 represent the pre-stall response, however at slightly higher angle of attack the response would be more similar to the 15° curve. It is therefore important to exercise caution if operation near stall is required; particularly if operating at low Reynolds number.

9.3 Comparison with Prior Work

Though the lift results calculated by the circulation integral are order-of-magnitude correct, it is worth comparing them to published data. Unfortunately much of the

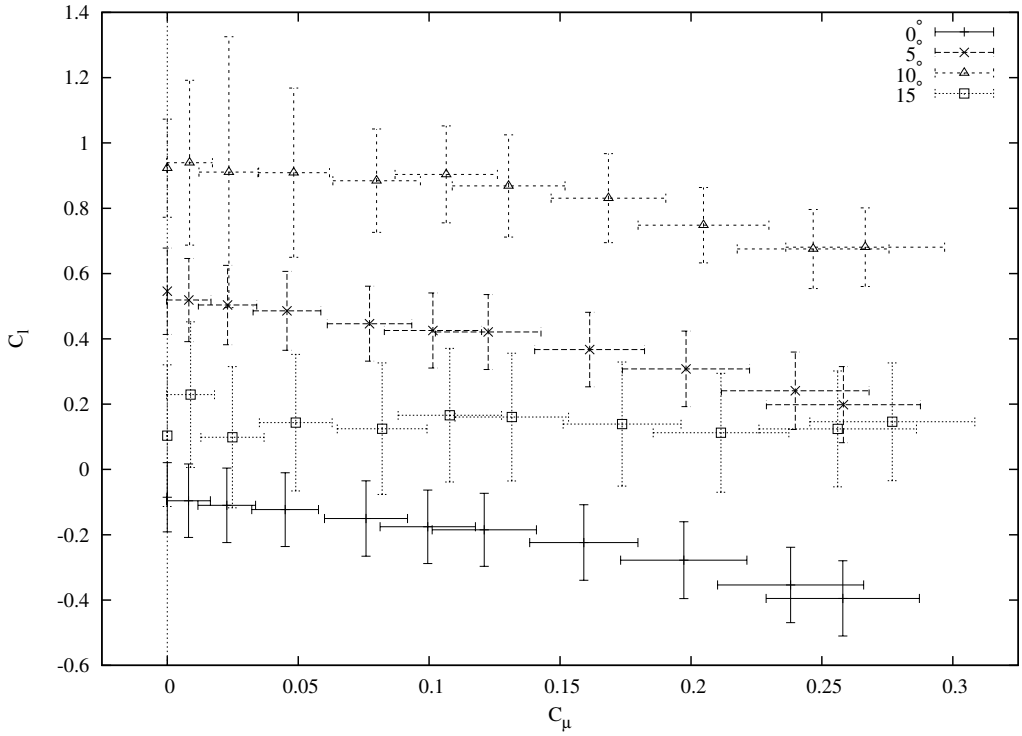

Figure 9.2: Pooled C_l versus C_μ curves at high Re.

lift data published to date have been gathered at much higher Reynolds numbers. High Reynolds number lift data are not generally applicable to low Reynolds number applications.

There are two obvious comparisons that can be made between prior work and the current experiment. First the magnitude of C_l can be compared with classic wind-tunnel work if $C_\mu = 0$. The C_l can be compared as α and Re are varied. Secondly C_l can be compared with previous jet flapped aerofoil results if $\alpha = 0$. If the 'natural' circulation of the aerofoil ($2\pi\alpha\eta$) is zero (Section 2.2.1), then the response of the jet flap should be isolated. Thus the only difference between the elliptical aerofoil used by Dimmock [6] and the chosen NACA symmetric aerofoil is the effect of the profile on the pressure component of lift.

9.3.1 Zero Momentum Flux Data

One data set used for comparison in this study was from Sheldahl and Klimas at Sandia National Laboratories [32]. The data were originally intended as an input for wind turbine design. This data set was produced by combining in-house experimental data with synthesized data from a computer code. This was the only data set found in the correct Reynolds number range for the NACA 0025 aerofoil. It was tabulated by Reynolds number and angle of attack. Figure 9.3 shows the comparison between the relatively sparse jet-off experimental data and

the comparison data. Note the experimental lift was plotted against true angle of attack (Tables B.1 and B.2) rather than nominal. For example the nominally 0° data are actually plotted at −0.7° on the graph.

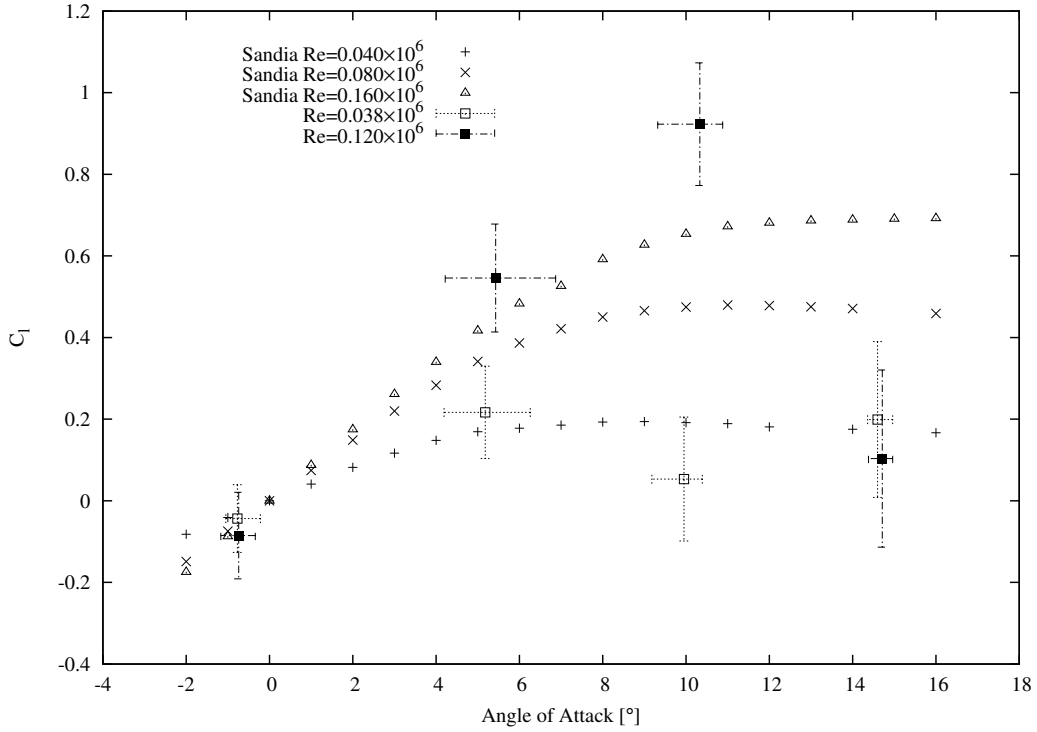

Figure 9.3: Lift curves for NACA 0025 aerofoil at three different Reynolds Numbers [32] compared to the $C_\mu = 0$ results from current experiment

It is seen that the data from the current experiment are somewhat consistent with the comparison data set. At nominally 0° and 5° the current experiment is consistent with the Sandia data. At the higher Re condition the current experiment shows the initial lift slope continuing to 10° before abruptly dropping to approximately zero. The Sandia data, at similar Reynolds numbers, exhibit a much more gentle stall behaviour and significantly lower maximum lift. At the low Re condition the aerofoil in the current experiment appears to stall earlier somewhere between 5° and 10°. Thus in attached flow the two sets of results are consistent, however the stall behaviour is very different. It is not known what factor or factors are responsible for the discrepancies in lift and stall behaviour.

9.3.2 Zero Angle of Attack Data

For a symmetrical aerofoil section the nomenclature of 'pressure side' and 'suction side' of the aerofoil can be interchanged. Thus the case of ($\alpha \geq 0$, $\theta \leq 0$) and ($\alpha \leq 0$, $\theta \geq 0$) are equivalent.

The data set used for zero angle of attack comparison was from Dimmock's experiments [6] detailed in Chapter 2. Figure 9.4 shows the current experimental

data, at high and low Reynolds number, compared with the predicted reaction lift (Equation 2.4). Compare the current experiment to Dimmock's data at $\theta = 31.4°$ and 90.0°. Note total lift curves (Equation 2.4) also plotted over Dimmock's data.

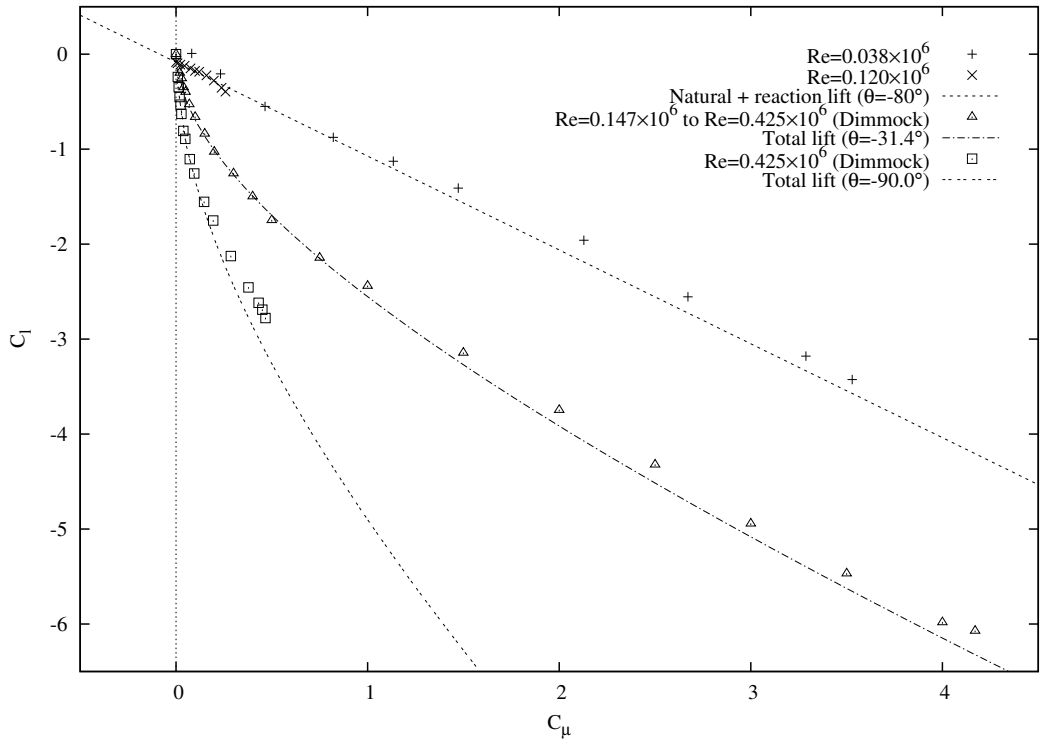

Figure 9.4: Comparison between current experimental data, published data [6], and the predictions of Equation 2.4. Note the sign convention of published data was interchanged.

Immediately obvious is that the lift coefficient in the current experiment is much smaller in magnitude, for a given momentum flux, than the previous results. Since the current experiment uses a jet deflection angle of 80°, the lift coefficients should fall somewhere between Dimmock's results for $\theta = 31.4°$ and $\theta = 90.0°$. Though a slight overestimate, Equation 2.4 fits the data reasonably well. The equation is within 5% at $\theta = 31.4°$ and 15% at $\theta = 90.0°$. The lift coefficient curve from the current experiment does not exhibit the expected $\sqrt{C_\mu}$ behaviour. Rather the reaction component of Equation 2.4 fits the data within uncertainty. Thus it appears that the significant 'pressure lift' component of the equation is missing.

Figure 9.5 gives a close up comparison between Dimmock's results with and without trip wires, which were used to simulate an increase in Reynolds number. In both cases the measured C_l values converge onto the predicted curve with increasing C_μ. Notice that the case with the trip wire is closer to the predicted curve. While the high Reynolds number results in Figure 9.4 do exhibit a slight curvature, it is not possible to say if the lift would converge onto the expected curve at a sufficiently high C_μ.

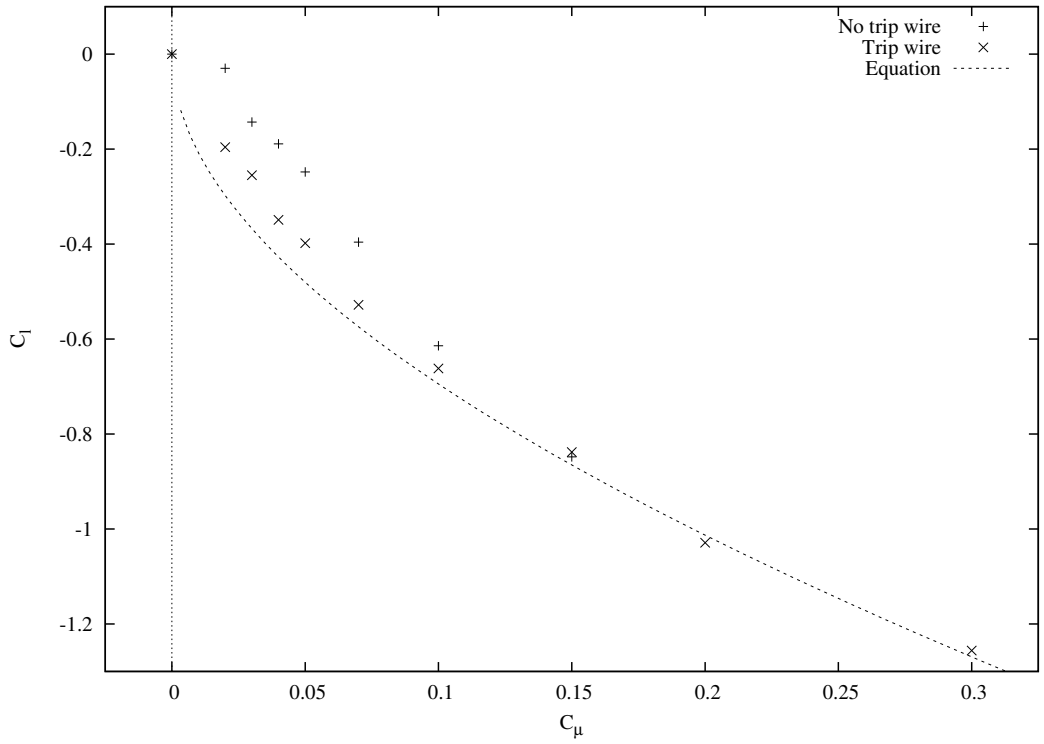

Figure 9.5: Effect of tripping the boundary layer: $\alpha = 0°, \theta = -31.4°, \mathrm{Re} = 0.425 \times 10^6$. All data from Dimmock [6].

9.4 Pressure Lift

From examining the low and high Reynolds results, and comparing them to previous results it is clear that the current experimental results do not show the characteristic 'pressure lift' effect. It is therefore worth investigating why this important component is not exhibited. As before, a qualitative examination of the wake profiles in Figures 9.6(a), 9.6(b), 9.7(a), and 9.7(b) reveals what occurs in the flow.

In Figures 9.6(a) and (b) it is seen that the wake initially narrows with increasing C_μ. This is the well known aerofoil boundary layer control effect of momentum injection. With increasing C_μ the trend reverses and the wake widens greatly. A large wake represents a large loss in momentum, which is not an expected result of momentum injection. Notice that in the 0° case, where the magnitude of lift is greater than that of the 5° case, the wake is also larger. The 10° and 15° wake profiles follow the same trends as the lower angles of attack. With a larger angle of attack the initial wake is deeper and the smallest wake occurs at higher C_μ. Again the final wake is smaller with increasing angle of attack and decreasing magnitude of lift. The loss in flow momentum with larger C_μ is a result of the jet forcing the flow to separate at the trailing edge behind the jet. This is analogous to the increase in drag and loss of lift due to locating a Gurney flap ahead of the trailing edge (Section 2.3.3). This observation is also supported by a qualitative examination

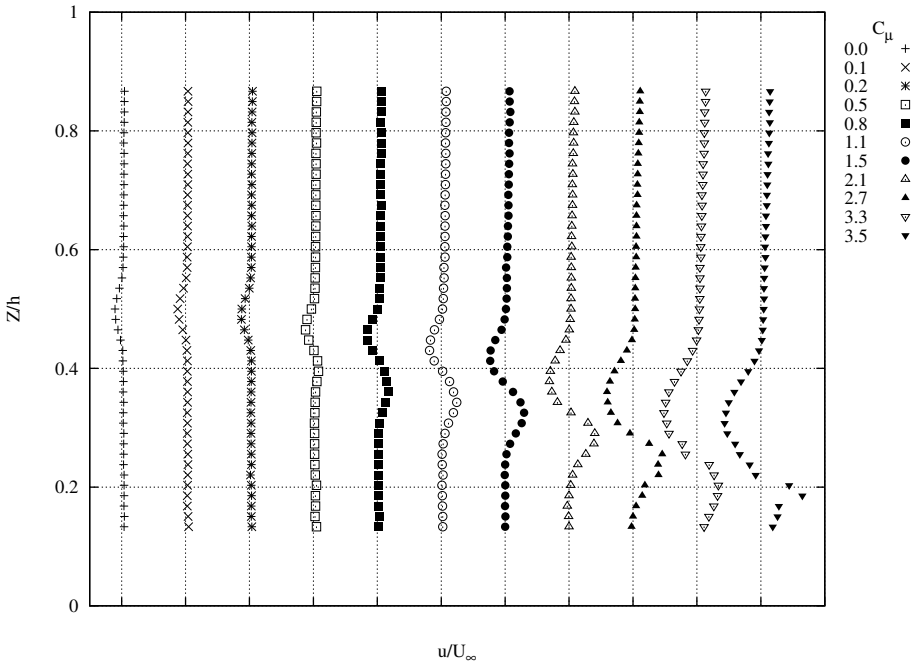

(a) $\alpha = 0°$

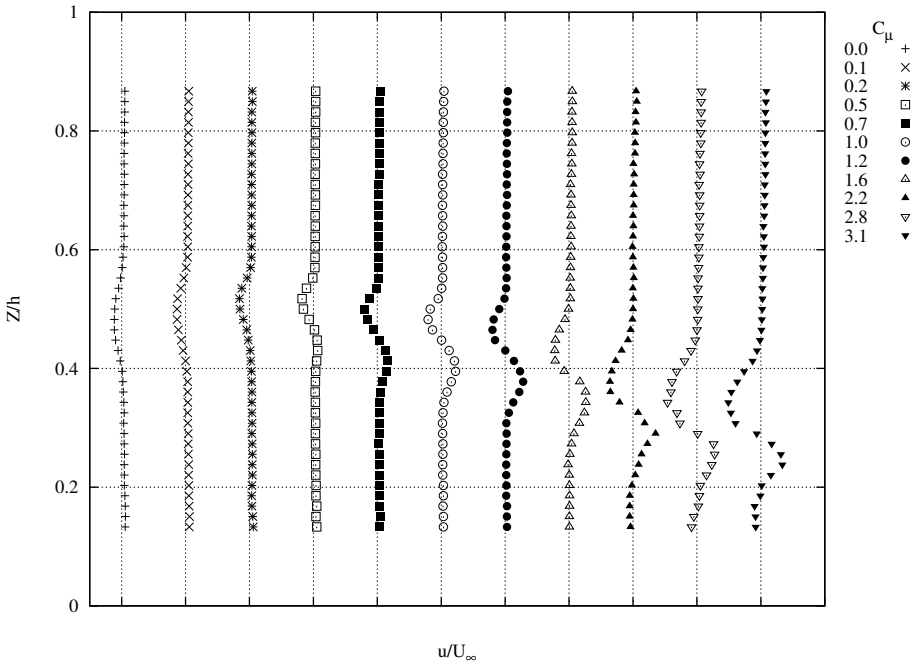

(b) $\alpha = 5°$

Figure 9.6: Low speed flow wake profiles for 0° and 5° listed by C_μ. Note again curves are offset for clarity; grid-lines indicate $\frac{u}{U_\infty} = 1$.

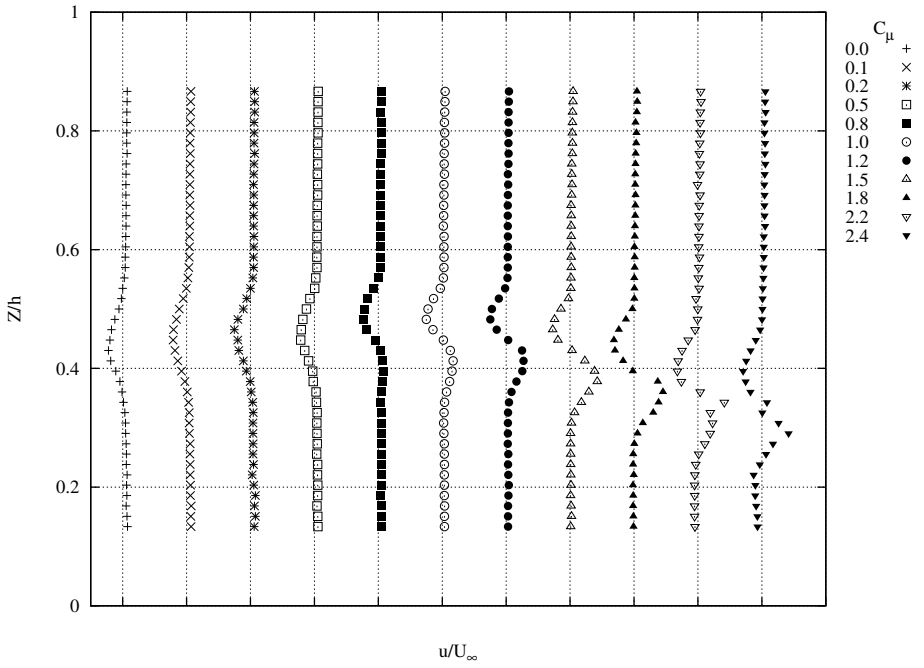

(a) $\alpha = 10°$

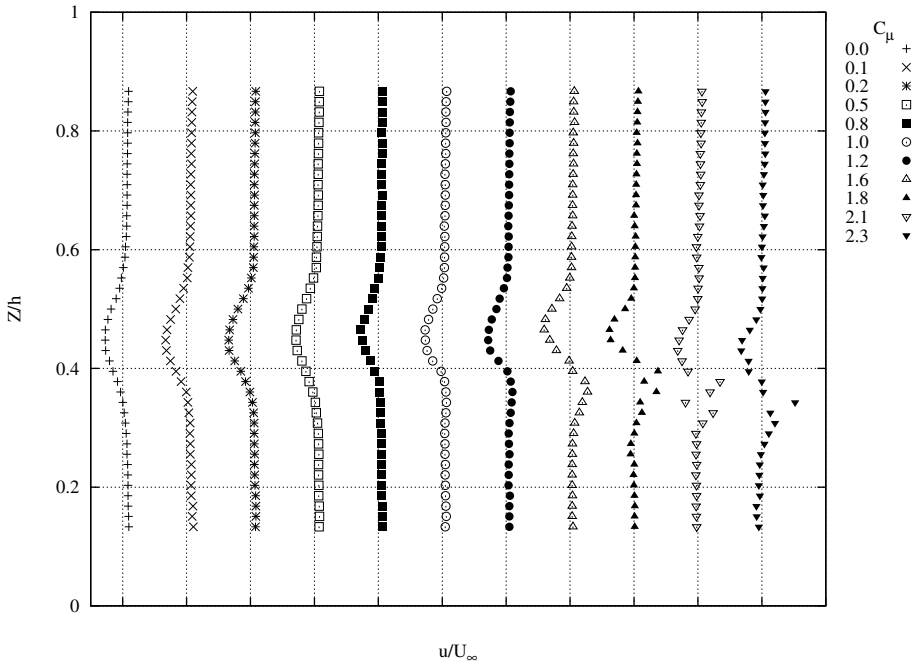

(b) $\alpha = 15°$

Figure 9.7: Low speed flow wake profiles for 10° and 15° listed by C_μ. Note again curves are offset for clarity; grid-lines indicate $\frac{u}{U_\infty} = 1$.

of flow visualization images. Figure 9.8 is an example of one such image. Unlike the aforementioned low speed wake profiles, the high speed wake profiles reveal nothing particularly interesting about the flow over the limited range of C_μ. Refer to Section B.2 in the appendix for the high Re wake profiles.

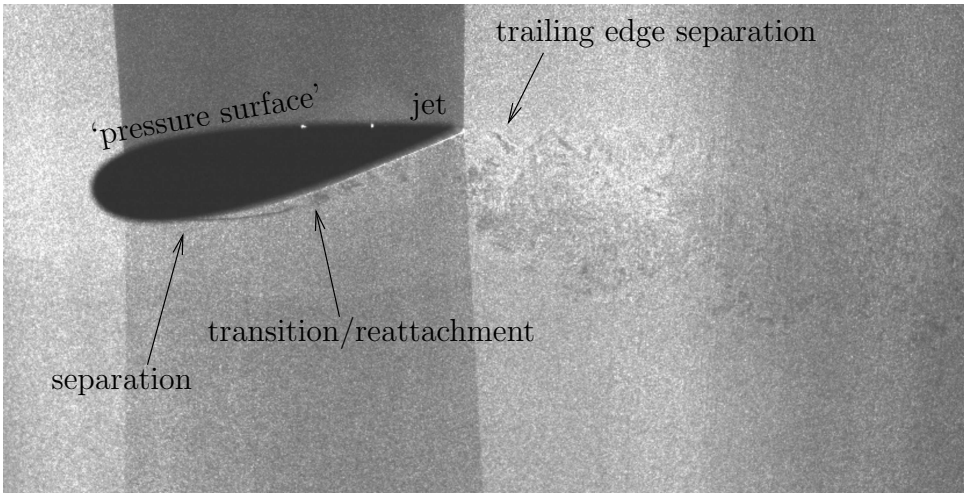

Figure 9.8: Flow visualization image of aerofoil at 10°, $C_\mu = 0.5$, and Re $= 0.038 \times 10^6$. Note the separation and reattachment over the aerofoil as well as the trailing edge separation.

9.5 Pressure Lift Replacement

Interesting parallels can be drawn between Dimmock's results (Figure 9.5) if the 'missing' pressure lift is replaced. In effect this is adding the lift as follows:

$$C_l = C_{l,measured} + \left(3.9\sqrt{C_\mu}\right) sin(\theta + \alpha) \tag{9.1}$$

Though this seems artificial, it allows flow separation effects to be observed apart from the trailing edge separation. The result of adding in this term is shown in Figure 9.9(a) through 9.10(b).

Figures 9.9(a) and (b) show how, with this method, the data collapse down onto the predicted curve. The more interesting result is the deviation from the predicted curve of the lift coefficient in Figures 9.10(a) and (b). Notice that in the 10° high speed case the measured lift slightly exceeds the expected lift in magnitude. At the same angle of attack and lower speed the lift deviates more from what is expected. Similarly at $\alpha = 15°$ (Figure 9.10(b)) both high and low Reynolds number curves exceed in magnitude the expected lift. Notice that the low Re data at both 10° and 15° converge onto the expected curve with increasing C_μ. Note that in the published data (Figure 9.5) the data follows the same trend, however on the opposite side of the predicted curve.

The explanation for this behaviour is flow separation on the 'suction surface' as shown in Figures 6.1 and 9.8. This is the *same* surface that the jet is located on. Due to flow separation the 'natural' component ($2\pi\alpha\eta$) of lift is diminished, so the jet is more effective in a relative sense, and the magnitude of lift is therefore greater. As C_μ is increased it has a boundary layer control effect causing the flow to reattach and the 'natural' lift to increase working against the 'pressure' and 'reaction' components. Note that at 10° and low Re the data fall on the predicted curve at fifth and higher jet momentum rates, and at 15° on the seventh. Referring back to Figures 9.7(a) and (b) it is seen that the wake narrows at approximately the fifth wake and seventh wake profiles respectively. Qualitatively these are also the flow rates at which the jet velocity becomes visible in the profiles.

In essence the aforementioned effect is the result of placing the jet on the 'suction surface' of the aerofoil. More accurately this is the effect of setting ($\theta \leq 0$, $\alpha \geq 0$) or ($\theta \geq 0$, $\alpha \leq 0$). From a control perspective it is problematic to have a control action respond in an opposite manner under a limited set of conditions. Thus from the control perspective at lower Reynolds numbers it is advantageous to locate the control jet on the 'pressure surface' of the aerofoil.

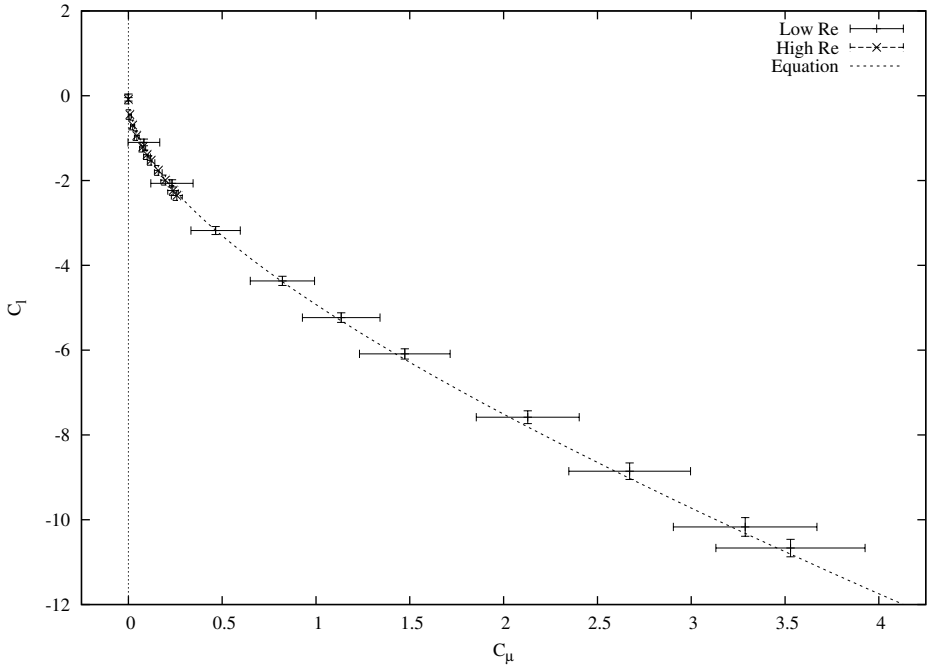

(a) 0°

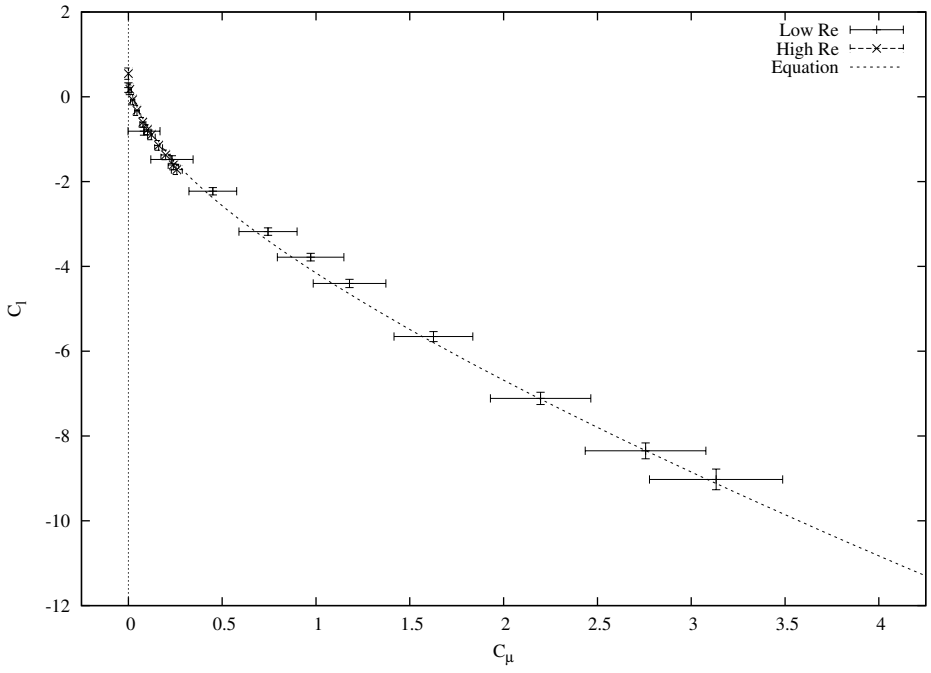

(b) 5°

Figure 9.9: Low and high Reynolds number data at 0° and 5° with 'replaced' pressure lift.

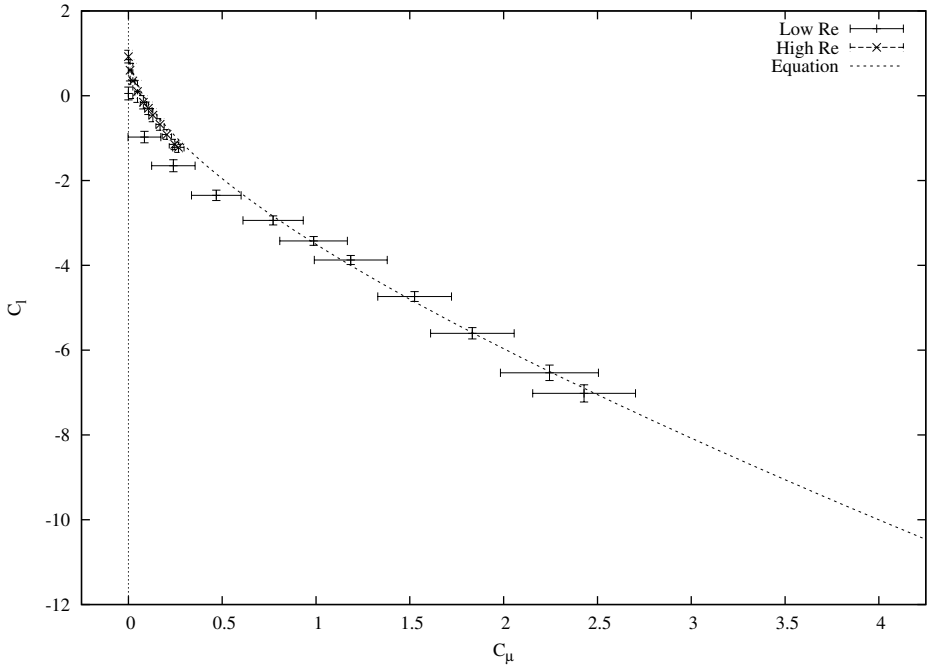

(a) 10°

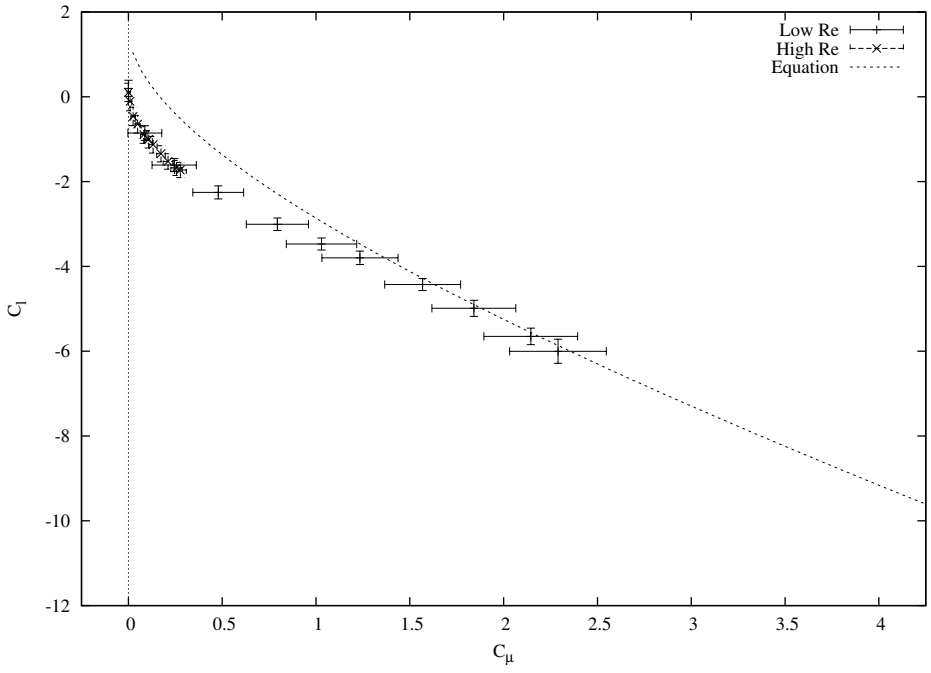

(b) 15°

Figure 9.10: Low and high Reynolds number data at 10° and 15° with 'replaced' pressure lift.

Chapter 10

Conclusions and Recommendations

10.1 Conclusions

A jet control sheet and its accompanying air supply system can be fabricated in a conventional aerofoil with simple practical manufacturing methods. In particular a row of discrete drilled outlets can be used as an alternative to a continuous slot.

Although discrete air jets are not uniform in either the near or far field, the individual jets do spread and merge to form a jet sheet. Differences between the shape and angle of the drilled holes leads to variation in the jet profile from what is expected.

The simple jet orifices were subject to large losses when the supply pressure was raised above the critical pressure ratio, hence the pressure should not be raised above this level unless the nozzle shape is refined.

In general there is a limitation on the upper range of practical free-stream velocities for jet control, since $C_\mu \propto U_\infty^{-2}$. It was found that there are also significant limitations to the effectiveness of jet control in very low Reynolds number regimes ($Re \approx 10^5$), hence this method is most appropriate for moderate Reynolds number wind turbines. In low Reynolds number flows the jet has a significant boundary layer control effect through jet entrainment. Under conditions of natural flow separation, such as high angle of attack, momentum from the jet is absorbed by the thick boundary layer and the wake. It was found that near stall low levels of C_μ caused flow separation from the aerofoil surface, while at high levels it caused reattachment.

Practical aerofoils typically have sharp trailing edges. If a sharp trailing edge is used then the control jet must be located forward of this position. Locating the control jet at 9% forward of the trailing edge has a detrimental effect on both the lift and drag of the aerofoil. With the given configuration the jet acts to separate the flow at the trailing edge, which increases drag and prevents 'pressure lift' from

being generated over the aerofoil. Thus the only modification of lifting force is through the jet reaction thrust itself.

In low Reynolds number flow the effect of negative jet deflection angle, combined with positive angle of attack, is that the boundary layer control acts counter to the intended 'flap action'. The opposing control effect, along with the aforementioned forced flow separation, lead to the conclusion that this is not a good control method for low Reynolds number flow regimes.

10.2 Recommendations

It is recommended that proportionally smaller, but more frequent, jet outlets should be used. This would be particularly easy if larger aerofoil models were constructed. More frequent outlets should lead to a more uniform flow in the near field, which is more similar to a sheet.

If possible further testing should be conducted at higher Reynolds number to determine if the large separated wake occurs under this condition and if there is evidence of 'pressure lift'. If higher Reynolds number testing cannot be done then the use of trip wires should be attempted to simulate higher Reynolds number flow.

Experimentation with a smaller jet deflection angle is recommended to determine if trailing edge separation can be avoided at low Reynolds number. Tests with a slightly truncated and rounded trailing edge could be done to determine if separation can be minimized in this way. It is possible that this, or a similar system, could be useful on inboard truncated wind turbine aerofoils [33].

It is worth investigating if the use of periodic jet flow can prevent flow separation, either over the aerofoil or at the trailing edge, and improve performance. Both the frequency and the duty cycle of the jet flow could be varied to study the response.

Finally it is recommended that, once effective control of steady flow has been established, the step-change and sinusoidally-varying angle of attack cases be investigated.

References

[1] T. Burton, D Sharpe, N. Jenkins, and E. Bossanyi. *Wind Energy Handbook*, chapter 8.3.9, pages 492–493. John Wiley and Sons, Toronto, 2001.

[2] T. J. Larsen, H. A. Madsen, and K. Thomsen. Active load reduction using individual pitch, based on local blade flow measurements. *Wind Energy*, 8(1):67–80, 2005.

[3] L. W. Carr. Progress in analysis and prediction of dynamic stall. *Journal of Aircraft*, 25(1):6–17, January 1988.

[4] S. Schreck and M. Robinson. Blade three-dimensional dynamic stall response to wind turbine operating condition. *Journal of Solar Energy Engineering*, 127:488–495, 2005.

[5] M. M. Hand, D. A. Simms, L. J. Fingersh, D. W. Jager, J. R. Cotrell, S. Schreck, and S. M. Larwood. Unsteady aerodynamics experiment phase vi: Wind tunnel test configurations and available data campaigns. Technical Report TP-500-29955, National Renewable Energy Laboratory, December 2001.

[6] N. A. Dimmock. An experimental introduction to the jet flap. Current Paper 344, Aeronautical Research Council, London, 1957.

[7] G. K. Korbacher and K. Sridhar. A review of the jet flap. UTIA Review 14, University of Toronto, May 1960.

[8] B. Massey and J. Ward-Smith. *Mechanics of Fluids*, pages 108–109. Taylor and Francis, New York, eighth edition, 2006.

[9] T. Strand. The jet flap: review and extension. Convair division report, General Dynamics Corporation, 1956.

[10] D. A. Spence. The lift coefficient of a thin, jet-flapped wing. *Proceedings of the Royal Society A*, 238(1212):46–68, December 1956.

[11] B. S. Stratford. Mixing and the jet flap. *The Aeronautical Quarterly*, 7(2):85–105, May 1956.

[12] B. S. Stratford. A further discussion on mixing and the jet flap. *The Aeronautical Quarterly*, 7(3):169–183, August 1956.

[13] C. Tongchitpakdee, S. Benjanirat, and N. S. Sankar. Numerical studies of the effects of active and passive circulation enhancement concepts on wind turbine performance. *Journal of Solar Energy Engineering*, 128:432–444, 2006.

[14] L. W. Traub, A. C. Miller, and O. Rediniotis. Comparisons of a gurney and jet flap for hingeless control. *Journal of Aircraft*, 41(2):420–423, 2004.

[15] D. A. Spence. Some simple results for two-dimensional jet-flap aerofoils. *The Aeronautical Quarterly*, 9:395–406, 1958.

[16] D. T. Y. Nakafuji, C. P. van Dam, R. L. Smith, and S. D. Collins. Active load control for airfoils using microtabs. *Journal of Solar Energy Engineering*, 123:282–289, 2001.

[17] T. Buhl, M. Gaunaa, and C. Bak. Potential load reduction using airfoils with variable trailing edge geometry. *Journal of Solar Energy Engineering*, 127:503–516, 2005.

[18] B. Sperandei. The application of particle image velocimetry in a small scale wind tunnel. Master's thesis, University of Waterloo, November 2002.

[19] R. C. Pankhurst and D. W. Holder. *Wind-Tunnel Technique*. Sir Isaac Pitman and Sons, Ltd., Toronto, 1952.

[20] Rae W. H. Jr. and Pope A. *Low-Speed Wind Tunnel Testing*. John Wiley and Sons, New York, 1984.

[21] E. N. Jacobs, K. E. Ward, and R. M. Pinkerton. The characteristics of 78 related aerofoil sections from tests in the variable-density wind tunnel. Technical Report 460, National Advisory Committee for Aeronautics, January 1933.

[22] Photograph by Stephen Orlando, January 2010.

[23] R. W. Miller. *Flow Measurement Engineering Handbook*, chapter 14, pages 40–48. McGraw-Hill, third edition, 1996.

[24] M. Raffel, C. Willert, and J. Kompenhans. *Particle Image Velocimetry*. Springer-Verlag, New York, 1998.

[25] H. E. Albrecht, M. Borys, N. Damaschke, and C. Tropea. *Laser Doppler and Phase Doppler Measurement Techniques*. Springer-Verlag, New York, 2003.

[26] M. Young. *Optics and Lasers*. Springer-Verlag, New York, second edition, 1984.

[27] M. G. Salvadori and M. L. Baron. *Numerical Methods in Engineering*. Prentice-Hall, New York, 1952.

[28] F. M. White. *Fluid Mechanics*. McGraw-Hill, New York, 2003.

[29] H. Schlichting. *Boundary-Layer Theory*. McGraw-Hill, Toronto, seventh edition, 1987.

[30] S.B. Pope. *Turbulent Flows*. Cambridge University Press, New York, 2006.

[31] P. R. Bevington. *Data Reduction and Error Analysis for the Physical Sciences*. McGraw-Hill, New York, 1969.

[32] R. E. Sheldahl and P. C. Klimas. Aerodynamic characteristics of seven symmetrical airfoil sections through 180-degree angle of attack for use in aerodynamic analysis of vertical axis wind turbines. Energy Report SAND80-2114, Sandia National Laboratories, Albuquerque, March 1981.

[33] S. P. Law and Gregorek G. M. Wind tunnel evaluation of a truncated naca 64-621 airfoil for wind turbine applications. Technical Report CR-180803, National Aeronautics and Space Administration, July 1987.

APPENDICES

Appendix A

Ancillary Information on Jet Experiment

A.1 Beam Properties

Table A.1: LDA beam properties.

Parameter	Symbol	Value
Beam expander ratio	-	1.98
Initial beam diameter	-	2.16×10^{-3} m
Beam diameter before focusing	$2 \cdot w_f$	4.28×10^{-3} m
Beam separation before expansion	-	38.1×10^{-3} m
Beam separation distance	d_s	75.4×10^{-3} m
Lens focal length	f	310×10^{-3} m
Distance of focal point along beam	$l(d_s, f)$	312×10^{-3} m
LDA beam intersection half-angle	$\frac{\phi}{2}$	0.121 rad

A.2 Jet Momentum Integration Uncertainty

$$\sigma_{\dot{M}_x} \approx \sqrt{\sum_{x,y} \left[\frac{W\rho\Delta x\Delta y V_x V_z}{9}\right]^2 \left[\left(\frac{\epsilon_\rho}{\rho}\right)^2 + \left(\frac{\epsilon_{\Delta x}}{\Delta x}\right)^2 + \left(\frac{\epsilon_{\Delta y}}{\Delta y}\right)^2 + \left(\frac{\sigma_{V_x}}{V_x}\right)^2 + \left(\frac{\sigma_{V_z}}{V_z}\right)^2\right]} \tag{A.1}$$

$$\sigma_{\dot{M}_z} \approx \sqrt{\sum_{x,y} \left[\frac{W\rho\Delta x\Delta y V_z^2}{9}\right]^2 \left[\left(\frac{\epsilon_\rho}{\rho}\right)^2 + \left(\frac{\epsilon_{\Delta x}}{\Delta x}\right)^2 + \left(\frac{\epsilon_{\Delta y}}{\Delta y}\right)^2 + \left(\frac{2\sigma_{V_z}}{V_z}\right)^2\right]} \tag{A.2}$$

$$\sigma_{\dot{M}} = \frac{1}{\dot{M}}\sqrt{\left(\sigma_{\dot{M}_x}\dot{M}_x\right)^2 + \left(\sigma_{\dot{M}_z}\dot{M}_z\right)^2} \tag{A.3}$$

A.3 LDA Data Rate

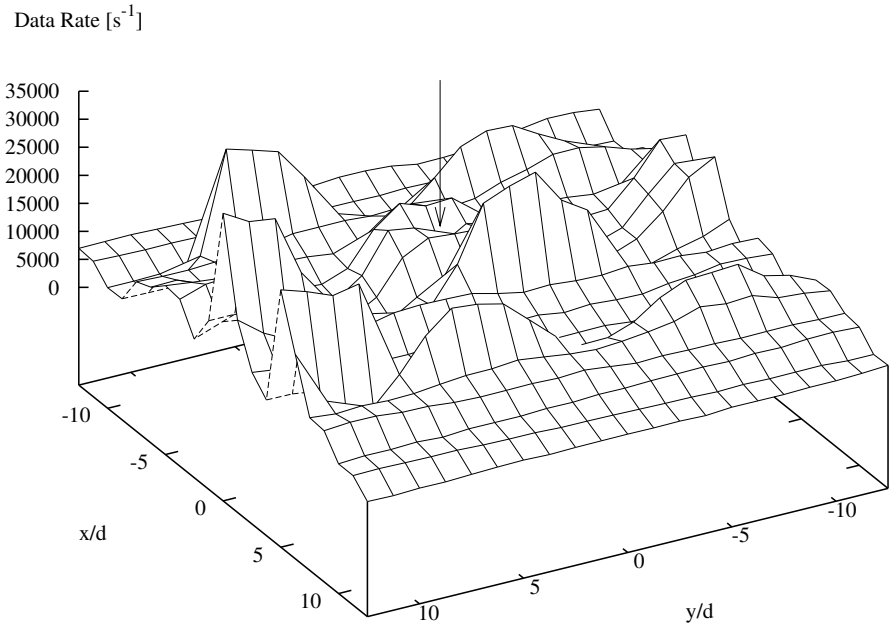

(a) 24d from jet orifice

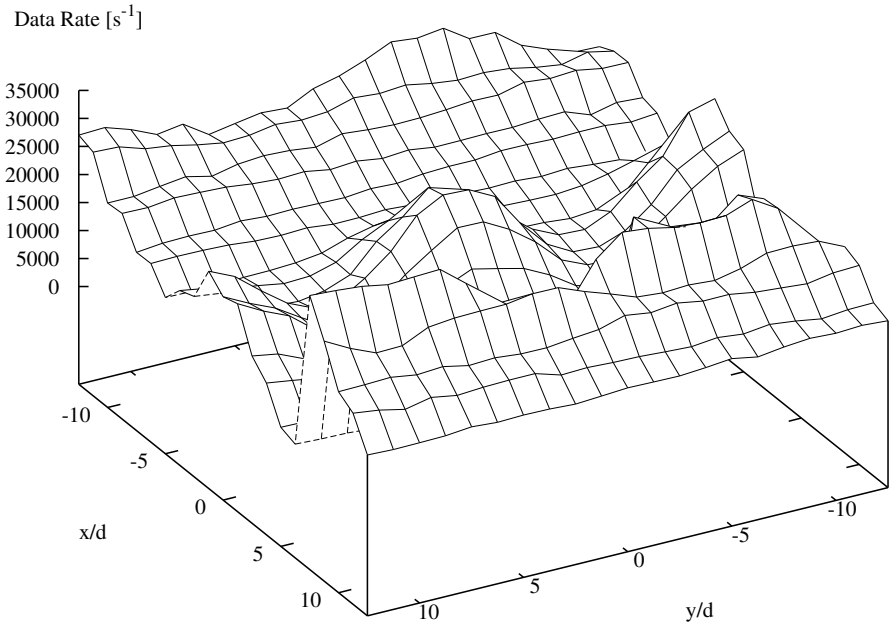

(b) 38d from jet orifice

Figure A.1: LDA data rate. Note arrow in Figure A.1(a) showing distinct dimple at the centre of the grid not seen in Figure A.1(b).

A.4 Measured Jet Properties

Table A.2: Jet half widths at 10×10^{-3} m cross section (all in mm).

Direction	Jet 13		Jet 14		Jet 15		Average
	$w+$	$w-$	$w+$	$w-$	$w+$	$w-$	w
x	1.1	1.0	1.3	1.0	1.4	1.2	1.2
y	1.2	-	1.4	1.3	-	1.5	1.3

Table A.3: Jet half widths at 15×10^{-3} m cross section (all in mm).

Direction	Jet 13		Jet 14		Jet 15		Average
	$w+$	$w-$	$w+$	$w-$	$w+$	$w-$	w
x	1.8	1.3	2.1	1.3	1.8	1.8	1.7
y	2.0	-	1.7	2.2	-	2.2	2.0

Table A.4: Stagnation pressure and pressure ratios with flow rate. Note p^* is the pressure at the orifice and p_{atm} is atmospheric pressure.

$q_V \times 10^6$ [m^3 s^{-1}]	$p_f \times 10^{-3}$ [Pa] (absolute)	$\frac{p^*}{p_f}$	$\frac{p^*}{p_{atm}}$
386	106	0.957	1.000
552	116	0.870	1.000
690	132	0.766	1.000
802	153	0.662	1.000
840	170	0.595	1.000
878	184	0.550	1.000
940	219	0.528	1.139
998	253	0.528	1.319
1041	294	0.528	1.535
1077	308	0.528	1.607

A.5 Equation of Two Dimensional Jet Profile

Schlichting [29] suggests the following equation to describe a jet velocity (u) in terms of the centre-line velocity (u_m) and the free stream velocity (U_∞):

$$\frac{u^2 - U_\infty^2}{u_m^2 - U_\infty^2} = e^{-ln(2)\cdot\left(\frac{y}{b}\right)^2}$$

where the width b is defined as the jet width, in terms of momentum, so that if $y = b$ then

$$\frac{u^2 - U_\infty^2}{u_m^2 - U_\infty^2} = \frac{1}{2}$$

In the LDA experiment the free stream velocity is zero, so the above equation is simplified somewhat. Alternatively the jet half radius ($r_{1/2}$) can be defined in terms of the location where the velocity is half that of the centre-line following Pope [30]. This requires the constant in the exponential to be changed to $ln(0.5)$ so that at radial location $r = r_{1/2}$ the jet velocity is $\frac{1}{2}V_{j,max}$. Thus the velocity in polar coordinates is:

$$V_j = V_{j,max} \cdot e^{ln(0.5)\cdot\left(\frac{r}{r_{1/2}}\right)^2}$$

For non rotationally symmetric distributions the $\left(\frac{r}{r_{1/2}}\right)^2$ term can be replaced with its multidimensional equivalent $\left(\frac{x}{w_x}\right)^2 + \left(\frac{y}{w_y}\right)^2$. Thus the full equation becomes:

$$V_j = V_{j,max} \cdot e^{ln(0.5)\cdot\left[\left(\frac{x}{w_x}\right)^2+\left(\frac{y}{w_y}\right)^2\right]}$$

If the major and minor axes are equal ($w_x = w_y$) then the equation becomes equivalent to the rotationally symmetric equation above.

A.6 Momentum Integral

The equation of the jet velocity is:

$$V_j = V_{j,max} \cdot e^{ln(0.5)\cdot\left[\left(\frac{x}{w_x}\right)^2+\left(\frac{y+\delta}{w_y}\right)^2\right]}$$

For a row of n jets the sum of squared velocities is:

$$V_J^2 = V_{j,max}^2 \cdot e^{2\cdot ln(0.5)\cdot\left[\left(\frac{x}{w_x}\right)^2+\left(\frac{y+\delta_1}{w_y}\right)^2\right]} + \ldots + V_{j,max}^2 \cdot e^{2\cdot ln(0.5)\cdot\left[\left(\frac{x}{w_x}\right)^2+\left(\frac{y+\delta_n}{w_y}\right)^2\right]}$$

Substituting into the momentum flux equation and integrating:

$$\begin{aligned}
\dot{M}_n &= \int_{-\infty}^{\infty}\int_{-\infty}^{\infty} \rho\left(V_J^2\right) dxdy \\
&= \int_{-\infty}^{\infty}\int_{-\infty}^{\infty} \rho\left(V_{j,max}^2 \cdot e^{2\cdot ln(0.5)\cdot\left[\left(\frac{x}{w_x}\right)^2+\left(\frac{y+\delta_1}{w_y}\right)^2\right]} + \ldots\right) dxdy \\
&= \rho V_{j,max}^2\left[\int_{-\infty}^{\infty}\int_{-\infty}^{\infty} e^{2\cdot ln(0.5)\left(\frac{y+\delta_1}{w_y}\right)^2} e^{2\cdot ln(0.5)\left(\frac{x}{w_x}\right)^2} dxdy + \ldots\right] \\
&= \rho V_{j,max}^2\left[\int_{-\infty}^{\infty}\left(e^{2\cdot ln(0.5)\left(\frac{y+\delta_1}{w_y}\right)^2}\int_{-\infty}^{\infty} e^{2\cdot ln(0.5)\left(\frac{x}{w_x}\right)^2} dx\right) dy + \ldots\right]
\end{aligned}$$

Since $\int_{-\infty}^{\infty} e^{-ax^2}dx = \sqrt{\frac{\pi}{a}}$ then set $a = -\frac{2\cdot ln(0.5)}{w_x^2}$

$$\begin{aligned}
\dot{M}_n &= \rho V_{j,max}^2\left[w_x\sqrt{\frac{-\pi}{2\cdot ln(0.5)}}\int_{-\infty}^{\infty} e^{2\cdot ln(0.5)\left(\frac{y+\delta_1}{w_y}\right)^2} dy + ...\right] \\
&= \rho V_{j,max}^2\left[w_x\sqrt{\frac{-\pi}{2\cdot ln(0.5)}}\left(e^{2\cdot ln(0.5)\left(\frac{\delta_1}{w_y}\right)^2}\int_{-\infty}^{\infty} e^{\frac{2\cdot ln(0.5)}{w_y^2}y^2} e^{2\frac{2\delta_1\cdot ln(0.5)}{w_y^2}y} dy\right) + ...\right]
\end{aligned}$$

Since $\int_{-\infty}^{\infty} e^{-ay^2}e^{-2by}dy = \sqrt{\frac{\pi}{a}}e^{\frac{b^2}{a}}$ then set $a = -\frac{2\cdot ln(0.5)}{w_y^2}$, $b = -\frac{2\delta_1\cdot ln(0.5)}{w_y^2}$

$$\begin{aligned}
\dot{M}_n &= \rho V_{j,max}^2\left[w_x\sqrt{\frac{-\pi}{2\cdot ln(0.5)}}e^{2\cdot ln(0.5)\left(\frac{\delta_1}{w_y}\right)^2} w_y\sqrt{\frac{-\pi}{2\cdot ln(0.5)}}e^{-2\cdot ln(0.5)\left(\frac{\delta_1}{w_y}\right)^2} + \ldots\right] \\
&= \rho V_{j,max}^2\left[\frac{\pi(w_x w_y)}{-2\cdot ln(0.5)} + \frac{\pi(w_x w_y)}{-2\cdot ln(0.5)} + \ldots + \frac{\pi(w_x w_y)}{-2\cdot ln(0.5)}\right] \\
&= \frac{\pi\rho(w_x w_y)V_{j,max}^2}{-2\cdot ln(0.5)} \times n
\end{aligned}$$

Appendix B

Ancillary Information on Lift Control Experiment

B.1 Measured Angle of Attack in PIV Experiment

Table B.1: Measured α at low Re for each ensemble and nominal α in degrees.

Nominal	Ensembles						Average
	1	2	3	4	5	6	
0	-0.87	-1.05	-0.58	-0.22	-1.05	-0.87	-0.77
5	6.26	6.21	5.07	5.07	4.19	4.30	5.18
10	9.18	9.32	10.19	10.27	10.32	10.39	9.95
15	14.66	14.96	14.75	14.36	14.39	14.50	14.60

Table B.2: Measured α at high Re for each ensemble and nominal α in degrees.

Nominal	Ensembles						Average
	1	2	3	4	5	6	
0	-0.93	-0.75	-0.40	-0.34	-1.17	-0.87	-0.74
5	6.87	6.35	5.34	5.26	4.52	4.22	5.43
10	9.32	9.65	10.88	10.67	10.70	10.73	10.33
15	14.38	14.90	14.41	14.85	14.75	14.96	14.71

B.2 Wake Profiles from PIV Experiment

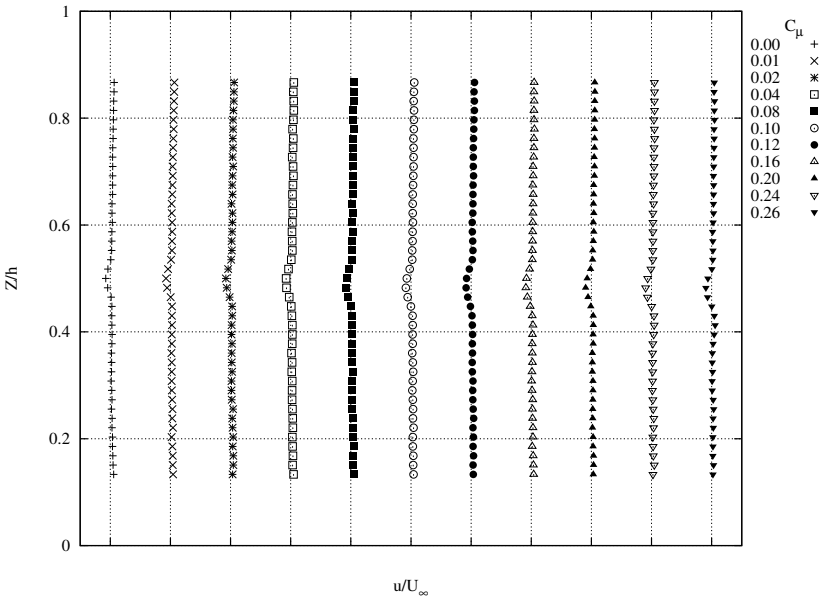

(a) $\alpha = 0°$

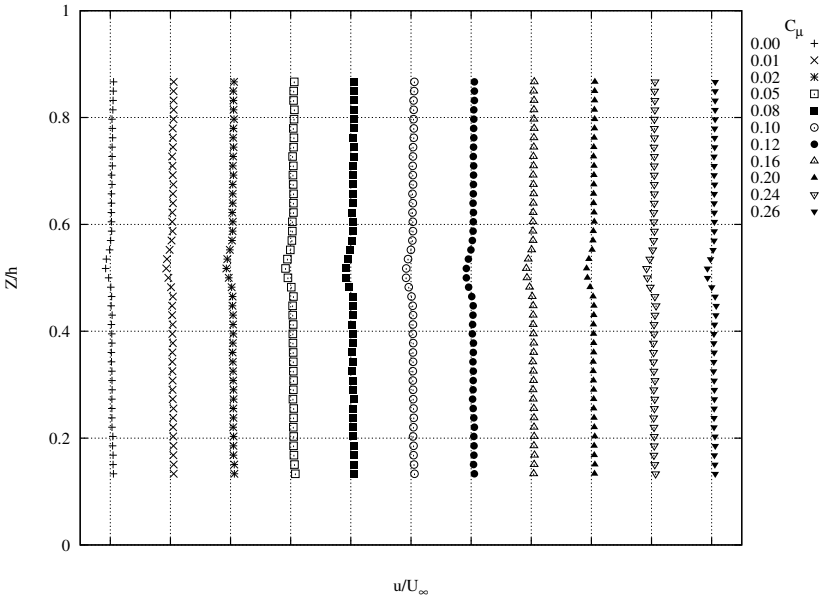

(b) $\alpha = 5°$

Figure B.1: High speed flow wake profiles for 0° and 5° listed by C_μ. Note again curves are offset for clarity; grid-lines indicate $\frac{u}{U_\infty} = 1$.

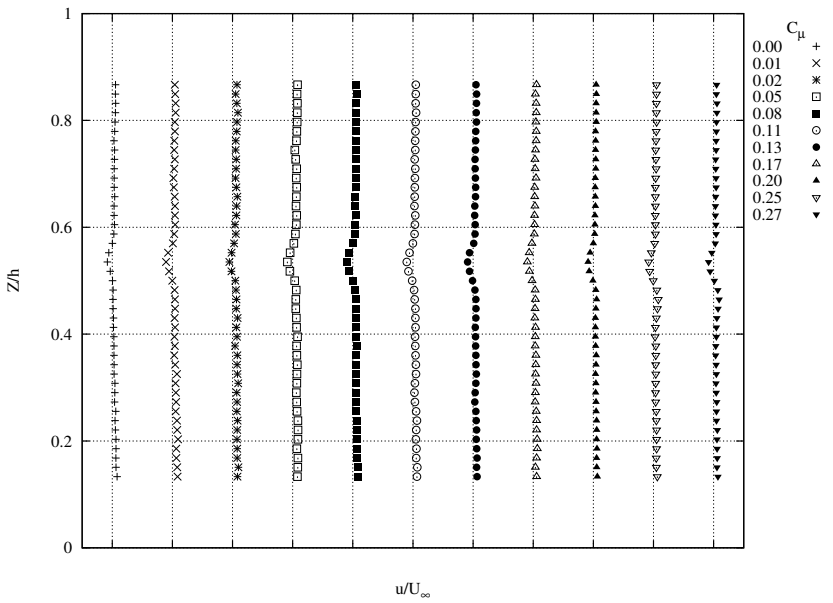

(a) $\alpha = 10°$

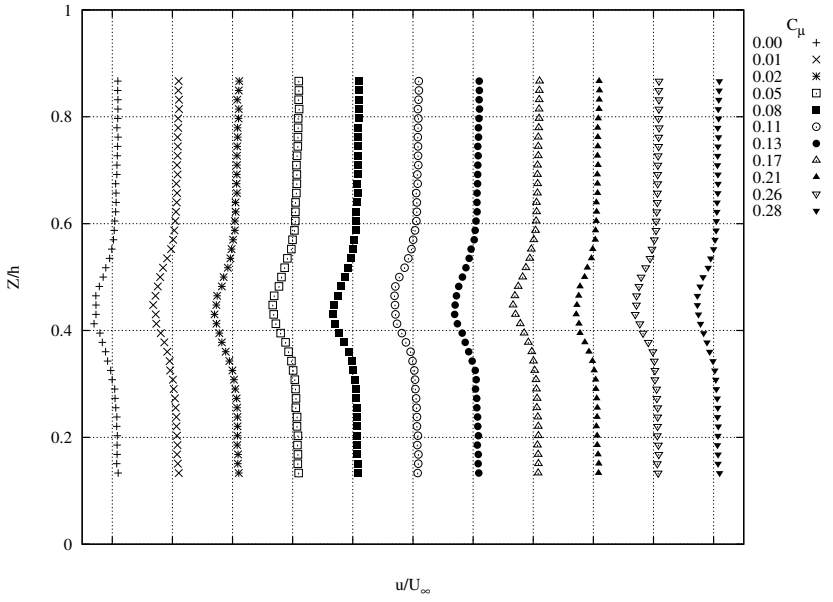

(b) $\alpha = 15°$

Figure B.2: High speed flow wake profiles for 10° and 15° listed by C_μ. Note again curves are offset for clarity; grid-lines indicate $\frac{u}{U_\infty} = 1$.